



NTNU – Trondheim
Norwegian University of
Science and Technology

Numerical investigation of thermal-hydraulics performance of fin-tube waste heat recovery units

Eirik Løland Eide

Master of Energy and Environmental Engineering

Submission date: June 2015

Supervisor: Erling Næss, EPT

Norwegian University of Science and Technology
Department of Energy and Process Engineering

EPT-M-2015-17

MASTER THESIS

for

Student Eirik Løland Eide

Spring 2015

Numerical investigation of thermal-hydraulics performance of fin-tube waste heat recovery units

Numerisk undersøkelse av termisk-hydraulisk ytelse for finnerørs varmegjenvinnere

Background and objective

The exhaust gas from a gas turbine contains large amounts of heat that can be utilized for process purposes or for power generation. On offshore oil and gas platforms, heat recovery units need to be compact and light weight. The Department, in cooperation with SINTEF Energy Research and international oil companies is engaged in research work which seeks to develop new, compact heat exchanger solutions for gas turbine exhaust gases. In this context, finned tubes have been selected as good candidates, due to the high specific heat transfer surface. A significant body of experimental data are available, obtained from a test rig for the measurement of heat transfer and pressure drop on finned tube bundles in the laboratory of NTNU.

The main objective of the project work is to further increase the understanding of fluid flow and heat transfer in finned tube bundles by numerical analysis, and to verify the calculations using the existing experimental data.

This work is a continuation of the Project work.

The following tasks are to be considered:

1. A numerical model for fluid flow in a finned tube bundle having cylindrical fins and serrated fins shall be further developed to also include heat transfer. The model shall be presented and all sub-models shall be justified.
2. Calculations shall be performed using the developed model with the purpose of reproducing existing experimental data. A detailed comparison of experimental data and model predictions shall be made and discussed. Systematic deviations shall be identified, and possible measures to correct these shall be attempted.
3. A detailed analysis of the fluid flow and heat transfer across a finned tube shall be made. The distribution shall be compared qualitatively to existing measurements in the published literature. Time allowing, the impact on the apparent fin efficiency shall be made.
4. Suggestions for further work shall be made.

Within 14 days of receiving the written text on the master thesis, the candidate shall submit a research plan for his project to the department.

When the thesis is evaluated, emphasis is put on processing of the results, and that they are presented in tabular and/or graphic form in a clear manner, and that they are analyzed carefully.

The thesis should be formulated as a research report with summary both in English and Norwegian, conclusion, literature references, table of contents etc. During the preparation of the text, the candidate should make an effort to produce a well-structured and easily readable report. In order to ease the evaluation of the thesis, it is important that the cross-references are correct. In the making of the report, strong emphasis should be placed on both a thorough discussion of the results and an orderly presentation.

The candidate is requested to initiate and keep close contact with his/her academic supervisor(s) throughout the working period. The candidate must follow the rules and regulations of NTNU as well as passive directions given by the Department of Energy and Process Engineering.


Risk assessment of the candidate's work shall be carried out according to the department's procedures. The risk assessment must be documented and included as part of the final report. Events related to the candidate's work adversely affecting the health, safety or security, must be documented and included as part of the final report. If the documentation on risk assessment represents a large number of pages, the full version is to be submitted electronically to the supervisor and an excerpt is included in the report.

Pursuant to "Regulations concerning the supplementary provisions to the technology study program/Master of Science" at NTNU §20, the Department reserves the permission to utilize all the results and data for teaching and research purposes as well as in future publications.


The final report is to be submitted digitally in DAIM. An executive summary of the thesis including title, student's name, supervisor's name, year, department name, and NTNU's logo and name, shall be submitted to the department as a separate pdf file. Based on an agreement with the supervisor, the final report and other material and documents may be given to the supervisor in digital format.

- Work to be done in lab (Water power lab, Fluids engineering lab, Thermal engineering lab)
 Field work

Department of Energy and Process Engineering, 14. January 2015



Olav Bolland
Department Head



Erling Næss
Academic Supervisor

Preface

This master thesis is carried out at the Department of Energy and Process Engineering of the Norwegian University of Science and Technology (NTNU). The master thesis constitutes 30 study points / ECTS credits and is performed during the second semester of the academic year 2014-2015.

I want to thank my supervisor professor Erling Næss for good advices and help throughout the work with the master thesis. I also want to thank PhD candidate Karl Lindqvist for giving valuable advices and feedback on the report.

Trondheim, Norway
June 2015

Eirik Løland Eide

Abstract

The objective of this master thesis is to increase the understanding of fluid flow and heat transfer development across a finned tube heat exchanger with help of Computational Fluid Dynamics (CFD). Three different geometries of finned tube bundles are considered. The finned tube bundles are made similar to existing experimental test rigs at NTNU carried out by Holfeld [11]. The purpose is to present a detailed comparison of the experimental data available and the result from a numerical model. Heat transfer and pressure drop performance is compared. The results are also compared with semi-empirical correlations from the published literature.

This master thesis is a continuation of the project work [7]. A main goal has been to expand the numerical model developed in the project work to include conjugate heat transfer. This has been successfully implemented by coupling the conduction and convection on the fins. Further a calculation method to predict the heat transfer on a row-to-row basis has been developed. The heat transfer coefficient and the fin efficiency are compared with the experimental data at each tube row for varying turbulent Reynolds numbers. The results shows that the heat transfer is predicted fairly good, but with some deviations. Generally the heat transfer is under-predicted for the two geometries having solid fins. The numerical model over-predicts the heat transfer for the geometry having serrated fins. The pressure drop performance is compared by looking at the pressure drop from the inlet to the outlet in the finned tube bundle. Larger deviations are seen between the numerical and experimental data for the pressure drop performance. Surprisingly, the pressure drop from the numerical model seems to be in better agreement with semi-empirical correlations from the published literature.

The effects of uneven heat transfer distribution has been investigated. An uneven heat transfer distribution is first of all reflected in the fin efficiency. Fin efficiencies found from the experiments and fin efficiencies calculated from the numerical model are therefore compared to theoretical fin efficiencies and reputable corrected fin efficiencies from the literature.

A qualitative analysis is performed by investigating relevant visualizations of the flow through the finned tube bundle. This analysis revealed several important effects happening in the finned tube bundles, affecting the heat transfer. This include boundary-layer development across the fins, horseshoe vortexes at the junction of the fin and tube and flow separation downstream of the finned tube rows. It is concluded that the use of CFD has a big potential for improving the prediction of heat transfer and pressure drop in fin-tube waste heat recovery units. Suggestions for further work on how the numerical model could be expanded are presented.

Sammendrag

Målet med denne masteroppgaven er å øke forståelsen av hvordan strømmingen utarter seg og varmevekslingen gjennom en ribberørs varmeveksler ved hjelp av numeriske simuleringer (CFD). Oppgaven tar for seg tre forskjellige geometrier for ribberørs varmevekslere. Varmevekslerene er laget lik varmevekslere fra eksisterende eksperimentelle rigger på NTNU gjennomført av Holfeld [11]. Hensikten er å presentere en detaljert sammenligning av varmeovergang og trykktapsytelse mellom tilgjengelig eksperimentelle data og resultat fra en numerisk modell av varmeveksleren. Resultatet er også sammenlignet med semi-empiriske korrelasjoner fra publisert litteratur.

Masteroppgaven er en fortsettelse av prosjektarbeidet [7]. Et hovedmål har vært å utvide den numeriske modellen fra prosjektoppgaven til å inkludere varmeveksling. Dette har vellykket blitt implementert ved å koble termisk konduksjon og konveksjon sammen på finnene. Videre har en beregningsmetode blitt utviklet for å predikere varmevekslingen fra rør-rekke til rør-rekke.

Varmeovergangstallet og finnevirkningsgraden er sammenlignet med eksperimentelle data for hver rørrekke med varierende turbulente Reynolds-tall. Resultatet viser at varmevekslingen er predikert ganske bra, men med noe avvik. For de to geometriene med solide finner er varmevekslingen under-predikert. Det motsatte er tilfelle for geometrien med seraterte finner. Trykktapsytelsen er sammenlignet ved å se på trykktapet mellom innløp og utløp på varmeveksleren. Større avvik mellom numeriske og eksperimentelle data oppleves for trykktapsytelsen. Overraskende nok ligger trykktapsytelsen tettere opp mot semi-empiriske korrelasjoner fra litteraturen.

Effektene fra ujevn varmevekslingsfordeling er undersøkt. En ujevn varmevekslingsfordeling kommer først og fremst til syne i finnevirkningsgraden. Finnevirkningsgradene fra eksperimentene og fra den numeriske modellen er derfor sammenlignet med teoretiske finnevirkningsgrader og anerkjente korrigerede finnevirkningsgrader fra litteraturen.

En kvalitativ analyse er gjennomført ved å undersøke relevante visualiseringer av strømmingen gjennom varmeveksleren. Analysen avdekket flere viktige fenomener som oppstår i varmeveksleren som påvirker varmevekslingen. Dette inkluderer grensesjiktutvikling på finnene, hestesko-virvlinger i krysningen mellom rørveggene og finnene samt separasjon av strømmingen bak rørrykkene. Det konkluderes med at bruk av CFD har et stort potensial i arbeidet med å forbedre predikeringen av varmeveksling og trykktapsytelse i ribberørs varmevekslere. Forslag til videre arbeid på hvordan den numeriske modellen kan utvides foreslås.

Contents

Preface	i
Abstract	iii
Sammendrag	v
Nomenclature	ix
List of Figures	xi
List of Tables	xiv
1 Introduction	1
1.1 Report structure	1
2 Theory on Finned Tube Heat Exchangers	3
2.1 Basic variables	4
2.2 Dimensionless numbers	5
2.3 Tube bundle arrangement	6
2.4 Fin efficiency	7
2.5 Correlations from the literature	9
3 Numerical Considerations	10
3.1 Turbulence models	10
3.1.1 Reynolds Averaged Navier-Stokes (RANS) Turbulence Model	12
3.2 Near-wall treatment	14
3.2.1 Near-wall regions for turbulent flows	14
3.2.2 Wall functions vs. near-wall model	15
3.3 Solver methods	16
3.3.1 Pressure-based solver	17
3.4 Ensuring convergence of the solution	18
4 Numerical Modeling of Staggered Fin-Tube Bundles	20
4.1 Geometry	20
4.2 Grid generation	22
4.2.1 Surface mesh	22
4.2.2 Volume mesh	22

4.2.3	Prism layers	23
4.3	Boundary Conditions	26
4.4	Physical properties	27
4.5	Standard procedure for running simulations	27
4.6	Data reduction	29
4.6.1	Calculation of relevant parameters	29
4.6.2	Evaluation of physical properties	29
4.6.3	Heat transfer	29
4.6.4	Pressure loss	32
4.7	Mesh sensitivity study for geometry 1	32
4.7.1	The tested meshes	32
5	Results and Discussion	34
5.1	Results from the mesh sensitivity study	34
5.2	Geometry 1 (solid fins)	38
5.2.1	Nusselt number	38
5.2.2	Euler number	38
5.2.3	Heat transfer	39
5.2.4	Fin efficiencies	41
5.3	Geometry 2 (solid fins)	44
5.3.1	Nusselt number	44
5.3.2	Euler number	44
5.3.3	Heat transfer	45
5.3.4	Fin efficiencies	46
5.4	Geometry 3 (serrated fins)	49
5.4.1	Nusselt number	49
5.4.2	Euler number	50
5.4.3	Heat transfer	50
5.4.4	Fin efficiencies	51
5.5	Fin efficiencies at varying thermal conductivities	54
5.6	Qualitative analysis of the finned tube bundles	56
5.6.1	Fluid flow behavior	56
5.6.2	Heat transfer behavior	66
6	Conclusions	76
7	Suggestions for Further Work	78
A	Thermo-Physical Properties	80
A.1	Air	80
A.2	Aluminum	80

A.3 Carbon Steel	81
B Correlations from literature	82
B.1 Heat transfer correlations	82
B.1.1 Solid fins	82
B.1.2 Serrated fins	83
B.2 Pressure drop correlations	83
B.2.1 Solid fins	83
B.2.2 Serrated fins	84

Nomenclature

Symbol	Units	Description
A	m^2	Heat transfer surface
C_p	$\text{J}/(\text{kg} \cdot \text{K})$	Specific heat capacity
d_o	m	Tube outer diameter
D_f	m	Fin diameter, $D_f = d_o + 2 \cdot h_f$
F_f	m^2	Free-flow area between fins for one tube
F_t	m^2	Free-flow area in transversal plane between two tubes
h_f	m	Fin height
h_s	m	Height of segmented section of fin
k	J/kg	Turbulent kinetic energy
\dot{m}	kg/s	Mass flow rate
m	$1/\text{m}$	Parameter defined in eq. 2.6
\dot{m}''	$\text{kg}/(\text{m}^2 \cdot \text{s})$	Mass flux in narrowest free-flow area, $\dot{m}'' = \dot{m}/F_{f,min}$
\vec{n}	–	unit vector normal to surface
N_L	–	Number of tube rows in longitudinal direction
p_f	m	Fin pitch
P_t	m	Pitch between tubes in transversal direction
P_l	m	Pitch between tubes in longitudinal direction
P_x	m	Pitch between tubes in diagonal direction
ΔP	Pa	Total Pressure drop in the finned tube bundle
\dot{Q}	W	Heat duty
\vec{q}	W/m^2	Heat flux vector
s_f	m	Fin spacing
T	K	Temperature
ΔT_{LMTD}	K	Logarithmic mean temperature difference for counterflow arrangement
t_f	m	Fin thickness
u	m/s	Velocity
U	$\text{W}/(\text{m}^2 \cdot \text{K})$	Overall heat transfer coefficient
w_f	m	Fin segment width
y^+	–	Dimensionless wall distance defined in eq. 3.10

Greek symbols

Symbol	Units	Description
α_e	$\text{W}/(\text{m}^2 \cdot \text{K})$	Effective/apparent average heat transfer coefficient at the outer surface of finned tube
α_o	$\text{W}/(\text{m}^2 \cdot \text{K})$	Actual heat transfer coefficient at the outer surface of finned tube

β	degree	Tube bundle arrangement angle
ρ	kg/m ³	Density
η	–	Fin efficiency
$\eta_{c,W}$	–	Corrected fin efficiency, proposed by Weierman [25]
$\eta_{c,H}$	–	Corrected fin efficiency, proposed by Hashizume et al. [9]
λ	W/(m · K)	Thermal conductivity
μ	kg/(m · s)	Dynamic viscosity
μ_t	kg/(m · s)	Turbulent viscosity

Dimensionless groups

Symbol	Description
Eu	Euler number, $Eu = \frac{2\Delta P \cdot \rho}{N_L \cdot (\dot{m}'')^2}$
Nu	Nusselts number, $Nu = \frac{\alpha_o d_o}{\lambda}$
Pr	Prandtl number, $Pr = \frac{\mu \cdot C_p}{\lambda}$
Re	Reynolds number, $Re = \frac{\dot{m}'' d_o}{\mu}$
Tu	Turbulent intensity, $Tu = \frac{\sqrt{u'^2}}{\bar{u}}$

Suffixes

a	Actual
air	Air
bare	Tube wall (excluding fin)
CFD	Computational Fluid Dynamics
exp	Experimental
f	Fin
in	Inlet
max	Maximum
min	Minimum
o	Outer
out	Outlet
row	Tube row
ser	Serrated
sim	Simulated
sol	Solid
th	Theoretical
tot	Total
w	Wall
∞	Local bulk fluid

List of Figures

2.1	Tubes with serrated fins (left) and solid fins (right). Courtesy: Delfintubes	3
2.2	Attachment methods for fins (taken from ESCOA [8])	4
2.3	Finned tube layout (taken from Næss [20])	4
2.4	Arrangements of tubes in bundles. Taken from Mon [16]	6
3.1	Subdivision of the near-wall region. Taken from [3]	15
3.2	Near wall treatments (applied in ANSYS FLUENT). Taken from [3]	16
3.3	Overview of the pressure-based solution methods. Taken from [3]	17
4.1	Computational domain	21
4.2	a. Individual annular fins; b. Helically wound fins (according to PFR [22])	22
4.3	Outer boundaries of mesh (for geometry 1)	23
4.4	Surface mesh on tube wall and fin (geometry 1)	24
4.5	Cut plane of the air-side volume mesh (geometry 1)	24
4.6	Prism layers near the finned tube surface (geometry 1)	25
4.7	Near-wall meshing of serrated geometry (geometry 3)	25
4.8	Planes at inlet/outlet of each tube row to calculate temperatures.	30
5.1	Nusselt number versus number of nodes for three different Reynolds numbers.	35
5.2	Euler number versus number of nodes for three different Reynolds numbers.	35
5.3	y^+ values for the decided mesh (for geometry 1) at $Re = 4397$ (top) and $Re = 26086$ (bottom)	37
5.4	$Nu \cdot Pr^{-\frac{1}{3}}$ vs. Re for geometry 1	38
5.5	Eu vs. Re for geometry 1	39
5.6	Comparison of the heat transfer coefficients for geometry 1 with four varying Reynolds number	40
5.7	Relative Deviation between simulated and experimental heat transfer coefficient for geometry 1, $\frac{\alpha_{o,exp} - \alpha_{o,sim}}{\alpha_{o,exp}} \cdot 100\%$	41
5.8	Ratio between row heat transfer coefficient to the average heat transfer coefficient for row 4-8 (geometry 1)	41
5.9	Fin efficiencies for geometry 1	43
5.10	$Nu \cdot Pr^{-\frac{1}{3}}$ vs. Re for geometry 2	44
5.11	Eu vs. Re for geometry 2	45

5.12 Comparison of the heat transfer coefficients for geometry 2 with four varying Reynolds number	46
5.13 Deviation between simulated and experimental heat transfer coefficient for geometry 2, $\frac{\alpha_{o,exp}-\alpha_{o,sim}}{\alpha_{o,exp}} \cdot 100\%$	47
5.14 Ratio between row heat transfer coefficient to the average heat transfer coefficient for row 4-8 (geometry 2)	47
5.15 Fin efficiencies for geometry 2	48
5.16 $Nu \cdot Pr^{-\frac{1}{3}}$ vs. Re for geometry 3	49
5.17 Eu vs. Re for geometry 3	50
5.18 Comparison of the heat transfer coefficients for geometry 3 with four varying Reynolds number	51
5.19 Relative Deviation between simulated and experimental heat transfer coefficient for geometry 3, $\frac{\alpha_{o,sim}-\alpha_{o,exp}}{\alpha_{o,exp}} \cdot 100\%$	52
5.20 Ratio between row heat transfer coefficient to the average heat transfer coefficient for row 4-8 (geometry 3)	52
5.21 Fin efficiencies for geometry 3	53
5.22 $1/\lambda_f$ vs. fin efficiencies η for geometry 1 ($Re = 9430$)	54
5.23 $1/\lambda_f$ vs. fin efficiencies η for geometry 2 ($Re = 9818$)	55
5.24 $1/\lambda_f$ vs. fin efficiencies η for geometry 3 ($Re = 9000$)	55
5.25 Schematic explaining formation of horseshoe vortex at the leading part of the tube (taken from Hofmann [10])	56
5.26 Velocity distributions between the fins of second row in symmetry plane at low and high Reynolds number for geometry 1	58
5.27 Velocity distributions between the fins of second row in symmetry plane at low and high Reynolds number for geometry 2	59
5.28 Velocity distributions between the fins of second row in symmetry plane at low and high Reynolds number for geometry 3	60
5.29 Velocity profile in mid-plane between fins for geometry 1	61
5.30 Velocity profile in mid-plane between fins for geometry 2	62
5.31 Velocity profile in mid-plane between fins for geometry 3	63
5.32 Turbulence in the finned tube bundle for geometry 1	64
5.33 Turbulence in the finned tube bundle for geometry 3	65
5.34 Wall temperature for $Re = 4397$ (top) and $Re = 26086$ (bottom) for geometry 1	67
5.35 Wall temperature for $Re = 5793$ (top) and $Re = 26017$ (bottom) for geometry 2	68
5.36 Wall temperature for $Re = 4802$ (top) and $Re = 25090$ (bottom) for geometry 3	69
5.37 Temperature distributions between the fins upstream of second row in symmetry plane at low and high Reynolds number for geometry 1	70

5.38 Temperature distributions between the fins upstream of second row in symmetry plane at low and high Reynolds number for geometry 2 71

5.39 Temperature distributions between the fins upstream of second row in symmetry plane at low and high Reynolds number for geometry 3 72

5.40 Wall heat flux at the fins for geometry 1 73

5.41 Wall heat flux at the fins for geometry 2 74

5.42 Wall heat flux at the fins for geometry 3 75

List of Tables

- 3.1 Overview of the setup of the relevant studies 11
- 4.1 The geometries considered in this study 20
- 4.2 Boundary conditions of the relevant studies (taken from Eide [7]) 28
- 4.3 The tested meshes for the mesh sensitivity study 32
- 5.1 Deviations in Nusselt number from the benchmark mesh, $\frac{Nu_{case}-Nu_{bench}}{Nu_{bench}} \cdot 100\%$ 36
- 5.2 Deviations in Euler number from the benchmark mesh, $\frac{Eu_{case}-Eu_{bench}}{Eu_{bench}} \cdot 100\%$ 36
- A.1 Coefficients for eq. A.1 80
- A.2 Coefficients for eq. A.3 and A.4 81

Chapter 1

Introduction

Production of oil and gas have a high power demand, and gas turbines are used for power generation. The most key requirements for offshore power generation have traditionally been high power to weight ratio and easy maintenance. Combined cycle gas turbines are being introduced as more importance is directed towards power efficiency. Currently work is being done to develop new, compact heat exchangers solutions for gas turbine exhaust gases. Because of the low heat transfer coefficient of the exhaust gas, finned tubes have been selected as good candidates, due to the high specific heat transfer surface.

At NTNU tests have been performed on finned tube bundles, and experimental data are available [11]. This thesis focuses on creating a numerical model which corresponds to these experimental tests. First of all the results from this model can help validate the experimental results. An important aspect of a numerical model is that visualizations of the fluid flow and heat transfer can be made. These visualizations can be used to investigate qualitatively the different characteristics effects happening in a compact fin-tube heat exchanger.

The ultimate goal of this thesis is to further increase the understanding of fluid flow and heat transfer in finned tube bundles. This will be done by setting up a CFD-model for fluid flow through a finned tube bundle and analysis will be performed. Further the numerical results will be compared with the experimental data available, as well as semi-empirical correlations found in the literature.

1.1 Report structure

- Firstly, an introduction to the theory of finned tube heat exchangers is given in chapter 2. The variables that characterizes a finned tube bundle is given, as well as relevant dimensionless numbers.
- In chapter 3 the theory on numerical modeling of finned tube bundles is presented.

- Chapter 4 gives a walk-through of the numerical model created in this study.
- In chapter 5 the results from the simulations are presented and compared with the experimental data and semi-empirical correlations from published literature.
- In chapter 6 conclusions from the study are drawn. Chapter 7 gives suggestions for further work.

Chapter 2

Theory on Finned Tube Heat Exchangers

Finned tube heat exchangers are a good option to exchange heat between a liquid and a gas. The biggest thermal resistance in these cases is the gas-side heat transfer coefficient. It is therefore important to increase this value in order to efficiently extract the heat from the flue gas, which in this study will be taken as dry air. This is done by attaching metal fins to the pipes.

There are two types of fins, namely solid and serrated fins (see fig. 2.1). A solid fin is made



Figure 2.1: Tubes with serrated fins (left) and solid fins (right). Courtesy: Delfintubes

by winding a piece of metal around the tube. For a serrated fin, the metal is partially split before it is winded around the tube. There are three different welding methods for

attaching the fins to the tubes. Fin attachments can be of type I-foot, L-foot or U-foot (see fig. 2.2). In the present study only I-foot fins will be considered.

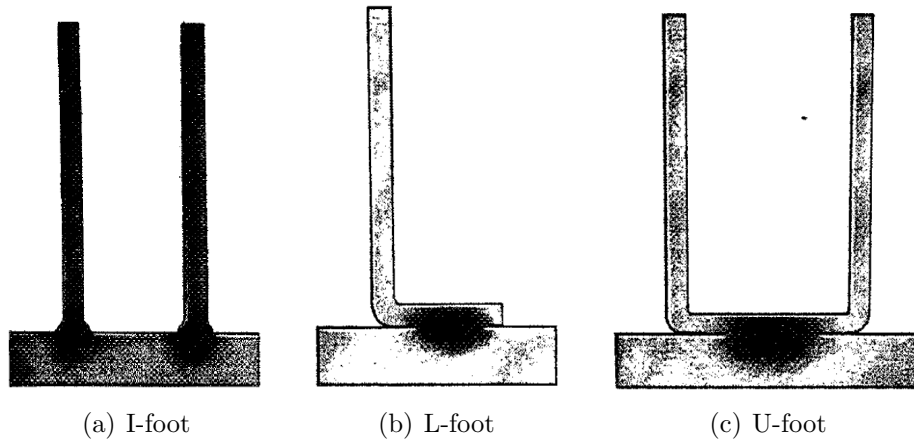


Figure 2.2: Attachment methods for fins (taken from ESCOA [8])

2.1 Basic variables

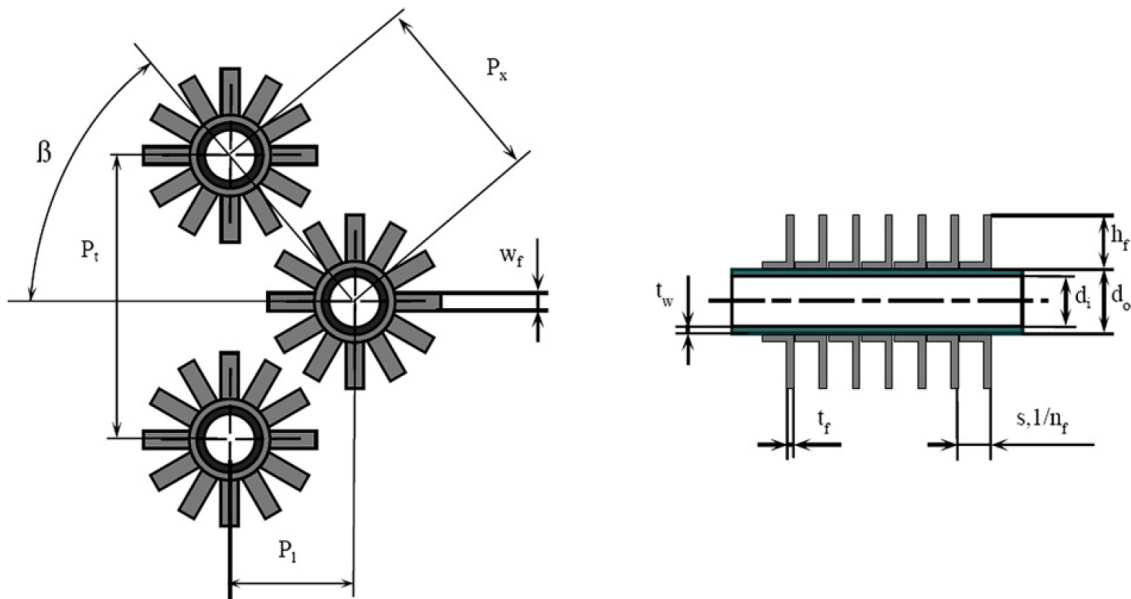


Figure 2.3: Finned tube layout (taken from Næss [20])

Geometry variables

Fig. 2.3 shows the geometrical variables that affects the heat transfer and pressure drop in a serrated finned tube bundle according to Webb and Kim [24]. The same variables are used for solid fins, except that the fin segment width w_f is dropped out. In the present

study the fin pitch s in fig. 2.3 will be denoted p_f . The fin spacing is denoted s_f .

Flow variables

Further Webb and Kim [24] identified five flow variables which to be taken in to consideration:

- Air density, ρ_{air}
- Air dynamic viscosity, μ_{air}
- Air thermal conductivity, λ_{air}
- Air specific heat capacity, $C_{p,air}$
- Air velocity, u_{air}

2.2 Dimensionless numbers

Dimensionless numbers are used to characterize the heat exchanger. In order to characterize the flow conditions, the Reynolds number is introduced. The Reynolds number (Re) is based on the outer diameter of the tube, and the mass flux through the narrowest free flow area within the tube bundle. This is consistent with the relevant literature.

$$Re = \frac{\dot{m}''_{air} \cdot d_o}{\mu_{air}} \quad (2.1)$$

For the geometries considered in the present study, the narrowest free flow area is the area between two tubes in the transversal direction, and can be defined as

$$F_{f,min} = F_t = p_f \cdot (P_t - d_o) - 2h_f \cdot t_f \quad (2.2)$$

For heat transfer correlations, the Nusselt number (Nu) is used.

$$Nu = \frac{\alpha_o d_o}{\lambda_{air}} \quad (2.3)$$

Here α_o is the air-side, actual heat transfer coefficient. See section 4.6 for how the gas-side heat transfer coefficient is derived.

According to Næss [20] the total pressure drop across a horizontal tube bundle may be obtained from

$$\Delta P = \Delta P_f + \Delta P_a \quad (2.4)$$

Here ΔP_a is the pressure change due to flow acceleration/deceleration associated with changes in flow area and fluid density. ΔP_f is the core frictional pressure loss. For pressure drop correlations, the Euler number (Eu) is used.

$$Eu = \frac{2\Delta P \cdot \rho_{air}}{N_L \cdot (\dot{m}''_{air})^2} \quad (2.5)$$

N_L is the number of tube rows in the longitudinal direction.

2.3 Tube bundle arrangement

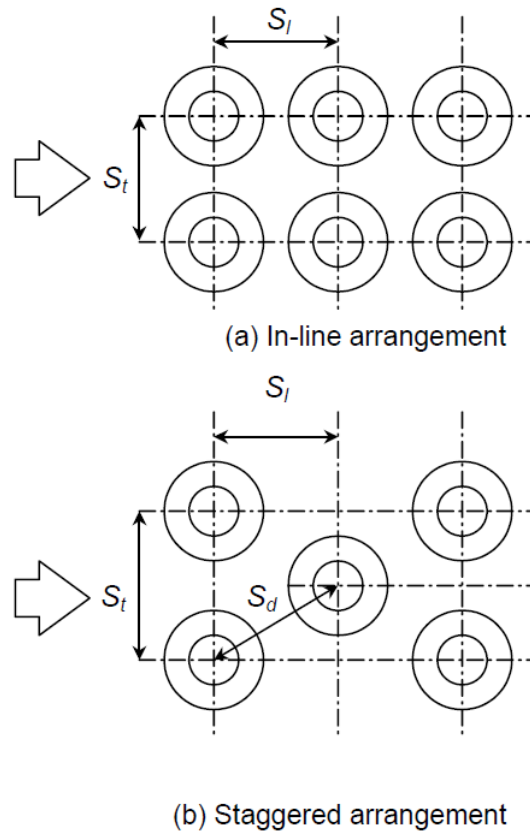


Figure 2.4: Arrangements of tubes in bundles. Taken from Mon [16]

There are two arrangements of tube bundles to consider, namely in-line and staggered arrangement, see fig. 2.3. Note that in the present study S_t and S_l are referred to as P_t and P_l . Earlier studies like Weierman [25], Mon [16] and Hofmann [10] have shown how the tube arrangement influence heat transfer and pressure loss in a tube row. Generally the finned tube rows creates a wake zone behind the row which then affects the consecutive rows. Mon [16] found that the heat transfer coefficient for all in-line rows was lower than compared to the staggered arrangements. This is mainly due to the by-pass effect of the flow experienced in an in-line arrangement. In the present study only staggered

arrangements will be considered.

2.4 Fin efficiency

When dealing with heat transfer for extended surfaces or fins it is important to account for the conductive resistance of the fin material. The ideal situation would be to have a large thermal conductivity in the fin material to minimize temperature variations from the fin base to the fin tip. The maximum possible heat transfer enhancement would occur if the fin had infinite thermal conductivity which would mean that the entire fin would be at the temperature of the base surface. Incropera et al. [12] presents how the theoretical fin efficiency can be calculated from the solution of a heat conduction equation for uniform extended surfaces:

$$\frac{d^2 T_f}{dx^2} - m^2(T_f - T_\infty) = 0 \quad (2.6)$$

$$m^2 \equiv \frac{\alpha_o P}{\lambda_f A_c}$$

Here α is the actual heat transfer coefficient, k is the fin thermal conductivity, P is the fin perimeter, A_c is the cross sectional area of the fin, T_f is the fin temperature and T_∞ is the gas-side fluid temperature. As can be seen from eq. (2.6), Incropera et al. [12] assumes that the heat transfer coefficient is uniform across the fin. Further it is assumed that there is no resistance between the fin and the tube and that the heat transfer at the fin tip is negligible. The boundary conditions can then be specified:

$$T_f(x = 0) = T_0 \quad (2.7)$$

$$\left. \frac{d}{dx} \left(\frac{T_f - T_\infty}{T_0 - T_\infty} \right) \right|_{x=h_f} = 0 \quad (2.8)$$

Here T_0 is the fin root temperature.

According to Incropera et al. [12] the fin efficiency can be defined as

$$\eta \equiv \frac{\dot{Q}_f}{\dot{Q}_{max}} = \frac{\dot{Q}_f}{\alpha A_f (T_b - T_\infty)} \quad (2.9)$$

In order to solve the fin efficiency for plain fins the use of Bessel functions is required. In

Incropera et al. [12] the fin efficiency for an annular fin is given as

$$\eta_{th} = C_2 \frac{K_1(mr_1)I_1(mr_{2c}) - I_1(mr_1)K_1(mr_{2c})}{I_0(mr_1)K_1(mr_{2c}) + K_0(mr_1)I_1(mr_{2c})} \quad (2.10)$$

$$C_2 = \frac{2r_1/m}{r_{2c}^2 - r_1^2} \quad (2.11)$$

Here r_1 is the tube outside radius. $r_{2c} = D_f/2 + t_f/2$. I_0 and K_0 are modified, zero-order Bessel functions. I_1 and K_1 are modified, first-order Bessel functions. Hashizume et al. [9] similarly gives an analytical solution of the fin efficiency for serrated fins using the same assumptions as Incropera et al. [12]. This solution also requires modified Bessel functions. The Bessel functions can easily be implemented in Microsoft Excel.

Uneven heat transfer and corrected fin efficiency

Due to the formation of vortices and boundary layers, the assumption that the heat transfer coefficient is uniform across the fin does not hold in actual situations. Experiments have shown lower heat transfer coefficients than predicted theoretically. Weierman [25] found a nonuniform heat transfer correction to correct for this. Weierman [25] found that the “actual”/corrected fin efficiency differs from the theoretical fin efficiency by a factor E . The actual fin efficiency can then be expressed:

$$\eta_{c,W} = E \cdot \eta_{th} \quad (2.12)$$

Weierman [25] found that the factor can be approximated as $E_{sol} = 0.7 + 0.3 \cdot \eta_{th}$ for solid fins and $E_{ser} = 0.9 + 0.1 \cdot \eta_{th}$ for serrated fins. As seen from the expression, these correction factors do not consider the geometry of the fins or flow parameters. Hashizume et al. [9] performed experiments on serrated tubes in a staggered arrangement to develop a correction factor for the fin efficiency. This resulted in a correction factor dependent on the geometry of the finned tube, the fin parameter m as well as the Reynolds number.

$$\psi_H = 1 - \left[0.016 \left(\frac{h_s}{w_f} \right) + 0.14 \left(\frac{D_f}{d_o} \right)^{2.7} \cdot (1 - 0.097 \ln Re) \right] \cdot mh_f \quad (2.13)$$

The corrected fin efficiency is then calculated

$$\eta_{c,H} = \psi_H \cdot \eta_{th} \quad (2.14)$$

It should be noted that Hashizume et al. [9] defines the applicable range as $1.80 \leq \frac{d_f}{d_o} \leq 2.15$, $0 \leq \frac{h_s}{h} \leq 0.86$, $0 \leq \frac{h_s}{w_f} \leq 2.60$, $5 \cdot 10^3 \leq Re \leq 5 \cdot 10^4$ and $0 \leq (mh_f) \leq 2.5$.

2.5 Correlations from the literature

Various different semi-empirical correlations exist for estimating the Nusselt number as well as the Euler number for a finned tube bundle. These correlations generally do not agree with each other, and can vary as much as 30 percent from each other [6]. However, the correlations can give an indication on the validity of the numerical results, and are therefore included in this study. See Appendix B for the correlation used in this study.

Chapter 3

Numerical Considerations

For the numerical model set up in this study the software package ANSYS Fluent is used. FLUENT uses the Finite Volume Method (FVM). In order to solve a problem the relevant geometry needs to be put in a grid system of small control volumes. The FVM solves the relevant partial differential equation on these finite volumes. For this study the flow in the finned tube bundle is considered to be turbulent, since higher Reynolds numbers are considered ($5000 \leq Re \leq 30000$). This means a turbulence model is required. This chapter presents the background theory on the models and sub-models used in this study. The chosen models will be justified based on characteristic traits of the models as well as results from earlier studies found in the relevant literature. The first three sections are modified versions from the project work (Eide [7]).

3.1 Turbulence models

Unfortunately there is no single turbulence model which is universally accepted as being the best model for all classes of problems. Important factors when choosing a model are physics of the flow, level of accuracy required, available computational resources and time available for the simulation. Each model has its capabilities and limitations. According to Mon [16] two types of turbulence models are relevant for numerical modeling of a finned tube bundle, namely Large Eddy Simulation (LES) and Reynolds averaging (RANS). [16] points out that the LES model requires extremely fine grids and therefore a much longer computing time than RANS. Tab. 3.1 gives an overview on the turbulence models used in the earlier relevant studies on numerical modeling of finned tube bundles. As can be seen [16], [15], [10], [5] and [6] uses a variant of the RANS turbulence model. [14] does not implement a turbulence model since the flow is considered to be laminar. Based on the findings in the relevant literature as well as limitations to computational capacity and time, it is decided to use a RANS turbulence model for this study.

Study	Solid or serrated fins?	Inline or staggered layout?	Reynolds range	Turbulence model	Near-wall treatment
Mon [16]	Solid	Both	$5,000 \leq Re \leq 70,000$	RNG $k - \epsilon$	Standard wall functions
McIlwain [15]	Solid	Both	$4,000 \leq Re \leq 16,000$	Realizable $k - \epsilon$	Enhanced wall treatment
Hofmann [10]	Both	Both	$3,500 \leq Re \leq 35,000$	RNG $k - \epsilon$	Enhanced wall treatment
Bharathan et al. [5]	Serrated	Staggered	$5,000 \leq Re \leq 35,000$	RNG $k - \epsilon$	Enhanced wall treatment
Cleirigh and Smith [6]	Both	Staggered	$5,000 \leq Re \leq 30,000$	SST $k - \omega$	Low-Re (near-wall model)
Lemouedda et al. [14]	Both	Staggered	$600 \leq Re \leq 2,600$	-	-

Table 3.1: Overview of the setup of the relevant studies

3.1.1 Reynolds Averaged Navier-Stokes (RANS) Turbulence Model

According to [2] RANS models are often used for computing complex turbulent industrial flows and is considered to be the most economic approach. In Reynolds averaging, the variables in the Navier-Stokes equation are decomposed in to averaged components and fluctuating components. For the velocity components:

$$u_i = \bar{u}_i + u'_i \quad (3.1)$$

Here \bar{u} is the averaged velocity, while u'_i is the fluctuating velocity component. Inserting the averaged components in to the continuity equation and Navier Stoke equation yields the RANS equations. Here, the bar notation \bar{u} is dropped for simplicity.

$$\frac{\partial \rho}{\partial t} + \frac{\partial}{\partial x_i}(\rho u_i) = 0 \quad (3.2)$$

$$\frac{\partial}{\partial t}(\rho u_i) + \frac{\partial}{\partial x_j}(\rho u_i u_j) = -\frac{\partial p}{\partial x_i} + \frac{\partial}{\partial x_j} \left[\mu \left(\frac{\partial u_i}{\partial x_j} + \frac{\partial u_j}{\partial x_i} - \frac{2}{3} \delta_{ij} \frac{\partial u_l}{\partial x_l} \right) \right] + \frac{\partial}{\partial x_j} (-\rho \overline{u'_i u'_j}) \quad (3.3)$$

New terms now appears, namely the Reynold stresses, $-\rho \overline{u'_i u'_j}$. These terms represent the effects of turbulence. It is these terms which must be modeled in the turbulence models in order to close eq. (3.3) [3]. This is done by introducing various transport equations, as well as turbulent viscosity, μ_t . Turbulent viscosity differs from molecular viscosity in the way that it is a property of the flow, not the physical property of the fluid.

Even though simplifications are done, the models often provide the required level of accuracy [3]. None of the models are universal, so it is necessary to do evaluations on which of the models that are the best fit for a given application. Both Mon [16] and Hofmann [10] uses the RNG $k - \epsilon$ model. Both studies point out that while the standard $k - \epsilon$ model fails to predict the wake created behind the tubes, the RNG modification performs well for finned tube bundles. The RNG $k - \epsilon$ model is reported to also predict well low Reynolds effects near the walls. For theory on the RNG $k - \epsilon$ model see [3].

Cleirigh and Smith [6] is the only study that uses the SST $k - \omega$ turbulence model. Cleirigh and Smith [6] states that “the SST $k - \omega$ turbulence model more accurately predicts flow separation in the presence of adverse pressure gradients, when compared to the Wilcox $k - \omega$ model and the $k - \epsilon$ model.” In the start of the present study both the RNG $k - \epsilon$ model and the SST $k - \omega$ model were tested. It was found that the SST $k - \omega$ turbulence model more accurately predicted the pressure loss in the tube bundle when compared to the experimental data and semi-empirical correlations. It was therefore decided to use the SST $k - \omega$ model.

The SST $k - \omega$ model

The $k - \omega$ models are two-equation models. According to [3] the standard $k - \omega$ model is based on transport equations for turbulence kinetic energy, k (3.4) and the specific dissipation rate, ω (3.5). The turbulence kinetic energy is defined as the mean kinetic energy per unit mass associated with turbulent eddies in the turbulent flow [18].

$$\frac{\partial}{\partial t}(\rho k) + \frac{\partial}{\partial x_i}(\rho k u_i) = \frac{\partial}{\partial x_j} \left(\Gamma_k \frac{\partial k}{\partial x_j} \right) + G_k - Y_k + S_k \quad (3.4)$$

$$\frac{\partial}{\partial t}(\rho \omega) + \frac{\partial}{\partial x_i}(\rho \omega u_i) = \frac{\partial}{\partial x_j} \left(\Gamma_\omega \frac{\partial \omega}{\partial x_j} \right) + G_\omega - Y_\omega + S_\omega \quad (3.5)$$

These equations are implemented in the FLUENT software-package and are taken from the Fluent Theory Guide [3]. G_k represents the generation of turbulence kinetic energy due to mean velocity gradients. G_ω represents the generation of ω . Γ_k and Γ_ω represent the effective diffusivity of k and ω , respectively. Y_k and Y_ω represent the dissipation of k and ω due to turbulence. S_k and S_ω are user-defined terms. It was decided for this study to retain the standard values for the coefficients used in ANSYS Fluent.

Further, the effective diffusivities are given by:

$$\Gamma_k = \mu + \frac{\mu_t}{\sigma_k} \quad (3.6)$$

$$\Gamma_\omega = \mu + \frac{\mu_t}{\sigma_\omega} \quad (3.7)$$

σ_k and σ_ω are turbulent Prandtl numbers. The turbulent viscosity is computed by combining k and ω :

$$\mu_t = \alpha^* \frac{\rho k}{\omega} \quad (3.8)$$

Without going into further detail, the coefficient α^* damps the turbulent viscosity, causing a low-Reynolds number correction. For high Reynolds number, $\alpha^* = \alpha_\infty^* = 1$. For a more detailed description, see the Fluent Theory Guide [3].

According to the Fluent User's Guide [2], these models offer several advantages to the ϵ -equation. The most important one is that the ω -equation can be integrated without additional terms through the viscous sublayer. The models are also considered to better predict adverse pressure gradient boundary layer flows and separation. The major challenge with using these models is the strong sensitivity of the solution, depending on the free-stream values of k - and ω - outside the shear layer. The Fluent User's Guide [2] therefore generally does not recommend using these models in ANSYS Fluent.

A specific $k - \omega$ model, namely the Shear-Stress Transport (SST) $k - \omega$ model has been developed to avoid the free-stream sensitivity. The idea behind the SST-model is to effectively blend the robust and accurate formulation of the $k - \omega$ model in the near-wall region (viscous sublayer) and at the same time get the freestream independence of the $k - \epsilon$ model in the far field. This is done by combining elements of the ϵ - equation and the ω -equation. Compared to the standard $k - \omega$ model, the transport equation for kinetic energy, k (3.4) is unchanged. (3.5) is modified to (taken from [3]):

$$\frac{\partial}{\partial t}(\rho\omega) + \frac{\partial}{\partial x_j}(\rho\omega u_j) = \frac{\partial}{\partial x_j} \left(\Gamma_\omega \frac{\partial \omega}{\partial x_j} \right) + G_\omega - Y_\omega + D_\omega + S_\omega \quad (3.9)$$

D_ω is the damped cross-diffusion derivative term. This term is a result of blending the standard $k - \omega$ and standard $k - \epsilon$ models together. All modeling constants are different compared to the standard model.

Furthermore the standard $k - \omega$ model and the transformed $k - \epsilon$ model are both multiplied by a blending function which activates the $k - \omega$ model in the near-wall regions and then activates the transformed $k - \epsilon$ model away from the walls. The definition of the turbulent viscosity is modified, in order to account for the transport of the turbulent shear stress [3].

The SST model is one of the most widely used model for aerodynamic flows [2]. It is considered to better predict the details of the boundary layer characteristics than the Spalart-Allmaras model. Within the $k - \omega$ model family the Fluent User's Guide [2] recommends using the SST-model.

3.2 Near-wall treatment

When modeling turbulent flows, proper near-wall treatment is of great importance. The no-slip condition always applies, but the turbulence is also changed by the presence of the wall in non-trivial ways.

3.2.1 Near-wall regions for turbulent flows

Very close to the wall, viscous damping reduces the tangential velocity fluctuations. This region is called the viscous sublayer. Here the flow is almost laminar and the molecular viscosity plays a dominant role in momentum and heat transfer. Toward the outer part of the near-wall region, the turbulence rapidly plays a bigger role. A fully turbulent region occurs because of this production of turbulent kinetic energy due to the large gradients in mean velocity.

Between the viscous sublayer and the fully turbulent region there is an interim region, where the effects of molecular viscosity and turbulence are equally important. Fig. 3.1 shows an overview of the different regions which must be treated in a correct manner.

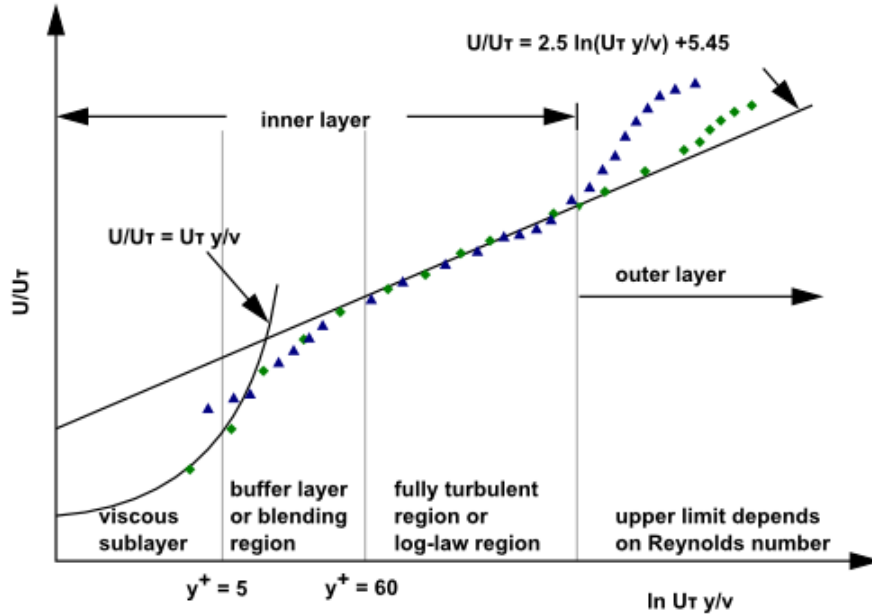


Figure 3.1: Subdivision of the near-wall region. Taken from [3]

Here, y^+ is the dimensionless distance from the wall. It is based on the distance from the wall to the first node as well as the wall shear stress, and is defined as:

$$y^+ = \frac{\rho u_\tau y}{\mu}, \quad u_\tau = \sqrt{\frac{\tau_w}{\rho}} \quad (3.10)$$

Here u_τ is the friction velocity. τ_w is the absolute value of the wall shear stress. y is the distance from the wall to the first node [3].

3.2.2 Wall functions vs. near-wall model

According to [3] There are normally two way of handling the near-wall effects, namely wall functions and near-wall modeling, see fig. 3.2.

Near-wall modeling

According to [3] this approach modifies the turbulence models to enable the viscosity-affected region to be resolved with a mesh all the way to the wall, including the viscous sublayer. Normally this means that $y^+ \approx 1$ is required. Also it is important to have an adequate number of cells in the buffer and sublayer (20 cells are considered to be desirable [3]). A good way to ensure this is to create prism layers under the grid generation. To check if the buffer and sublayer are properly covered, looking at the turbulent viscosity after obtaining a solution can give the answer. Turbulent viscosity has a maximum in the middle of the boundary-layer, which can give an indication of the thickness of the boundary-layer (twice the location of the maximum gives the boundary-layer edge).

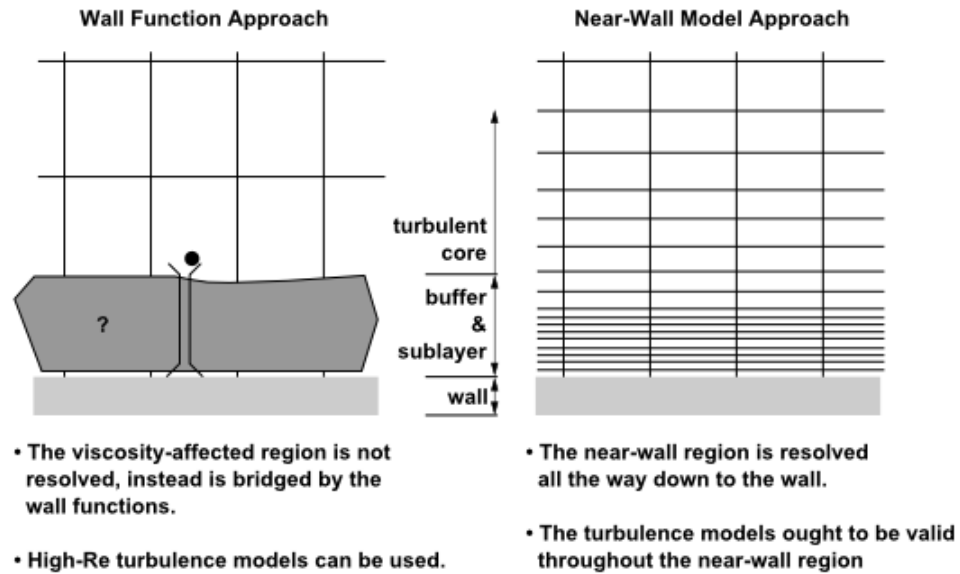


Figure 3.2: Near wall treatments (applied in ANSYS FLUENT). Taken from [3]

Wall functions

This approach does not resolve the viscosity-affected buffer and sublayer. Semi-empirical formulas called “wall functions” are used in stead. Traditionally the numerical results deteriorate if the mesh becomes to fine near the wall ($y^+ < 15$) when using wall functions [3]. This is because of unbounded errors in wall shear stress and wall heat transfer. During the last years, actions have been taken to offer more advanced wall functions, offering y^+ -independent formulations. This new method has become default for ω -equation based turbulence models. This method is called the Enhanced Wall Treatment (EWT). EWT is special by way of it combining wall functions with a two-layer model. If the near-wall mesh is fine enough to be able to resolve the sublayer, near-wall modeling will be applied. If this is not the case, wall functions are used [3].

Since the SST $k - \omega$ turbulence model is used in the present study, EWT will be applied.

3.3 Solver methods

In FLUENT, two numerical methods can be chosen: Pressure-based solver and density-based solver. Traditionally, the pressure-based solver was developed for low-speed incompressible flows and the density-based solver for high-speed compressible flows. Today the solvers have been extended and reformulated to operate for a wider range of flow conditions. Both solvers obtain the velocity field from momentum equations. The main difference between them is how the density and pressure field is obtained [3].

The density-based solver uses the continuity equation to obtain the density and the equa-

tion of state for the pressure field. For the pressure-based solver the pressure field is obtained by solving a pressure correction equation which originates from continuity and momentum equations [3].

Both solvers use the Finite-Volume Method (FVM), but the method used to linearize and solve the discretized equations is different. For the present study the pressure-based solver is chosen. This solver is chosen because the flow in the finned tube bundle can be considered to be compressible, which is what the solver was originally designed for.

3.3.1 Pressure-based solver

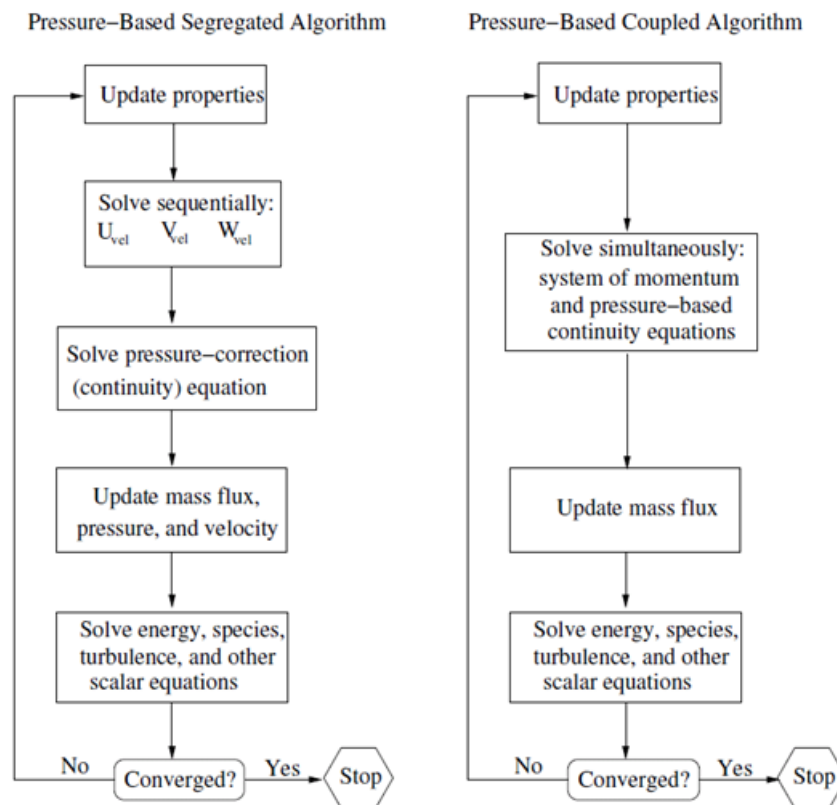


Figure 3.3: Overview of the pressure-based solution methods. Taken from [3]

Two algorithms for the pressure-based solver are available in FLUENT; a segregated and a coupled algorithm. Fig. 3.3 gives an overview of the major differences. These algorithms each have their own pros and cons. For the segregated algorithm, the discretized equations only need to be stored in the memory one at a time, which makes this algorithm memory-efficient. However this method causes a slower convergence. The opposite situation is the case for the coupled algorithm. Typically the memory requirement increases by 1.5 – 2 times that of the segregated algorithm. For the current study it was decided to use

the coupled algorithm, since enough memory was available at the computer used for the simulations.

Spatial discretization scheme

FLUENT gives the option to choose among several upwind schemes for the spatial discretization. Generally a first-order upwind scheme gives faster convergence than a second-order upwind scheme. However, a second-order upwind scheme naturally gives better accuracy of the solution [2]. Further [2] states that first-order schemes especially yield less accurate results on tri/tet meshes. Since this is the type of mesh that will be used in this study, a second order upwind scheme was chosen for all calculations.

Under-relaxation factors

The under-relaxation factors are kept at default values, as these values gave good convergence of the solution:

Pressure: 0.3

Density: 1

Body forces: 1

Momentum: 0.7

Turbulent kinetic energy: 0.8

Turbulent dissipation rate: 0.8

Turbulent viscosity: 1

Energy: 1

3.4 Ensuring convergence of the solution

An important aspect when performing numerical simulations is to judge whether the simulation is complete and converged, or not. There are several different ways to check this and ensure convergence. The most used method is to look at the residuals for each variable being solved. Residuals can be understood as the absolute error in the solution of a solved variable. In ANSYS FLUENT the default convergence criterion is defined using globally scaled residuals [2]. The residuals are scaled to easily judge convergence. The globally scaled residuals in FLUENT are defined as:

$$R^\phi = \frac{\sum_{cellsP} \left[\sum_{nb} a_{nb} \phi_{nb} + b - a_P \phi_P \right]}{\sum_{cellsP} [a_P \phi_P]} \quad (3.11)$$

This equation is valid for a general variable ϕ at a cell P . a_P is the center coefficient, while a_{nb} are the influence coefficients for the neighboring cells. b is the contribution of the constant part of the source term S_c in $S = S_c + S_P\phi$ [3].

The default convergence criterion in FLUENT states that (3.11) needs to be reduced to 10^{-3} for all solved equations, except the energy equation for which the criterion is set to 10^{-6} [2]. For most problems, the default convergence criterion is sufficient [2]. This criterion is therefore enforced for the simulations performed in this study.

It should be noted that the default convergence criterion may not always be appropriate [2]. The residuals are scaled based on the first initial guesses of the flow field. If a good initial guess is made the initial residual will be small, leading to large scaled residuals. This is typically a problem for the continuity residuals [2]. This also holds the other way around: A poor initial guess of the flow field will lead to high scale factors which means low scaled residuals. Scaled residuals may therefore not give the full picture. A good indicator to judge convergence is to look at how the residuals develop with the iterations. A good indication that convergence is reached is if the residuals continue to decrease or remain low for several iterations

Chapter 4

Numerical Modeling of Staggered Fin-Tube Bundles

The purpose of this chapter is to develop a numerical model for fluid flow through a finned tube-bundle. To make the model, five steps must be performed:

1. Create three dimensional geometry of the problem.
2. Define outer boundaries of the geometry and make a discrete representation of the geometry by generating a mesh.
3. Apply sub-models, boundary conditions and solution method.
4. Perform simulations
5. Post-process the result.

In this chapter steps 1. through 4. will be described. The data reduction necessary to process the data will also be presented.

4.1 Geometry

All geometries are made in the software package Solidworks. When creating the geometry the main focus was to make it similar to the geometry used in the experimental tests [11]. This means that eight longitudinal tube rows are made. According to Næss [20]

Geom.	Fin type	d_o [mm]	p_f [mm]	t_f [mm]	h_f [mm]	h_s [mm]	w_f [mm]	P_l [mm]	P_t [mm]
1 (6)	Solid	13.5	3.32	0.5	10	-	-	33.5	38.7
2 (2)	Solid	31.75	3.72	1	18	-	-	60.41	69.75
3 (5)	Serrated	19.05	3.61	1	10	5	4.5	34.58	44.05

Table 4.1: The geometries considered in this study

this is sufficient to obtain representative heat transfer and pressure drop data. In order to reduce the computational calculation time, only one fin pitch is modeled when creating the geometry. This is consistent with earlier numerical investigations on finned tube bundles ([16],[10], [6]) and has proven to give good results. Further two tube rows are modeled in the transversal direction with half tubes at the boundaries, in order to portray the staggered arrangements. This setup is consistent with [6] and [14]. See tab. 4.1 for the geometrical parameters and fig. 4.1 for the computational domain. In the geometry row in tab. 4.1 the numbers in parenthesis are the numbering of the geometries used in the experimental tests [11]. All three geometries have an arrangement angle $\beta = 30^\circ$. Geometry 1 is made out of aluminum, while geometry 2 and 3 is made out of carbon steel.

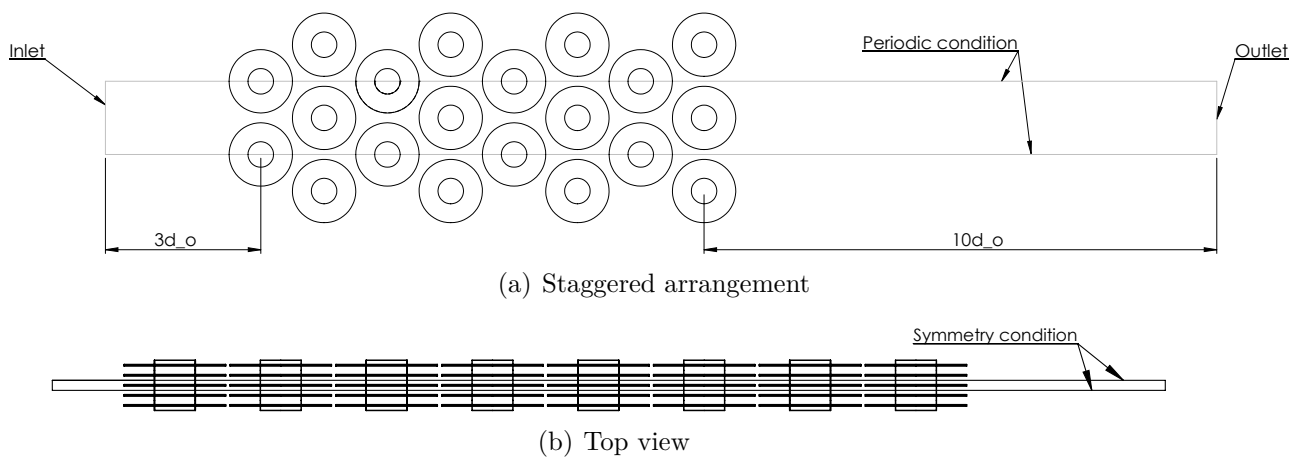


Figure 4.1: Computational domain

There is one important difference in geometry from the experimental setup. The fins in the experimental setup are twisted helically around the tube (case b. in fig. 4.2). In the simulations the geometry is simplified to annular fins around the tube (case a. in fig. 4.2). This will have an impact on pressure drop. More on this in the next chapter.

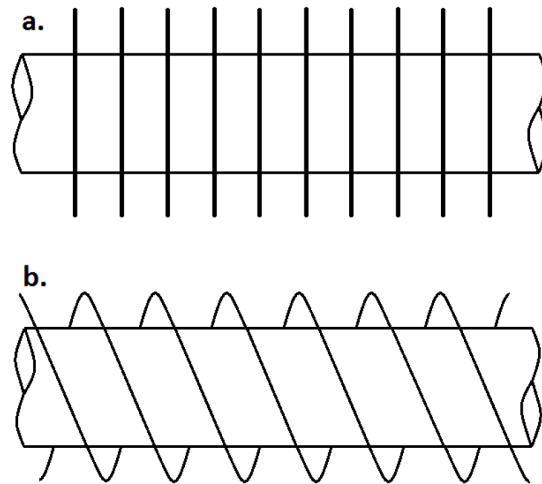


Figure 4.2: a. Individual annular fins; b. Helically wound fins (according to PFR [22])

4.2 Grid generation

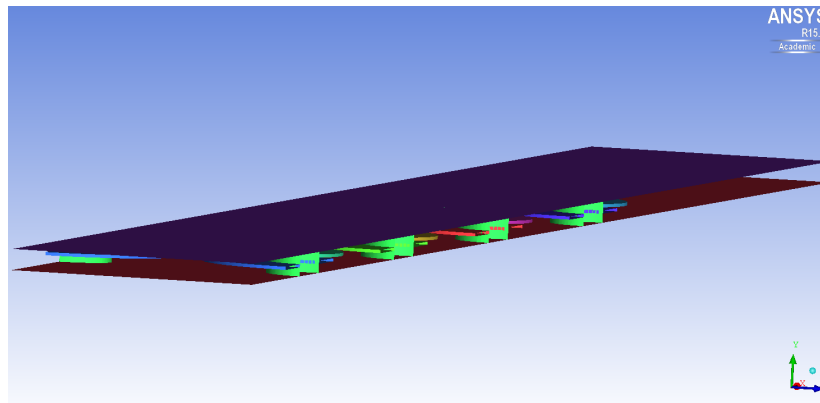
For the grid generation, the geometry files were imported from Solidworks to the meshing-software program ICEM CFD. First the outer boundaries were defined, see fig. 4.3. The distance from the inlet to the first tube was set to $3 \cdot d_0$. The distance from the last tube to the outlet was set to $10 \cdot d_0$ (see fig. 4.1(a)). The distance of $10 \cdot d_0$ to the outlet proved to be a sufficient distance for all three geometries to prevent back-flow at the outlet. An unstructured grid was chosen for the whole domain for all geometries.

4.2.1 Surface mesh

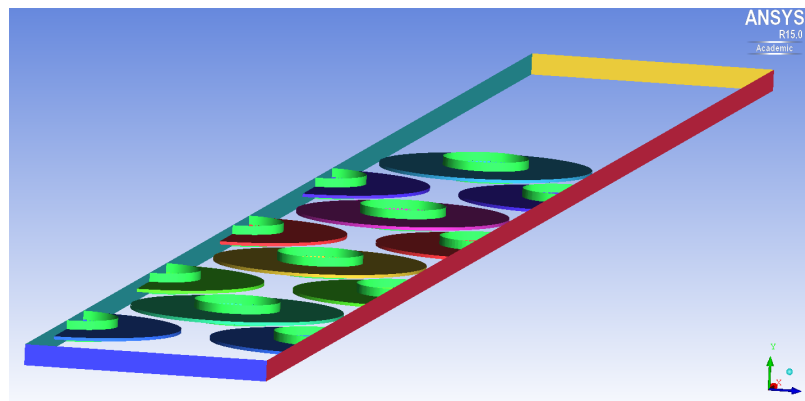
For the surfaces, a quad dominant mesh was chosen, see fig. 4.4. This mesh allows for several transitional triangles [1]. Since the given set-up contains sharp corners and edges this type of mesh is considered to deliver better result than a pure quad mesh [1]. Fig. 4.4 shows that ICEM mainly meshes the surfaces with triangles.

4.2.2 Volume mesh

For the meshing of volume elements (air-side volume and volume inside the fins) the mesh type Tetra/Mixed was chosen. For the volume in between the finned tubes a hexa-core is generated. According to [1] “a hexa-core retains the tri surface or prism mesh, deletes the existing tetra mesh, and remesh the volume interior with Cartesian meshing.” Hexa-core allows for a reduction in number of elements for quicker solver run time. Faster convergence is also experienced because of the structure of the Cartesian meshing. See fig. 4.5 for a cut plane of the air-side volume mesh. The inside of the tubes are not meshed.



(a) Top/bottom



(b) Inlet (dark blue), outlet (orange), sides (red/cyan)

Figure 4.3: Outer boundaries of mesh (for geometry 1)

4.2.3 Prism layers

In order to capture the near-wall effects (see section 3.2), prism layers are created near the finned tube surfaces. Based on the mesh sensitivity study (see section 4.7) six prism layers are created near the surfaces. First three layers were generated when creating the surface and volume mesh. Then the prism layers were split up in to six prism layers. This method proved to give the best quality of the mesh. See fig. 4.6 for a representation of the prism layers. Prism layers were not generated for tube bundle with serrated fins (geometry 3). Several attempts were made in order to grow prisms, but the quality of the mesh were insufficient to run simulations on. The main reason for the poor quality is the narrow areas between the fin serrations. A high quality mesh without prism layers was therefore chosen in stead. See fig. 4.7 for the near-wall meshing for geometry 3 without prism layers.

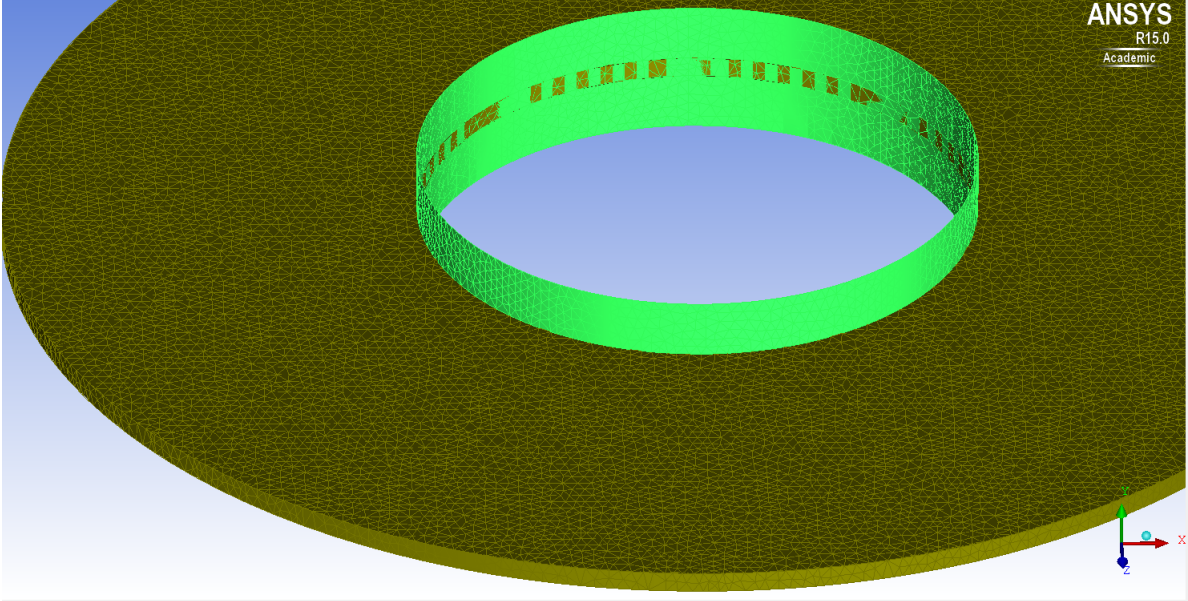


Figure 4.4: Surface mesh on tube wall and fin (geometry 1)

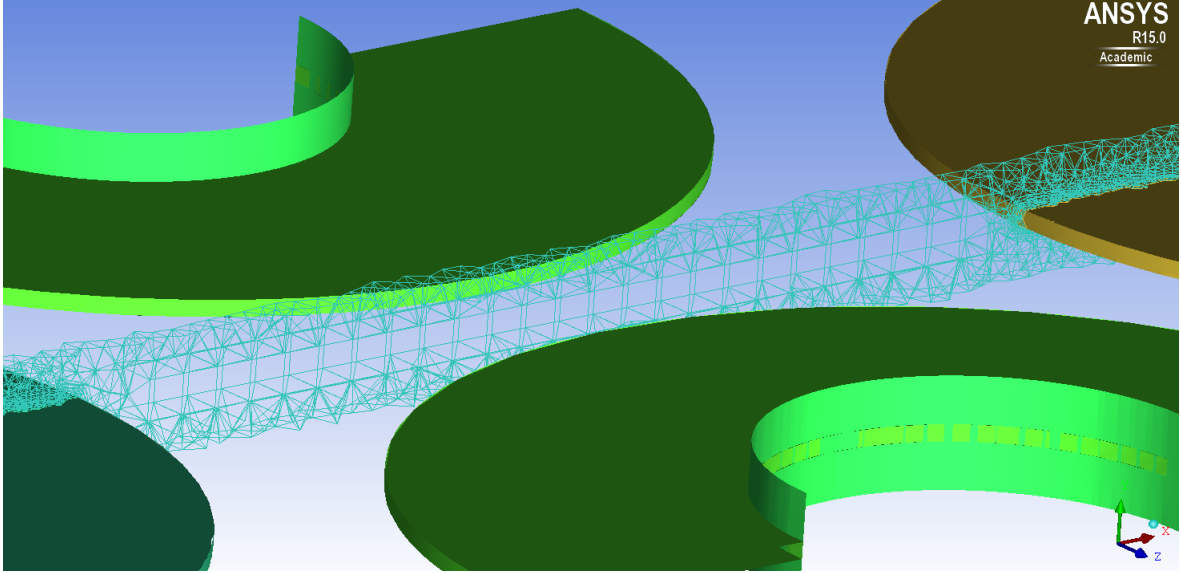


Figure 4.5: Cut plane of the air-side volume mesh (geometry 1)

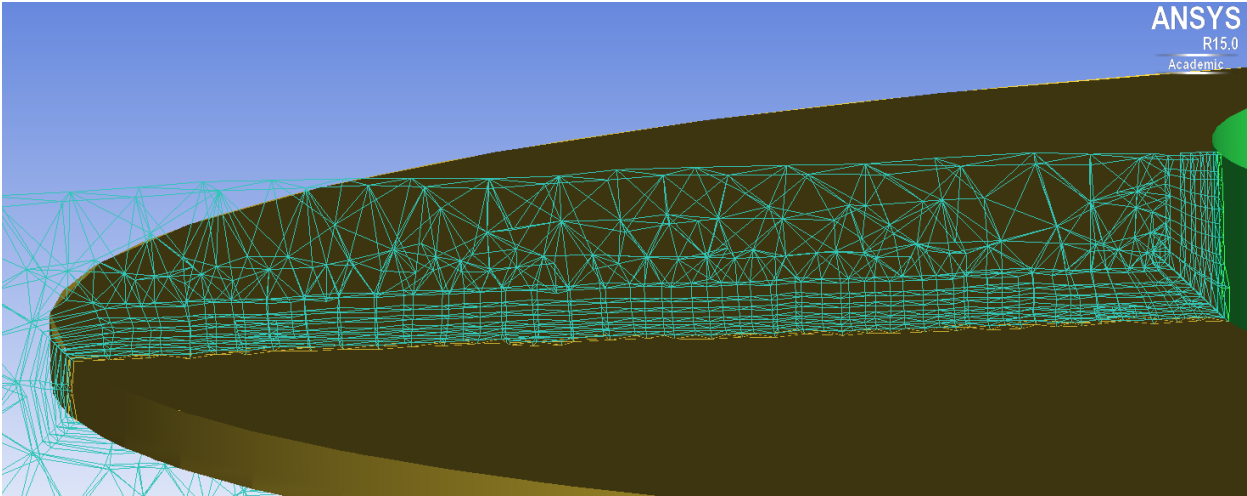


Figure 4.6: Prism layers near the finned tube surface (geometry 1)

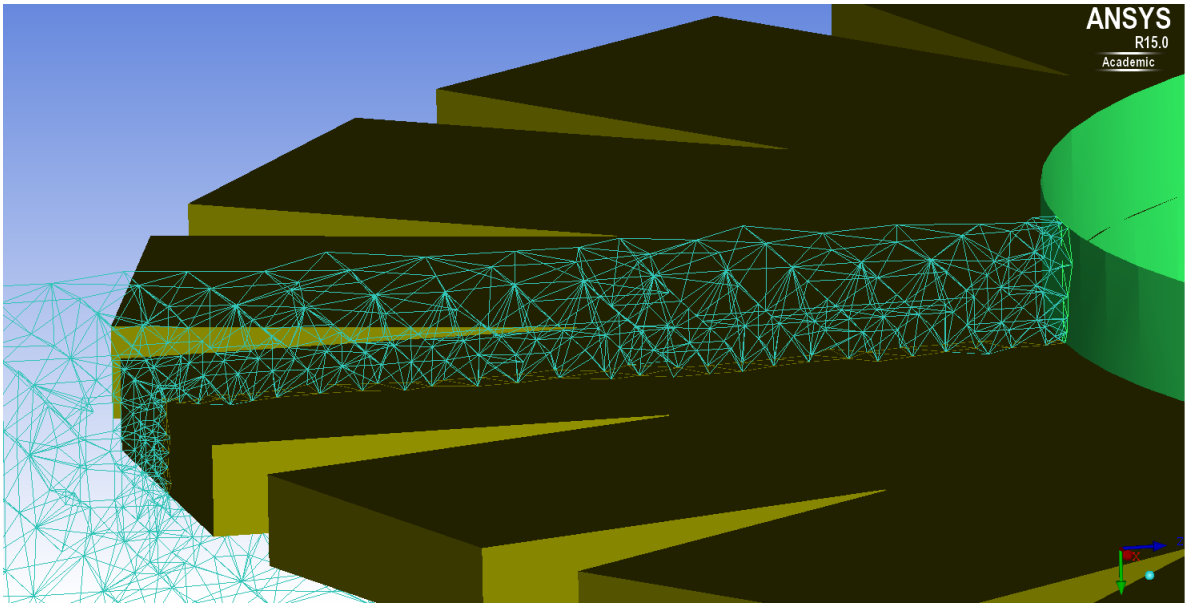


Figure 4.7: Near-wall meshing of serrated geometry (geometry 3)

4.3 Boundary Conditions

Top and bottom

The top and bottom outer boundary are set as symmetry boundary conditions. This means a zero flux of all quantities in the normal direction to the boundaries. As seen from tab. 4.2 symmetry conditions at the top/bottom have been used in earlier studies. Since most flow effects occur in the transversal and longitudinal direction, symmetry conditions at the top/bottom are considered to be adequate.

Left- and right-side

The left- and right-side boundaries are set as periodic. This means that the left- and right-side boundary must have an identical surface mesh. This is taken care of when meshing in Ansys ICEM. Periodic boundary conditions means that the conditions from the left-side boundary are reflected to the right-side boundary. This means that in theory an infinite sequence of fin-arrays are modeled. All fluid variables are conservative across the two boundaries. As seen from tab. 4.2 only Cleirigh and Smith [6] uses periodic conditions for the left/right side. Cleirigh and Smith [6] points out that the use of symmetry condition for these boundaries is unrealistic since that would mean the heat and mass flow normal to the boundaries would be constrained to zero.

Inlet and outlet

The inlet is chosen to be a velocity-inlet with inlet velocity $u_{in} = constant$, varying with different Reynolds numbers. Further, the inlet temperature is set to be $T_{in} = 400K$, which is approximately the inlet temperature of air used in the experimental tests at NTNU. The turbulent intensity at the inlet is set to $Tu = 5\%$. This is the default value in ANSYS Fluent and is characterized as medium intensity. Few investigations are done in the literature on the influence of upstream turbulence. In an earlier master thesis at NTNU by Klynderud [13] it was found that “the experimental results show no influence of the upstream flow conditions on the heat transfer coefficient development through the tube bundle”. It was further emphasized that there is a need for further investigations on the topic. The outlet is set as a pressure-outlet. The gauge pressure at the outlet is set to zero. This corresponds to atmospheric conditions. The backflow temperature is set to $350K$ in case of separation of the flow. Backflow was experienced sometimes during the calculations, but no backflow was present in the converged solutions.

Tube walls and fins

The tube walls were set as walls with no slip condition. Further, the tube wall temperature was set to $T_w = 300K = constant$. The fins were also set to no slip walls, but

with temperature dependent on the flow conditions and coupling between conduction and convection.

4.4 Physical properties

The gas-side fluid was modeled as dry air, using the incompressible ideal gas law for calculating the density. According to Hofmann [10] the ideal gas law can be used since the pressure variations are small enough, but the flow is temperature dependent. For the thermo-physical properties of the air, polynomial functions are used, see Appendix A. For the materials of the finned tubes the thermal conductivity is considered using functions found in the literature. See Appendix A.

4.5 Standard procedure for running simulations

After doing initial test simulations a systematic procedure was developed for running simulations for varying Reynold numbers. The procedure goes as follows.

1. Start FLUENT with 3D solver, double precision and parallel processing with all available processors.
2. Load the mesh in to FLUENT. Scale down the mesh from meter to millimeter. Check the mesh, concerning the dimension of the calculation domain, minimum/maximum volumes and number of nodes. Also see if the quality of the mesh is acceptable, by checking the minimum orthogonal quality.
3. Set the solver options, physical properties, turbulence model and solution method as described.
4. Under models, turn energy on, in order to solve the energy equations.
5. Set the boundary conditions as described. For varying Reynolds numbers only the inlet velocity is changed.
6. Initialize the solution by choosing hybrid initialization.
7. Set convergence criteria: Scaled residuals are set to 0.001, while the energy residual is set to $1e^{-6}$.
8. Calculate the solution and save the result.

In average a simulation took between 10-14 hours to reach the desired convergence criteria. The simulations were ran on a laptop with an i7-4600 CPU @ 2.10GHz 2.70GHz processor and 16 GB of RAM.

Study	Inlet	Outlet	Left/Right	Top/Bottom	Tube walls
Mon [16]	$T_{in} = 308.15K$, $Tu = 1\%$	Atmospheric pressure	Symmetry	Symmetry	$T_w = 283.15K = constant$
Mcllwain [15]	$T_{in} = 373.15K$, $Tu = 30\%$	Mass flow outlet	Symmetry	Symmetry	Unknown
Hofmann [10]	$T_{in} = 480K$, $Tu = 5\%$	Atmospheric pressure	Symmetry	Periodic interfaces	$T_w = 330K = constant$, $\alpha_i = 3860W/m^2K$
Bharathan et al. [5]	$T_{in} = 373K$, $Tu = 5\%$	Atmospheric pressure	Symmetry	Symmetry	$T_w = 293K = constant$, $\alpha_i = 3226W/m^2K$
Cleirigh and Smith [6]	$T_{in} = 673.15K$, Tu unknown	Atmospheric pressure	Periodic interfaces	Periodic interfaces	$T_w = 333.15K = constant$
Lemouedda et al. [14]	$T_{in} = 300K$	Atmospheric pressure	Adiabatic slip walls	Adiabatic slip walls	$T_w = 350K = constant$

Table 4.2: Boundary conditions of the relevant studies (taken from Eide [7])

All inlets are velocity inlets. $u_{in} = constant$ for varying Reynolds number

All outlets are pressure outlets, except for Mcllwain [15] which have a mass flow outlet

All tube walls and fin walls are no-slip walls.

The fins have varying temperature dependent on the flow conditions. Conduction and convection are coupled in all cases.

α_i is the inner heat transfer coefficient (liquid-side) of the tube.

4.6 Data reduction

4.6.1 Calculation of relevant parameters

All relevant data is gathered using the function calculator in CFD-post. For the calculation of the necessary flow variables (ϕ) at boundaries (for example at inlet and outlet), mass flow averaging was used. In ANSYS CFD-Post the *massFlowAve* function was used. According to [4] this function is evaluated with the formula:

$$massFlowAve(\phi) = \frac{\sum(m\phi)}{\sum m} \quad (4.1)$$

Here ϕ represents the flow variable being averaged. m represents the local mass flow. Each summation term is evaluated on and corresponds to, a node on the 2D locator/boundary [4]. Relevant temperatures and pressures were acquired using this function.

Some of the parameters needs to be evaluated with integrals. In ANSYS CFD-Post this data was obtained using the *areaInt* function. According to [4] the *areaInt* function integrates a variable over the specified 2D location. No specific axis is specified, so the integration is performed over the total face area.

To calculate the average fluid temperature of the fluid in the finned tube bundle, the *ave* function is used. According to [4] the *ave* function calculates the arithmetic average of a variable or expression on the specified location [4].

The mass flow at the inlet is gathered using the *massFlow* function which computes the mass flow through the specified 2D location [4].

4.6.2 Evaluation of physical properties

The thermal conductivity of air is evaluated at the arithmetic mean gas temperature of the air using the *ave* function. This is consistent with the semi-empirical correlations used in this study. This method is also used to find the average thermal conductivity of the finned tube material. The density, molecular viscosity and specific heat capacity of air is calculated by taking the arithmetic between the inlet and outlet using the *massFlowAve* function.

4.6.3 Heat transfer

To calculate the Nusselt number and fin efficiencies it was decided to use a method similar to the one used by Cleirigh and Smith [6]. The calculations are performed at each tube row.

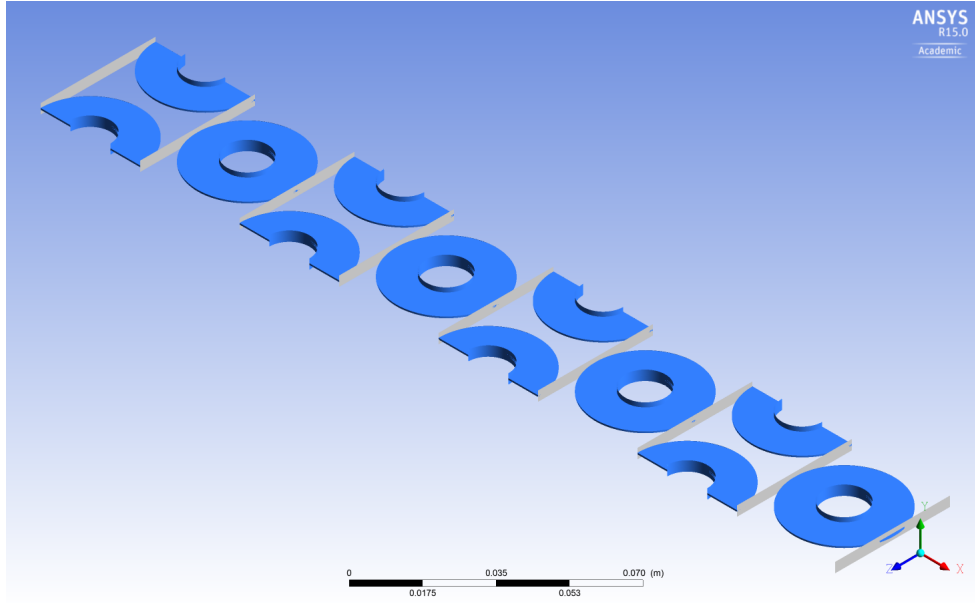


Figure 4.8: Planes at inlet/outlet of each tube row to calculate temperatures.

The heat transfer from the hot gas to the finned tubes was calculated using the integral of heat flux over the finned tubes.

$$\dot{Q}_{tot} = \int_{Fintube} \vec{q} \cdot \vec{n} dA \quad (4.2)$$

To calculate the overall heat transfer coefficient (U), the log-mean (LMTD) method was used. The logarithmic mean temperature difference for counter-current flow was chosen. According to Næss [20] this method has proven to be accurate to within 0.1% of the actual cross-counter-current arrangement mean temperature difference.

$$\Delta T_{LMTD} = \frac{T_{row,in} - T_{row,out}}{\ln \left(\frac{T_{row,in} - T_w}{T_{row,out} - T_w} \right)} \quad (4.3)$$

Here $T_{row,in}$ and $T_{row,out}$ is the bulk temperature evaluated at planes right before/after the respective tube rows. See fig. 4.8 for a representation of the planes. $T_w = 300K$ is the constant temperature of the tube walls.

The overall heat transfer coefficient is then calculated:

$$U = \frac{\dot{Q}_{tot}}{A_{tot} \Delta T_{LMTD}} \quad (4.4)$$

Here A_{tot} is the total external heat transfer surface area of the finned-tubes.

In the numerical model, the tube walls are modeled as thin walls. This means that

conduction through the tube walls are neglected. The effective/apparent gas-side heat transfer coefficient is simplified to

$$\alpha_e = \frac{1}{\frac{1}{U} - A_{tot} \frac{\ln\left(\frac{d_o}{d_i}\right)}{2\pi L \lambda_f}} \approx U \quad (4.5)$$

Here L is the total length of tube.

In order to calculate the actual average gas-side heat transfer coefficient, α_o , the fin efficiency η is needed. Based on the standard definition of fin efficiency, the fin efficiency can be calculated directly, assuming a constant mean bulk temperature at each tube row.

$$\eta_{sim} = \frac{\dot{Q}_{actual}}{\dot{Q}_{ideal}} = \frac{\int_{fin} (T_s - T_\infty) dA}{A_{fin}(T_{base} - T_\infty)} \approx \frac{\int_{fin} T_s dA - T_\infty A_{fin}}{A_{fin}(T_{base} - T_\infty)} \quad (4.6)$$

Here T_s is the surface temperature on the fin. T_∞ is the mean bulk temperature at each tube row, and is taken to be $\frac{T_{row,in} + T_{row,out}}{2}$. It should be noted that this assumption might give slightly wrong results since the mean gas temperature varies within each row. The assumption is however consistent with the method used by Cleirigh and Smith [6].

The theoretical fin efficiency is also calculated using eq. 2.11 for the solid fins and the theoretical fin efficiency found by Hashizume et al. [9] for the serrated fins. In these calculations, α_e is used from the simulations to calculate the fin parameter m . An iterative procedure is performed in Excel in order to obtain α_o and η_{th} since the two parameters are dependent on each other.

Having calculated the theoretical fin efficiency, the fin efficiency correction using the method proposed by Weierman [25] can be found. The actual heat transfer coefficients from the experimental tests is calculated using this method [11]. It therefore makes sense to calculate the actual heat transfer coefficients from the simulations based on this fin efficiency. The corrected fin efficiency proposed by Hashizume et al. [9] is also calculated. It should be noted that the fin diameter ratio $\frac{d_f}{d_o}$ for geometry 1 equals 2.45 which exceeds the applicable range defined by Hashizume et al. [9]. For completeness the corrected fin efficiency is included anyway. For all the calculated fin efficiencies the overall fin efficiency of the finned tube bundle is taken to be the averaged fin efficiency from the eight tube rows.

The actual average gas-side heat transfer coefficient is defined as

$$\alpha_o = \frac{\alpha_e A_{tot}}{A_{bare} + \eta_{c,W} A_f} \quad (4.7)$$

The Nusselt number can then be calculated

$$Nu = \frac{\alpha_o d_o}{\lambda_{air}} \quad (4.8)$$

4.6.4 Pressure loss

The total pressure loss $\Delta P = P_{in} - P_{out}$ is obtained using the *massFlowAve* function in CFD-Post at the inlet and outlet of the tube bundle. The relevant parameter is the Total Pressure, which includes both frictional pressure loss and pressure change due to acceleration/deceleration. The Euler number can then be calculated.

$$Eu = \frac{2\Delta P \cdot \rho_{air}}{N_L \cdot (\dot{m}''_{air})^2} \quad (4.9)$$

4.7 Mesh sensitivity study for geometry 1

An important goal when performing a CFD study is to minimize the numerical errors of the solution. First of all it is a requirement that the solution is independent of the mesh resolution. A good way to ensure this is to perform a mesh sensitivity study. The main principle behind this study is to keep refining the grid until changes in the solution are negligible. To reduce the simulation time, the smallest mesh that gives a mesh independent solution should be used. In this study, two characteristic numbers of the flow are used to compare the changes in the solution, namely the Nusselt and Euler number. The numbers are obtained by looking at the overall system. Because of a limited time frame of this project, a mesh sensitivity study is done just for geometry 1. An attempt is then made to make similar meshes for the two other geometries, based on the decided mesh for geometry 1.

4.7.1 The tested meshes

	# Nodes	# Prisms	Volume element size	Surface element size
<i>Case 1</i>	211600	0	1.04 units	0.52 units
<i>Case 2</i>	436758	6	1.20 units	0.60 units
<i>Case 3</i>	736725	12	1.20 units	0.6 units
<i>Case 4</i>	1692818	12	0.80 units	0.40 units
<i>Case 5</i>	1694663	6	1.20 units	0.30 units

Table 4.3: The tested meshes for the mesh sensitivity study

See tab. 4.3 for the layout of the tested meshes. Case 5 is considered to be the benchmark. Each mesh is tested for three different Reynolds numbers (5000, 10000 and 25000).

The smallest mesh consisting of 0.21 million nodes has no prisms to resolve the near-wall effects. For the other meshes, prism layers are used. The only difference between case 2 and case 3 is that 6 additional prism layers are added. For case 4 the volume element size and surface element size is made smaller. In case 5 the surface elements are made even smaller and 6 prism layers are applied.

The boundary conditions are set as described in section 4.3. Due to human error the pressure at the outlet was mistakenly set to twice the atmospheric pressure for all simulations in the mesh sensitivity study. It was considered that this mistake would not impact the mesh sensitivity study itself. New simulations were of course ran with the correct pressure for the decided mesh.

Chapter 5

Results and Discussion

Firstly in this chapter the results from the mesh sensitivity study will be presented. It is crucial to ensure that the numerical solution is independent of the mesh resolution. In the rest of the chapter the main focus will be to compare heat transfer and pressure loss in the tube bundle from the simulations to the available experimental data. Both the numerical and experimental data will be compared to well-known semi-empirical correlations from the literature. The effects of uneven heat distribution will be investigated by comparing the simulated and experimental fin efficiencies to corrected efficiencies from the literature. Visualizations of the flow will then be presented in order to explain the characteristic effects happening in the finned tube bundle.

5.1 Results from the mesh sensitivity study

As can be seen in fig. 5.1 and 5.2 the 0.21 million-node mesh deviates considerably from the more refined meshes. The most likely explanation to this is the insufficient mesh resolution within the boundary-layer. This results in a higher predicted Nusselt number and a lower predicted Euler number. This observation is consistent with the findings of Cleirigh and Smith [6].

As can be seen on fig. 5.1 a considerable higher Nusselt number is observed for case 3 compared to the benchmark mesh for $Re = 25000$. One possible explanation to this deviation could be the aspect ratio for the elements closest to the wall. Because of the extra prism layers added, the cells closest to the walls gets stretched out, resulting in bad aspect ratios. Bad aspect ratios for a mesh can result in interpolation errors of unacceptable magnitude. In Ansys ICEM The aspect ratios are scaled, so that an aspect ratio of 1 corresponds to a perfectly regular element, while an aspect ratio of 0 indicates that the element has zero area/volume [1]. Investigations showed that for case 2, 0.25% of the elements had a aspect ratio lower than 0.1. For case 3 0.96% of the elements had a aspect ratio lower than 0.1.

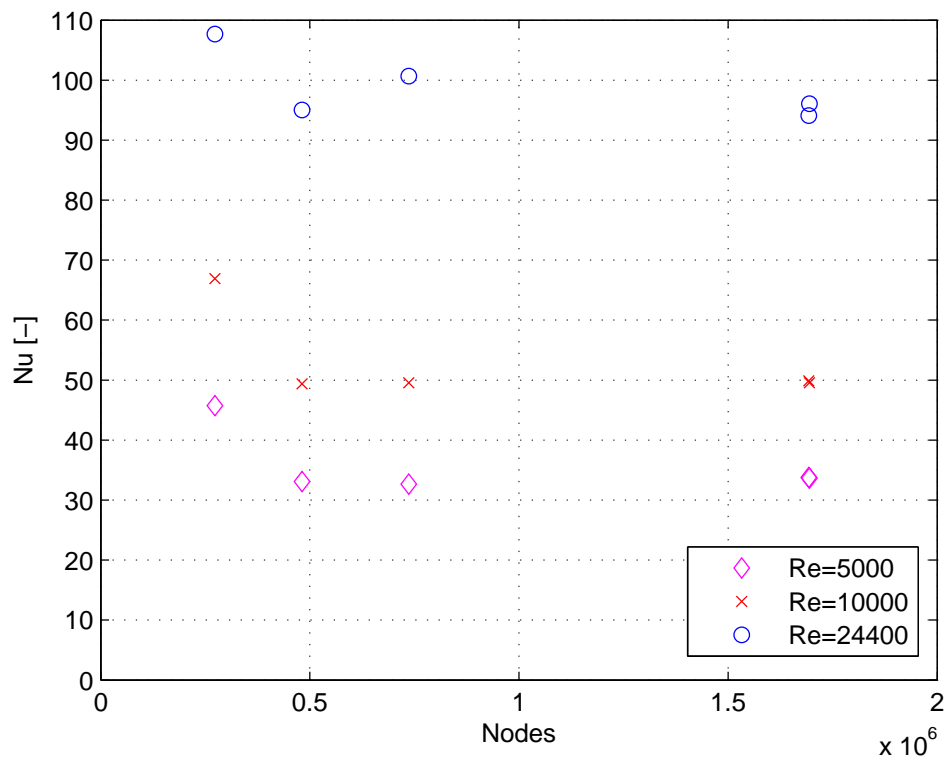


Figure 5.1: Nusselt number versus number of nodes for three different Reynolds numbers.

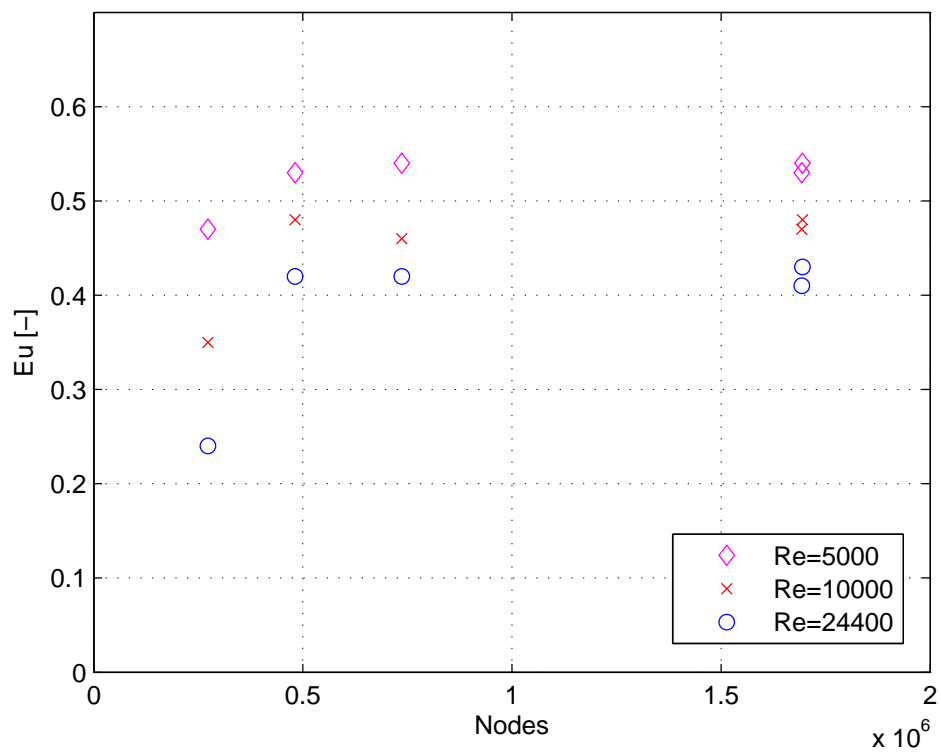


Figure 5.2: Euler number versus number of nodes for three different Reynolds numbers.

Re [-]	Case 1	Case 2	Case 3	Case 4
5000	35.88%	-1.66%	-2.98%	0.33%
10000	35.24%	-0.16%	0.17%	0.80%
25000	12.09%	1.08%	4.76%	-2.07%

Table 5.1: Deviations in Nusselt number from the benchmark mesh, $\frac{Nu_{case} - Nu_{bench}}{Nu_{bench}} \cdot 100\%$

Re [-]	Case 1	Case 2	Case 3	Case 4
5000	-13.06%	-1.91%	0.29%	-1.75%
10000	-26.34%	0.00%	-4.61%	-0.55%
25000	-44.45%	-2.43%	-3.39%	-4.66%

Table 5.2: Deviations in Euler number from the benchmark mesh, $\frac{Eu_{case} - Eu_{bench}}{Eu_{bench}} \cdot 100\%$

Therefore for the final cases, it was decided to have one case with 6 prism layers and one case with 12 prism layers. For case 5 with 6 prism layers the focus was to improve the aspect ratios by making the surface elements smaller. After looking at the results it is seen that case 5 predicts a higher Euler number than case 4. Since the simulations generally under-predicts the Euler number compared to experimental data, it is decided to use case 5 in the further calculations. Six prism layers near the walls are therefore considered to be enough to resolve the near-wall effects.

Fig. 5.3 shows the y^+ values at the fin walls for the decided mesh (case 5). As discussed in section 3.2, $y^+ \approx 1$ is required in order for the viscosity-affected region to be resolved adequately. As can be seen from the figure this holds for a case with low Reynolds number. For the case with a high Reynolds number $y^+ > 1$. Since the SST $k - \omega$ turbulence model uses Enhanced Wall Treatment (EWT) the numerical model should still be able to provide decent results.

It should be noted that it was considered to further refine the mesh. When this was tried the the computer used lacked the necessary memory. For further work a more refined grid should be tested in order to verify that case 5 provides a good enough result.

Similar meshes are made for geometry 2 and 3 based on the conclusions drawn from the sensitivity analysis. As mentioned earlier, prism layers are not created for geometry 3.

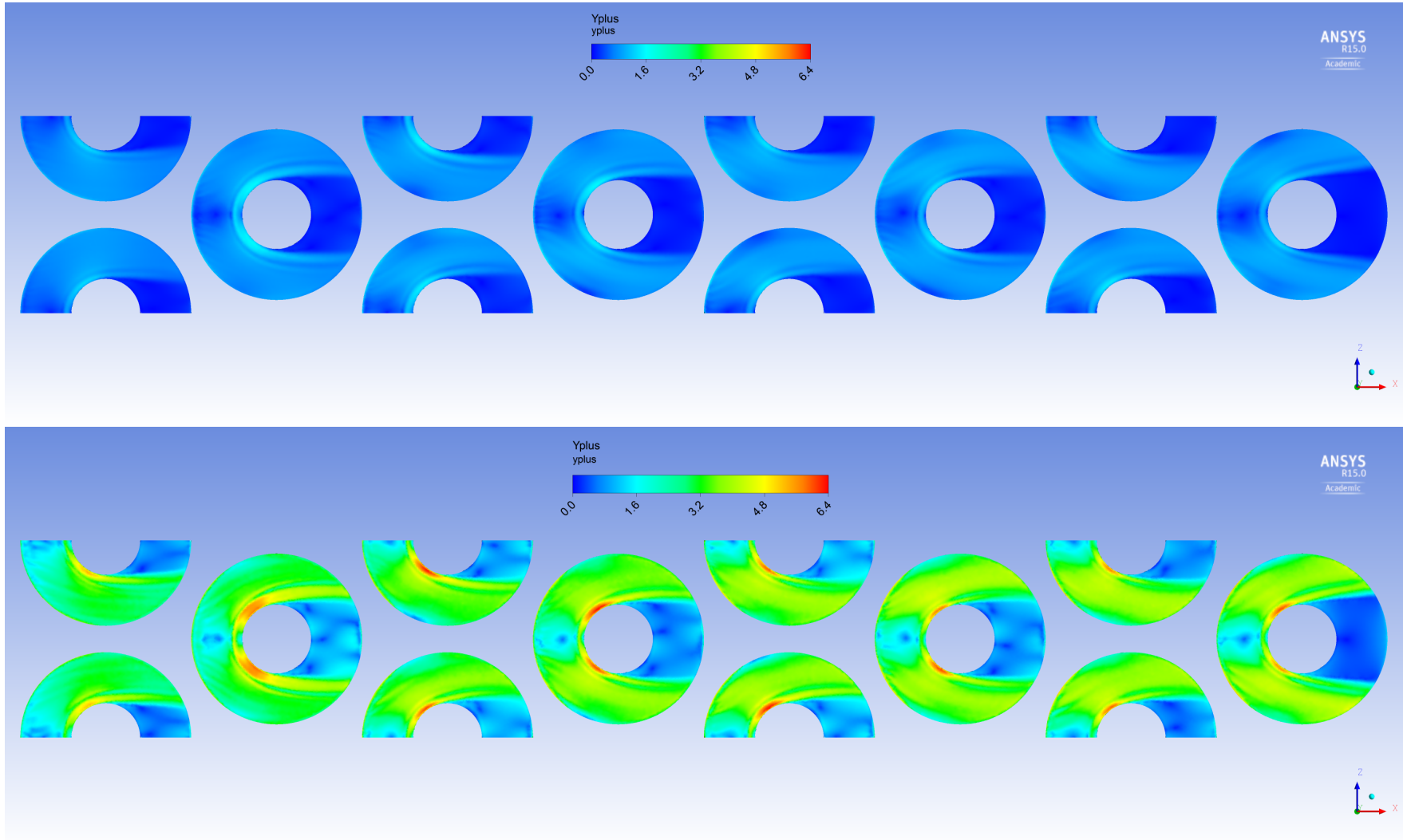


Figure 5.3: y^+ values for the decided mesh (for geometry 1) at $Re = 4397$ (top) and $Re = 26086$ (bottom)

5.2 Geometry 1 (solid fins)

5.2.1 Nusselt number

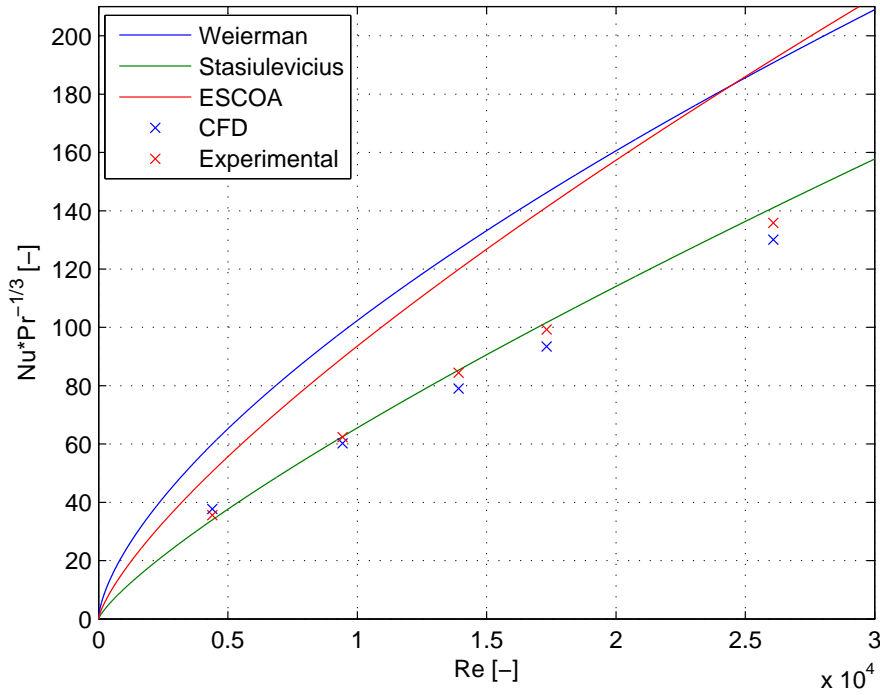
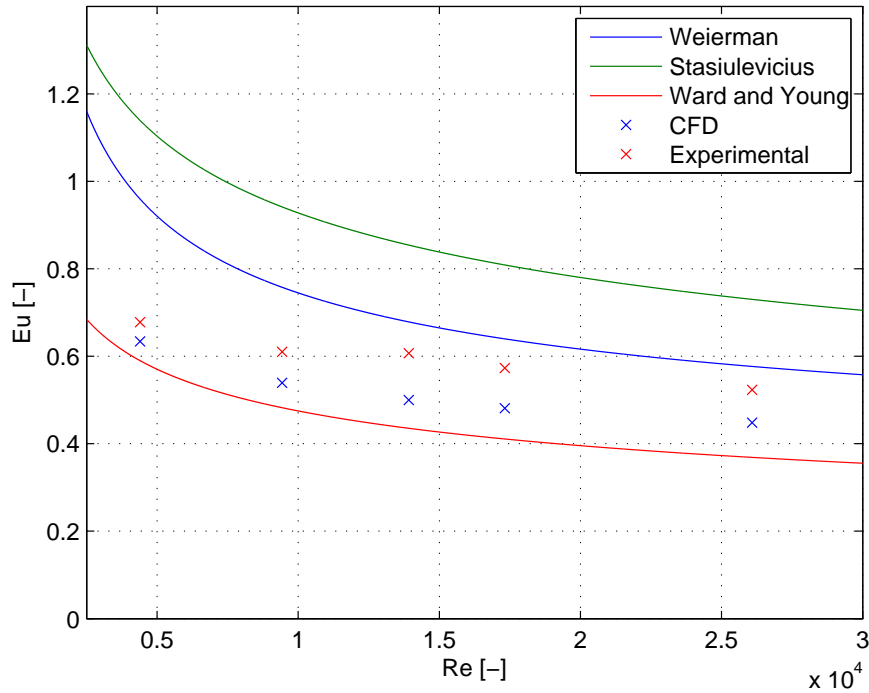


Figure 5.4: $Nu \cdot Pr^{-\frac{1}{3}}$ vs. Re for geometry 1

The Nusselt number is based on the actual heat transfer coefficient obtained using the fin efficiency according to Weierman [25]. The Nusselt number is calculated at each row and then averaged to give a Nusselt number for the entire tube bundle. Fig. 5.4 compares the numerical case to the experimental case, as well as three semi-empirical correlations for heat transfer in finned tube bundles. See appendix B for the equations used. Here the Prandtl number is taken to be constant $Pr = 0.7$. As can be seen from the figure, the numerical result seems to under-predict the experimental result and the correlations. The correlations from Stasiulevicius et al. [21] seems to be the best fit for both the numerical and experimental result. The numerical result exhibits a similar sensitivity to the Reynolds number as the correlations and experimental data. Also for higher Reynolds numbers where the flow is highly turbulent, the numerical model is able to provide decent results. This strengthens the use of the SST $k - \omega$ turbulence model.

5.2.2 Euler number

Fig 5.5 compares the numerical case to the experimental case, as well as three semi-empirical correlations for pressure drop. As can be seen the numerical results tend to

Figure 5.5: Eu vs. Re for geometry 1

undershoot the experimental values. It is believed that a major reason for the deviation between the numerical and experimental result is the fact that for the experimental finned tubes the fins are twisted helically around the tube. In the numerical model the fins are circular around the tubes. For the helical fins an additional drag effect on the fins is expected to cause an increase in pressure drop.

Also for the pressure drop the numerical result exhibits a similar sensitivity to the Reynolds number as the correlations, which is a good sign. Large variations can be seen between the correlations. This indicates that predicting the pressure loss in a finned tube bundle is a complicated and difficult procedure.

5.2.3 Heat transfer

Fig. 5.6 shows the actual heat transfer coefficient α_o for four different Reynolds numbers, including both simulated and experimental values at each tube row. Since the simulated Reynolds numbers did not exactly match the experimental Reynolds numbers, the experimental heat transfer coefficients are interpolated between two nearby experimental tests in order to match the simulated case. This is also done for geometry 2 and 3. First of all it can be seen from fig. 5.6 that the simulation generally under-predicts the experimental heat transfer coefficient. However the numerical model seems to predict the first and last row fairly well for the whole range of Reynolds numbers. A clear tendency for both the

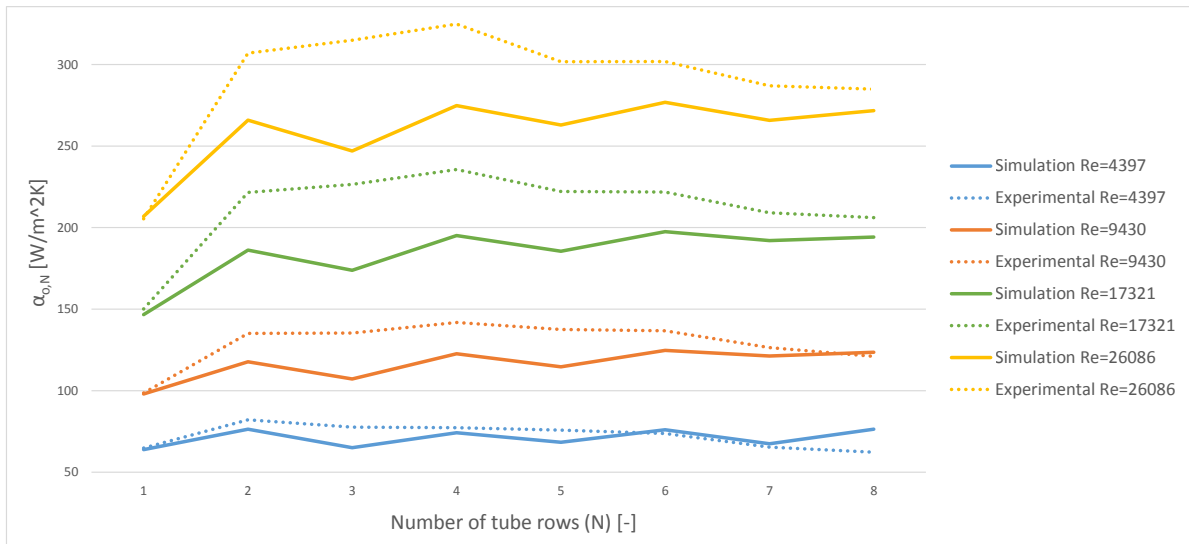


Figure 5.6: Comparison of the heat transfer coefficients for geometry 1 with four varying Reynolds number

numerical and experimental heat transfer coefficients is that the heat transfer drastically increases from row 1 to row 2. This phenomena is also generally observed in the relevant literature. According to Sparrow and Samie [19], which investigated staggered finned tube arrangements for different Reynolds numbers and tube pitches, the most likely explanation to this phenomena is the higher turbulence and velocity provided by the jet stream of the preceding row (row 1).

Fig. 5.7 plots the deviations in simulated values to the experimental ones. As can be seen from the figure, the case with $Re = 4397$ predicts better the experimental data than the other three cases with higher Reynolds number. A tendency for the simulations is that the first row has small deviations on heat transfer. With increasing row number the deviation increases. A possible reason for this could be that the flow becomes more complex to model because of the row to row effects like flow separation after the rows for example.

An interesting topic to investigate is the stabilization of the heat transfer coefficient in the finned tube bundle. Fig. 5.8 shows the ratio between the heat transfer coefficient for each single row and the average value found for row 4-8. According to a literature study performed by Klynderud [13], it can be generally be observed that the heat transfer coefficient seems to stabilize around the fourth row and only have a minor increase towards the eight and final row. Based on fig. 5.8 this tendency can be seen for the numerical case at a high Reynolds number. Also for the experimental case the heat transfer coefficient stabilizes after the fourth row, but unlike the simulation, the value decreases towards the final row. At a low Reynolds number however, no clear tendency can be seen. There is

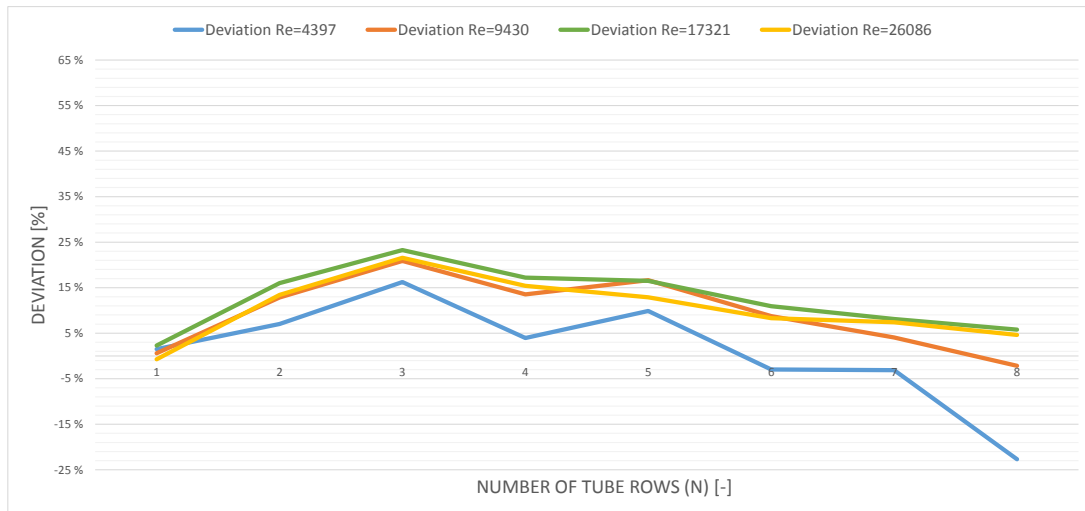


Figure 5.7: Relative Deviation between simulated and experimental heat transfer coefficient for geometry 1, $\frac{\alpha_{o,exp} - \alpha_{o,sim}}{\alpha_{o,exp}} \cdot 100\%$

no good explanation to why the heat transfer coefficient increases and decreases from row to row.

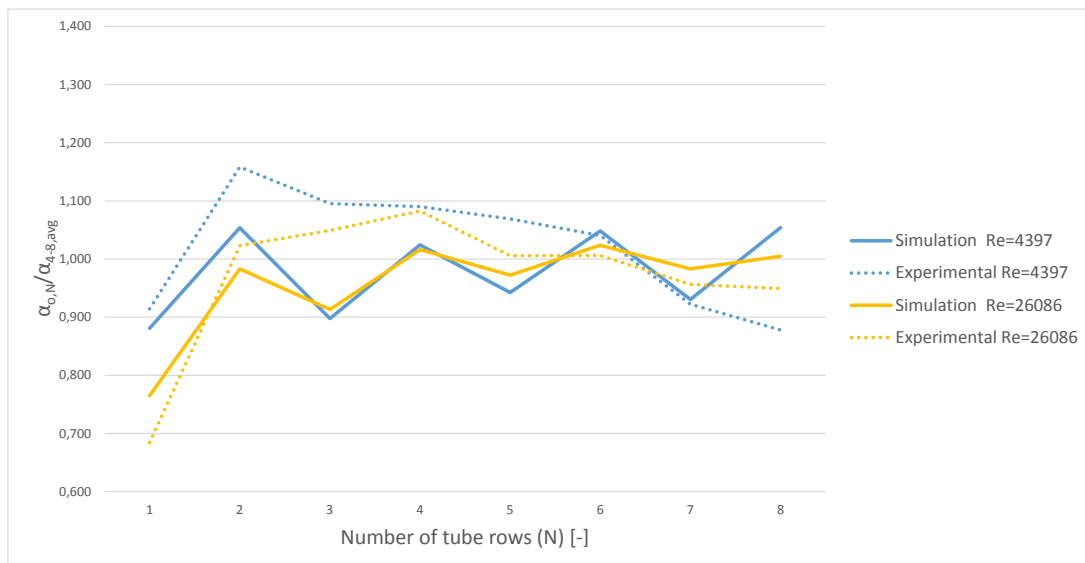
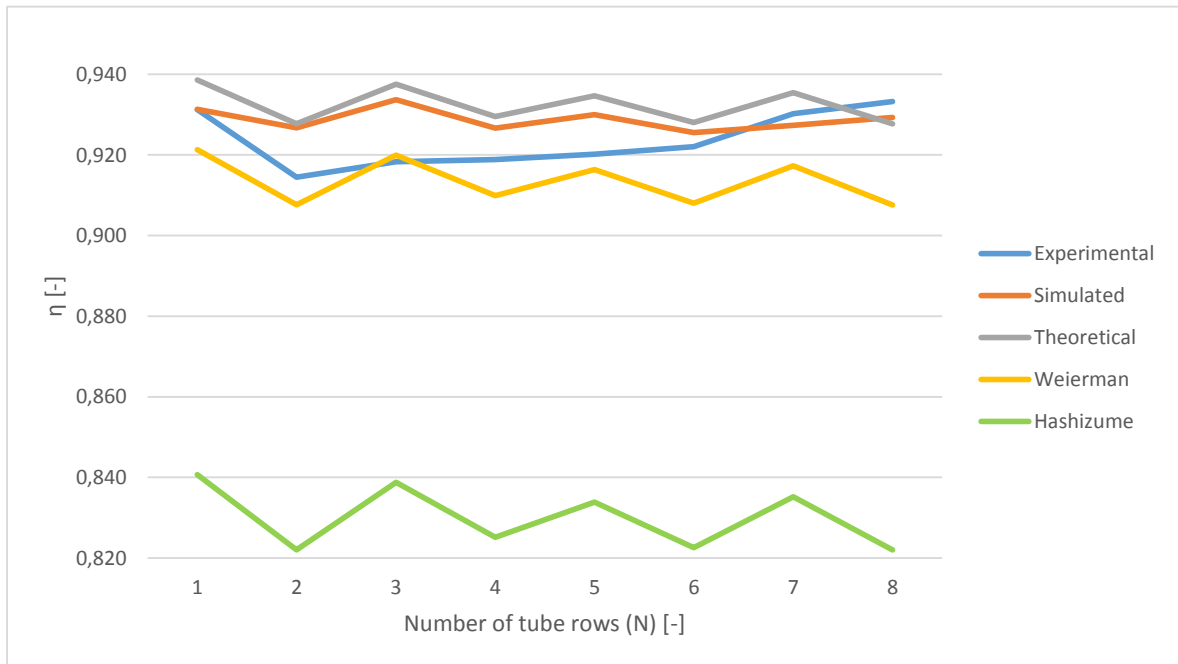


Figure 5.8: Ratio between row heat transfer coefficient to the average heat transfer coefficient for row 4-8 (geometry 1)

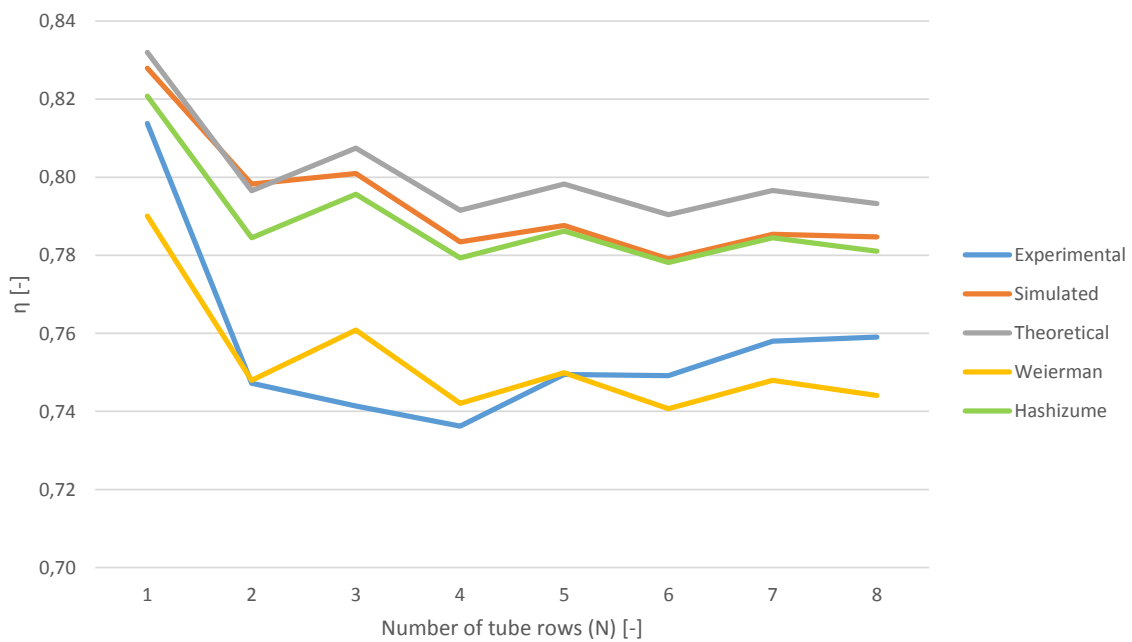
5.2.4 Fin efficiencies

As can be seen from fig. 5.9, the fin efficiency found from the simulations lies closest to the theoretical fin efficiencies. It can also be seen that Weierman [25] better predicts the fin efficiency at a low Reynolds number. The opposite is the case for the fin efficiency

calculated from Hashizume et al. [9]. The most likely reason to why [9] deviates considerably for low Reynolds number is that the case is outside the defined applicable region. Keep in mind that the theoretical fin efficiency and the corrected fin efficiencies calculated from Weierman [25] and Hashizume et al. [9] uses the effective heat transfer coefficient, α_e calculated from the simulations using eq. 4.5.



(a) $Re = 4397$



(b) $Re = 26086$

Figure 5.9: Fin efficiencies for geometry 1

5.3 Geometry 2 (solid fins)

5.3.1 Nusselt number

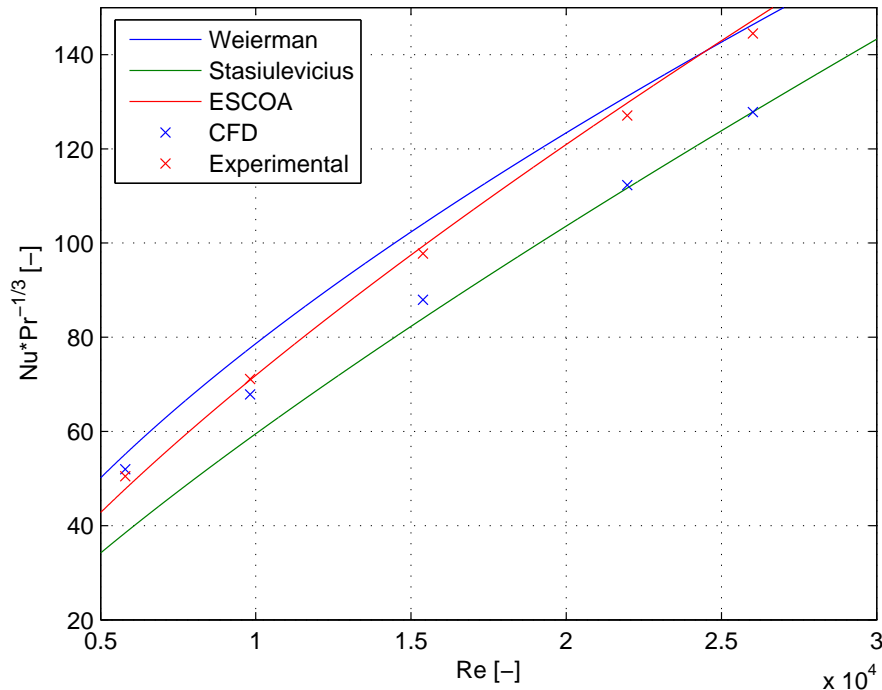
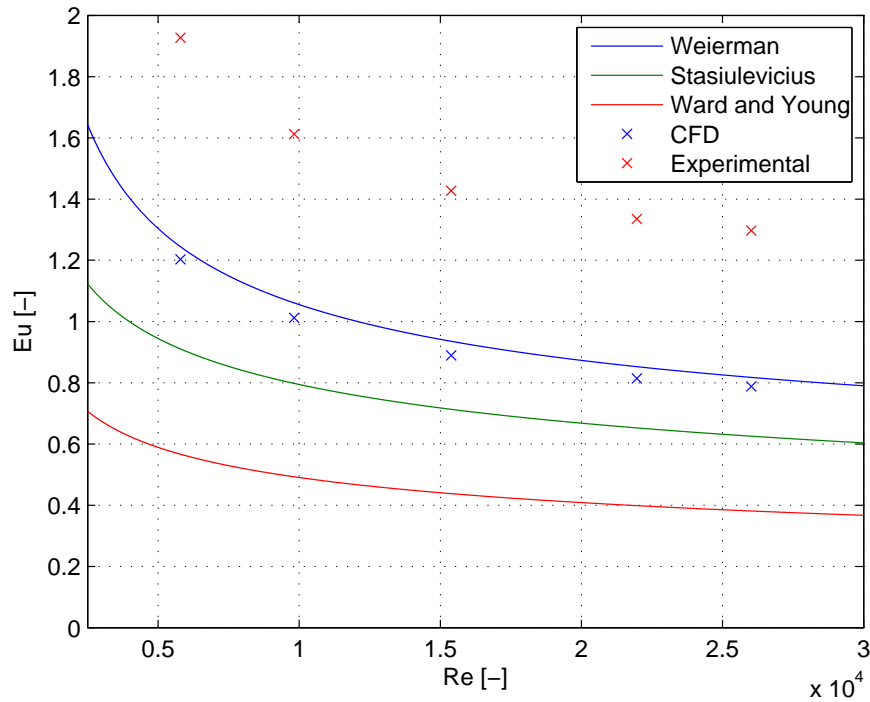


Figure 5.10: $Nu \cdot Pr^{-\frac{1}{3}}$ vs. Re for geometry 2

Fig. 5.10 compares the numerical case to the experimental case, as well as three semi-empirical correlations for heat transfer in finned tube bundles. When compared to geometry 1 (fig. 5.4), larger deviations are seen between the numerical and experimental result for geometry 2. The numerical result lies close to Stasiulevicius et al. [21]. The prediction of the Nusselt number worsens with increasing Reynolds number.

5.3.2 Euler number

Fig 5.5 compares the numerical case to the experimental case, as well as three semi-empirical correlations for pressure drop. As can be seen the numerical result under-shoots the experimental result. This is probably due to the same reason as explained for geometry 1 (circular versus helical fins). The numerical result exhibits a similar sensitivity to the Reynolds number as the correlations and the experimental data. As can be seen the numerical result is right in alignment with Weierman [25].

Figure 5.11: Eu vs. Re for geometry 2

5.3.3 Heat transfer

Fig. 5.12 shows the actual heat transfer coefficient α_o for four different Reynolds numbers, including both simulated and experimental values at each tube row. Similarly to geometry 1, the numerical model tends to under-predict the experimental data. The experimental heat transfer coefficient at tube row eight for $Re = 5793$ is believed to be an outlier caused by experimental error and should be neglected.

When comparing fig. 5.13 with fig. 5.7 it can be seen that the deviation between simulated and experimental data is larger for geometry 2 than for geometry 1. The longitudinal and transversal pitch relative to the finned tube size is smaller for geometry 2 than for geometry 1. In other words, geometry 2 is a narrow and densely packed finned tube bundle and therefore a more challenging task to model numerically. This is probably one of the reasons as to why larger deviations are seen for geometry 2.

Fig. 5.14 shows that for the case with a high Reynolds number the heat transfer coefficients stabilize after the fourth row for both the numerical and experimental data. For the case with the low Reynolds number the experimental data follows a pattern where the heat transfer coefficient oscillates up and down. This is not the case for the numerical data. A possible reason can be that the flow effects happening in the tube bundle behave differently for the numerical and experimental setup. In such a densely packed tube

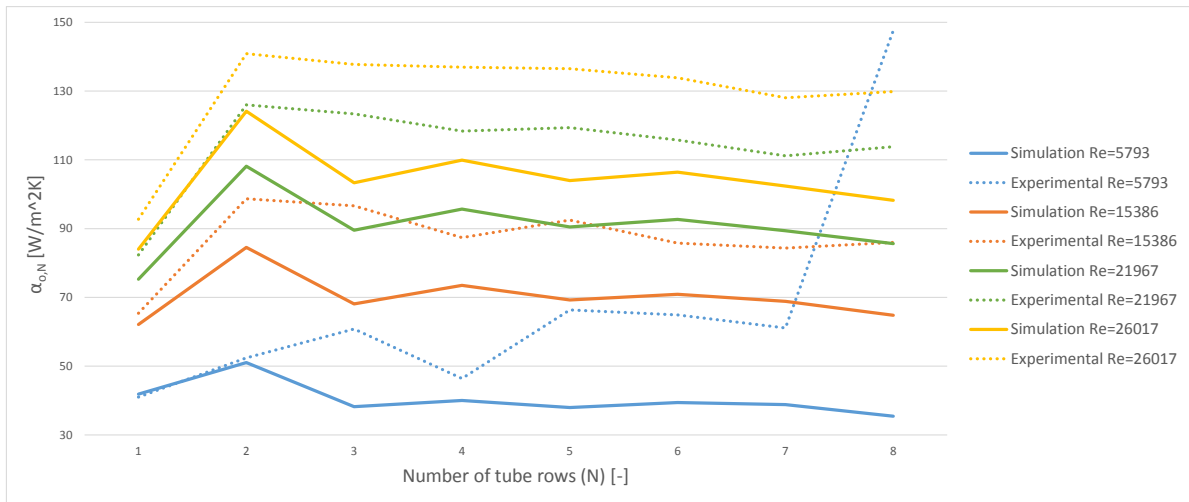


Figure 5.12: Comparison of the heat transfer coefficients for geometry 2 with four varying Reynolds number

bundle there is no guarantee that the numerical model manage to simulate the separation effects happening behind each tube row for example.

5.3.4 Fin efficiencies

Fig. 5.15 shows that the simulated fin efficiency over-predicts the experimental fin efficiency. This is the same tendency as seen for geometry 1. The geometry of the finned tubes for geometry 2 lies within the applicable range defined by Hashizume et al. [9]. As can be seen from the figure the fin efficiency by Hashizume et al. [9] is in better alignment with the simulated fin efficiency for the case with a high Reynolds number. For a low Reynolds number the simulated efficiency lies closest to the theoretical fin efficiency. The numerical model seems to predict the experimental fin efficiency better for a low Reynolds number than for a high Reynolds number. Bear in mind that the experimental fin efficiency is found using the method from Weierman [25]. It therefore makes sense that these two fin efficiencies lay close together.

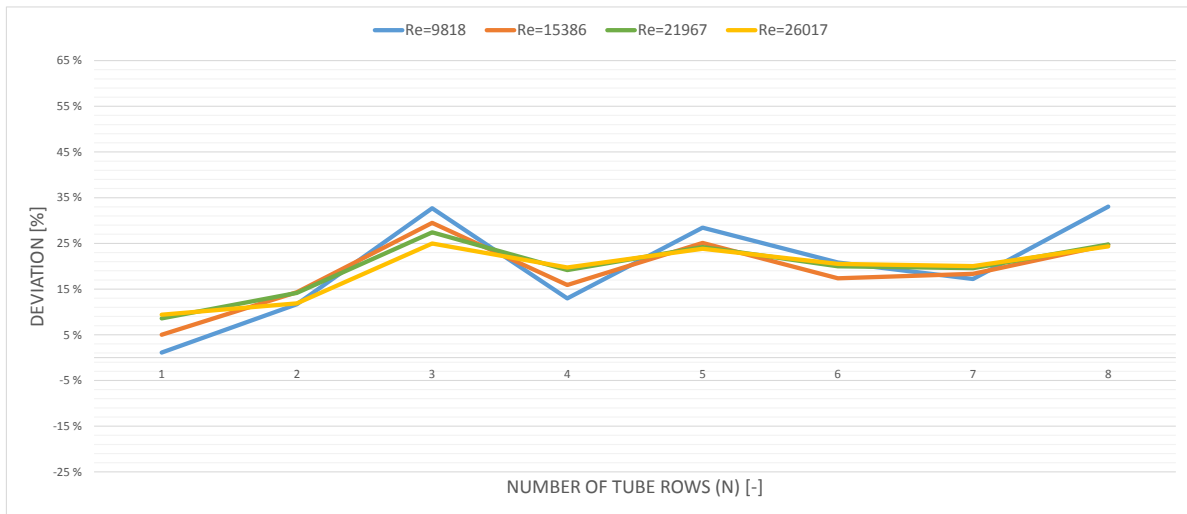


Figure 5.13: Deviation between simulated and experimental heat transfer coefficient for geometry 2, $\frac{\alpha_{o,exp} - \alpha_{o,sim}}{\alpha_{o,exp}} \cdot 100\%$

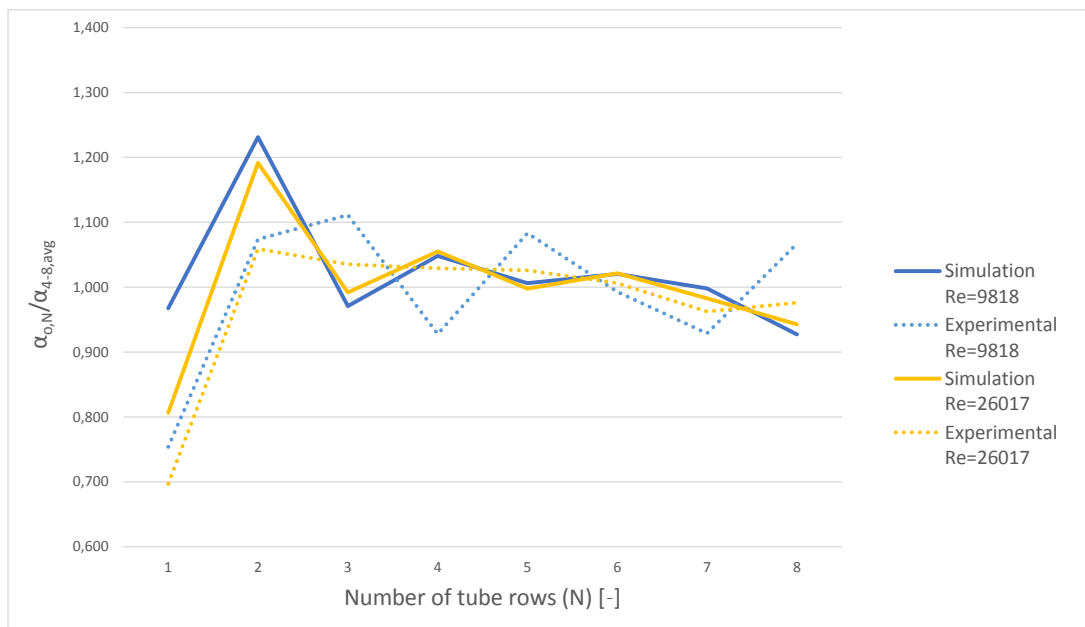


Figure 5.14: Ratio between row heat transfer coefficient to the average heat transfer coefficient for row 4-8 (geometry 2)

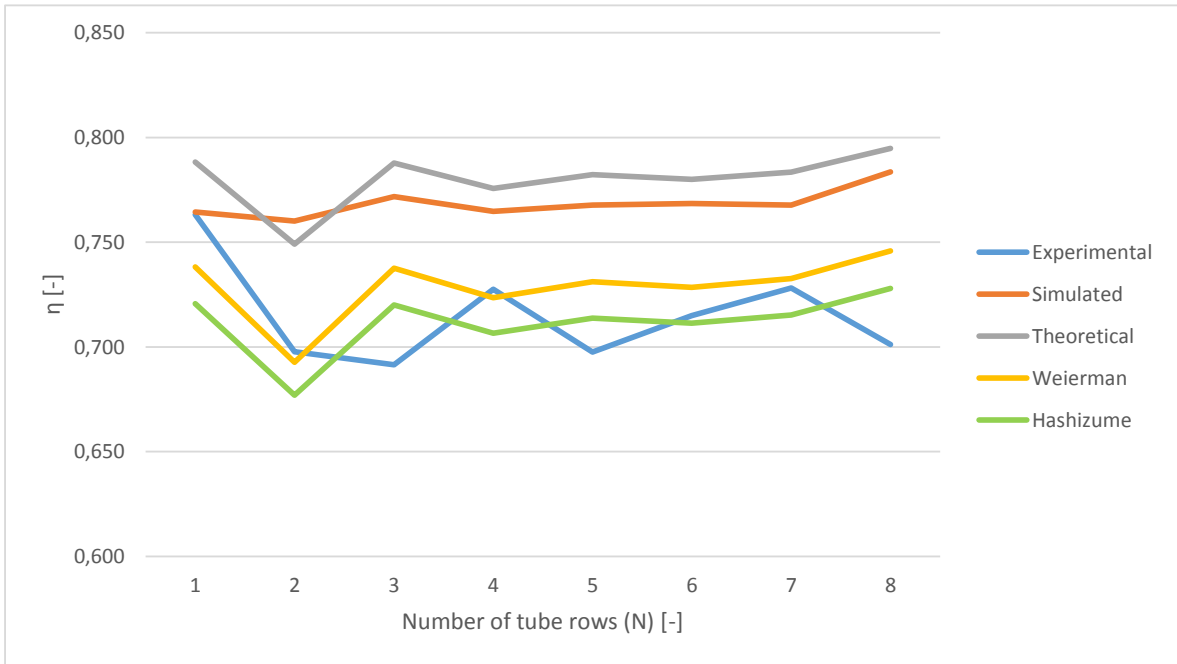
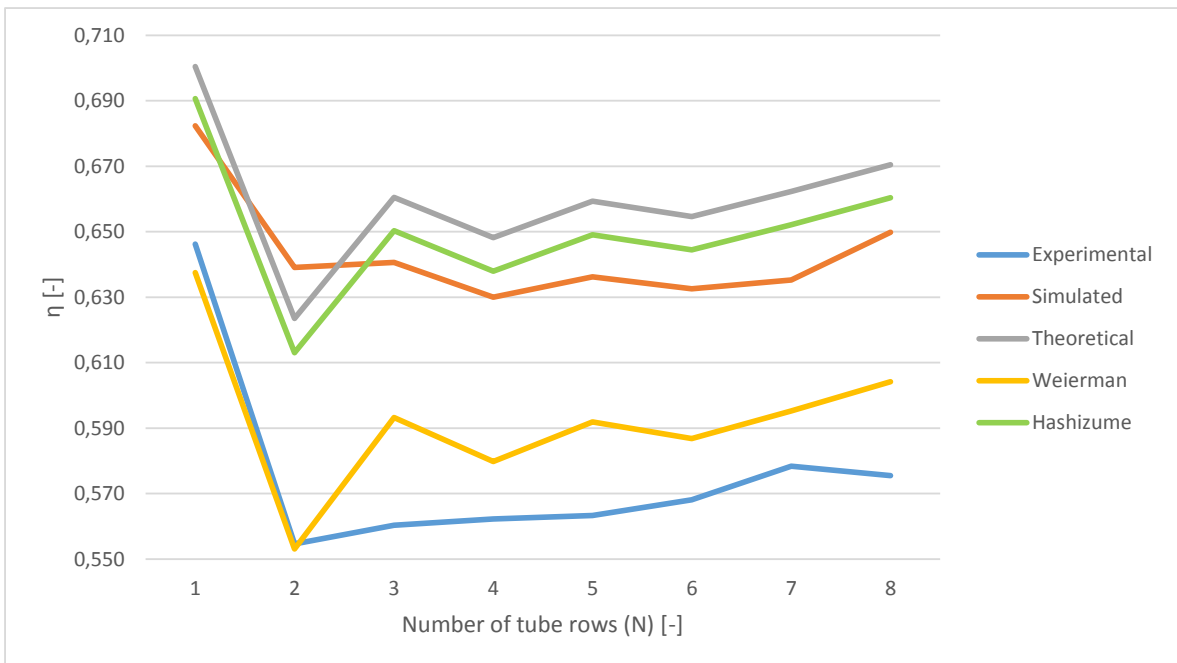
(a) $Re = 9818$ (b) $Re = 26017$

Figure 5.15: Fin efficiencies for geometry 2

5.4 Geometry 3 (serrated fins)

5.4.1 Nusselt number

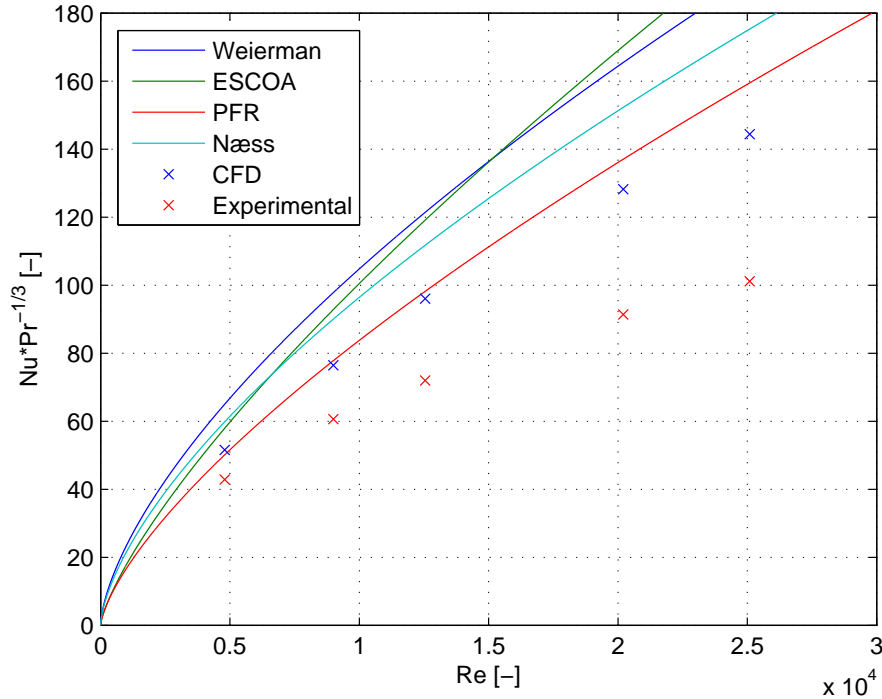


Figure 5.16: $Nu \cdot Pr^{-\frac{1}{3}}$ vs. Re for geometry 3

Fig. 5.16 compares the numerical case to the experimental case, as well as four semi-empirical correlations. Since the geometry consists of serrated fins the correlations are different than from geometry 1 and 2. The figure shows a surprising result. For geometry 1 and 2 the numerical result under-shoots the experimental result. As can be seen from fig. 5.16 the opposite is the case for geometry 3. As mentioned earlier, [6] pointed out that an insufficient mesh resolution within the boundary-layer can result in a higher predicted Nusselt number. Since geometry does not have prism layers close to the walls, this is exactly the case for geometry 3. There might be other unknown numerical issues as well that arise when modeling serrated fins instead of solid fins. Another possible reason could be that the finned tubes used experimentally for geometry 3 have a lower quality of welding than geometry 1 and 2.

Interestingly, the experimental result agrees fairly well with the correlations. This might just be a coincidence, in the future different geometries with serrated fins should be considered. As can be seen from fig. 5.16 the numerical result lies closest to PFR [22]. This is the simplest correlation, only considering Re , Pr and the geometry of the finned tubes, not the layout of them in the bundle. The numerical result exhibits a similar

sensitivity to the Reynolds number as the correlations.

5.4.2 Euler number

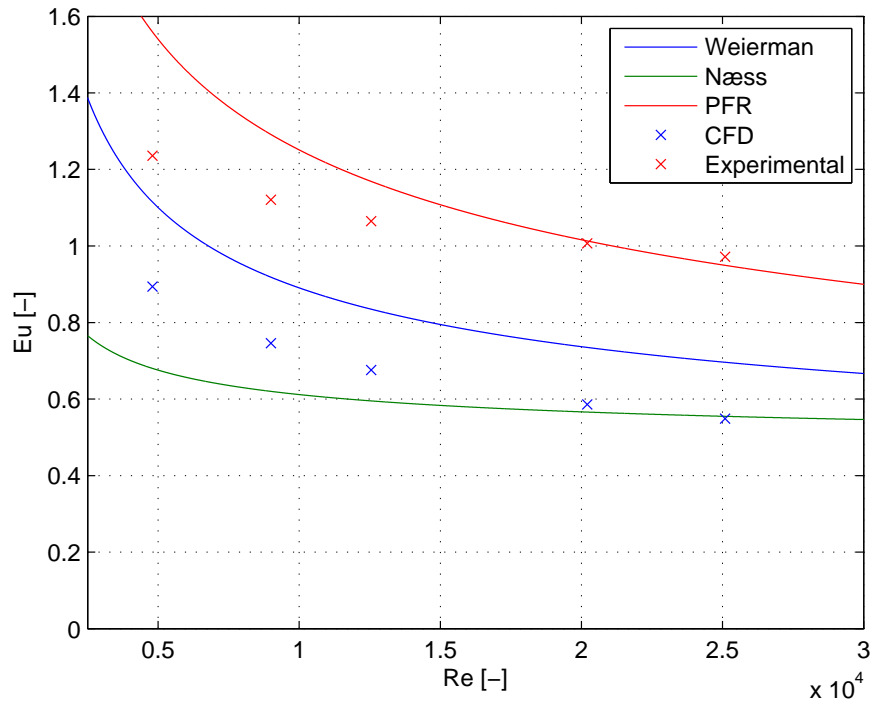


Figure 5.17: Eu vs. Re for geometry 3

Fig. 5.17 shows large deviations between the numerical and experimental Euler number, but the numerical and experimental exhibits a similar sensitivity to the the Reynolds number. Large variations exists between the correlations, which indicates the complexity and difficulty of predicting the Euler number. One of the reasons to the deviation between the experimental and numerical result is most likely due to how the fins are twisted around the tubes (circular versus helically).

5.4.3 Heat transfer

Fig. 5.18 shows that the numerical heat transfer over-predicts the experimental case with increasing Reynolds number. For the case with the lowest Reynolds number the numerical and experimental result are in good agreement.

Fig. 5.19 shows the clear tendency where deviations increase as the Reynolds number increase. This clear tendency can not be seen in fig. 5.7 and 5.13. In other words: Geometry 1 and 2 better predict the heat transfer coefficient for increasing Reynolds numbers than geometry 3 does when compared to experimental data. Geometry 3 does not have prism layers close to the walls. A possible reason could therefore be that the

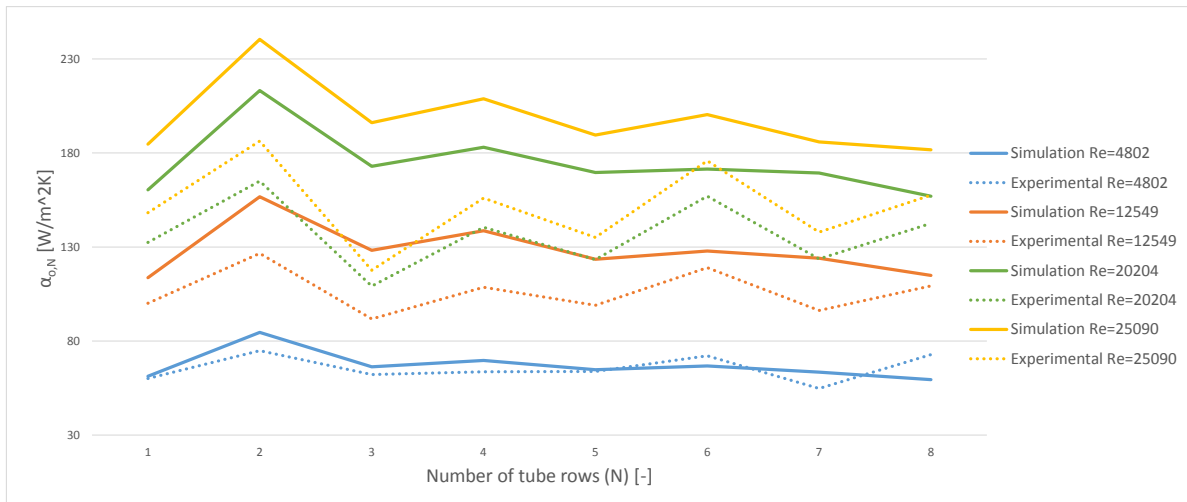


Figure 5.18: Comparison of the heat transfer coefficients for geometry 3 with four varying Reynolds number

numerical model for geometry 3 fails to predict the heat transfer coefficients for highly turbulent flows because of the insufficient mesh resolution close to the walls.

Fig. 5.20 shows that the heat transfer coefficients stabilize after the fourth row for the numerical case. This differs from the experimental case, where oscillating values are seen for the heat transfer coefficients.

5.4.4 Fin efficiencies

Fig. 5.21 shows that the simulated fin efficiencies under-predicts the experimental fin efficiencies. The deviation is largest for the case with a high Reynolds number. In 5.21(b) the experimental fin efficiency is higher than the theoretical fin efficiency. This is unrealistic/not possible and further indicates that the numerical models fails at higher Reynolds numbers. The corrected fin efficiency from Hashizume et al. [9] lies closer to both the simulated and experimental fin efficiencies for a high Reynolds number. This is the same tendency as seen for the two other geometries.

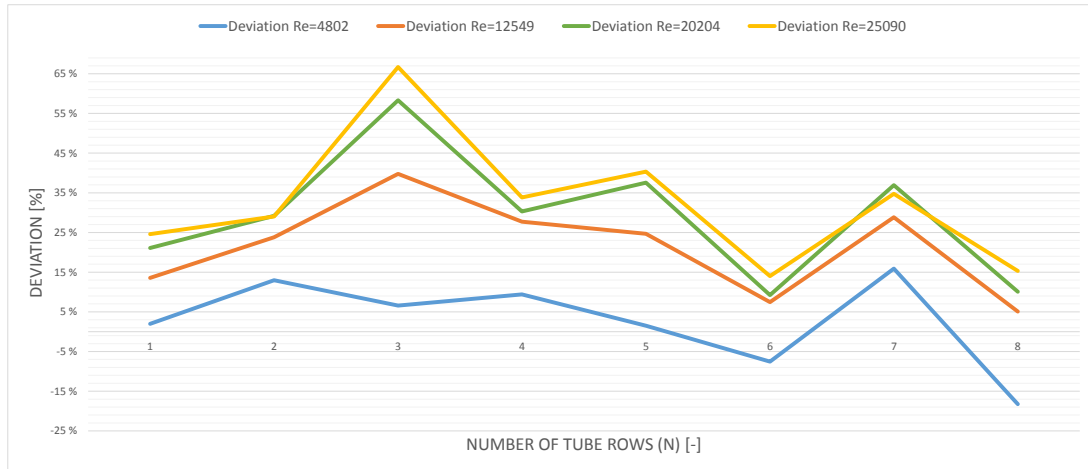


Figure 5.19: Relative Deviation between simulated and experimental heat transfer coefficient for geometry 3, $\frac{\alpha_{o,sim} - \alpha_{o,exp}}{\alpha_{o,exp}} \cdot 100\%$

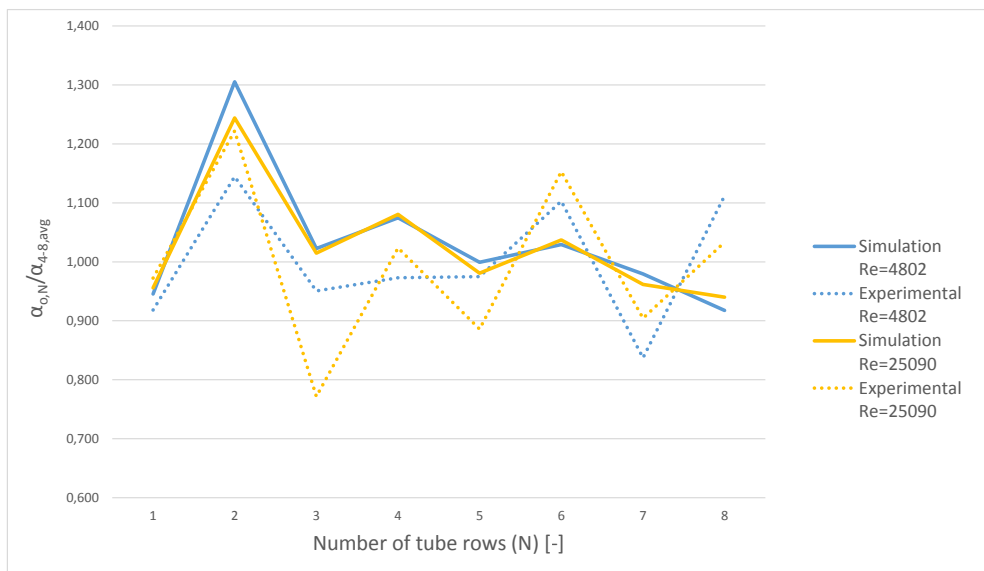


Figure 5.20: Ratio between row heat transfer coefficient to the average heat transfer coefficient for row 4-8 (geometry 3)

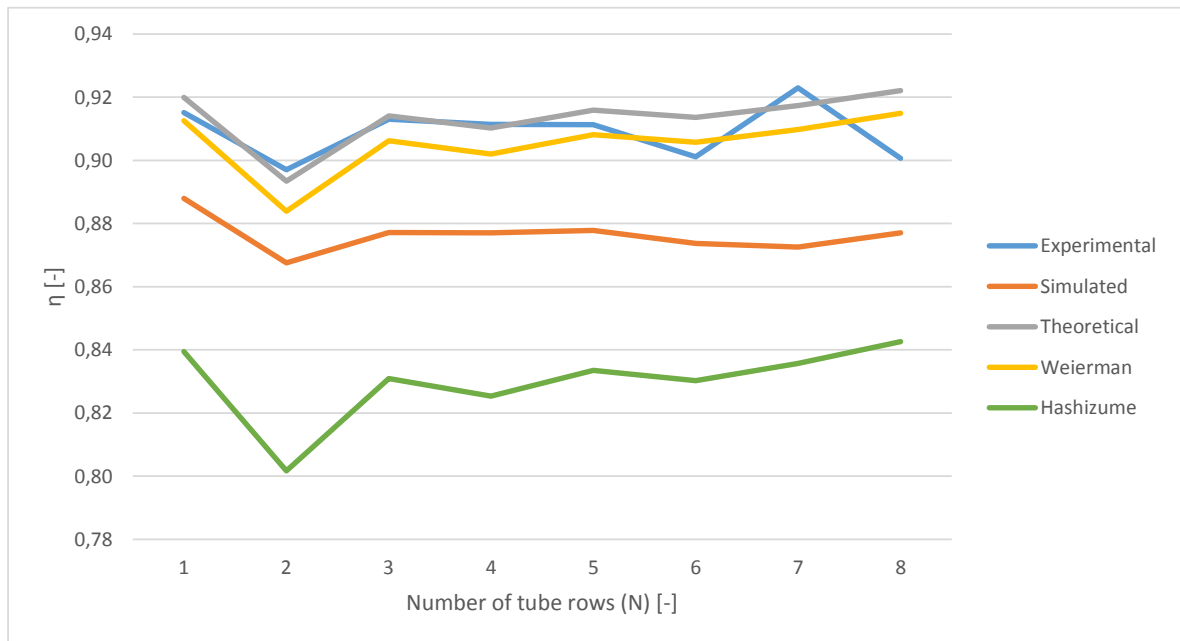
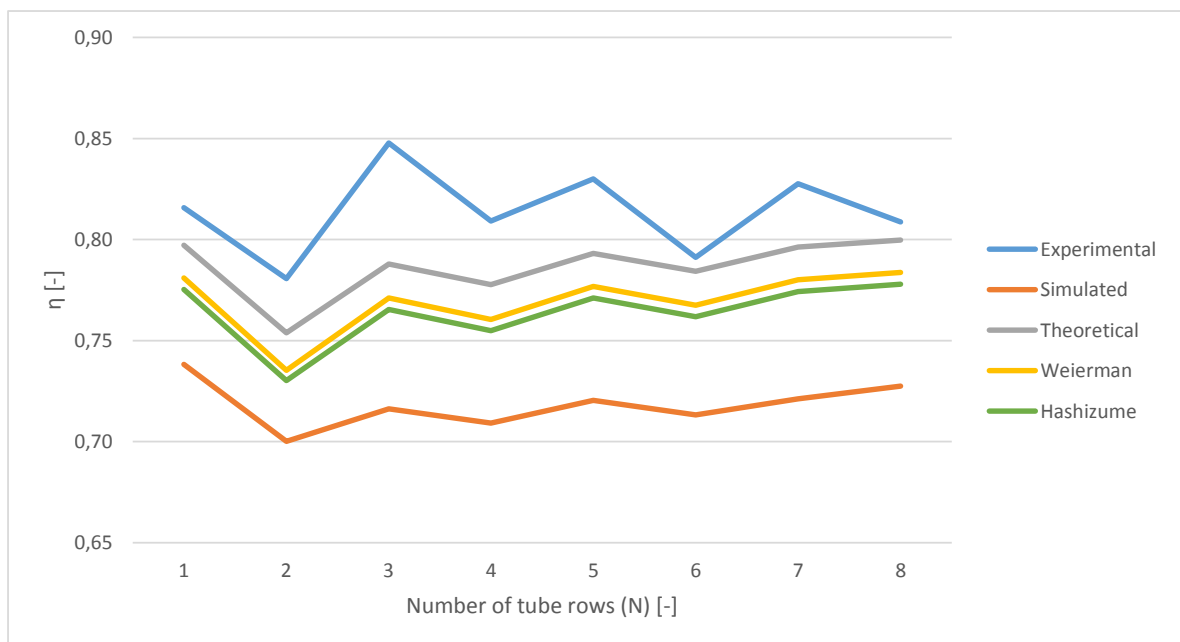
(a) $Re = 4802$ (b) $Re = 25090$

Figure 5.21: Fin efficiencies for geometry 3

5.5 Fin efficiencies at varying thermal conductivities

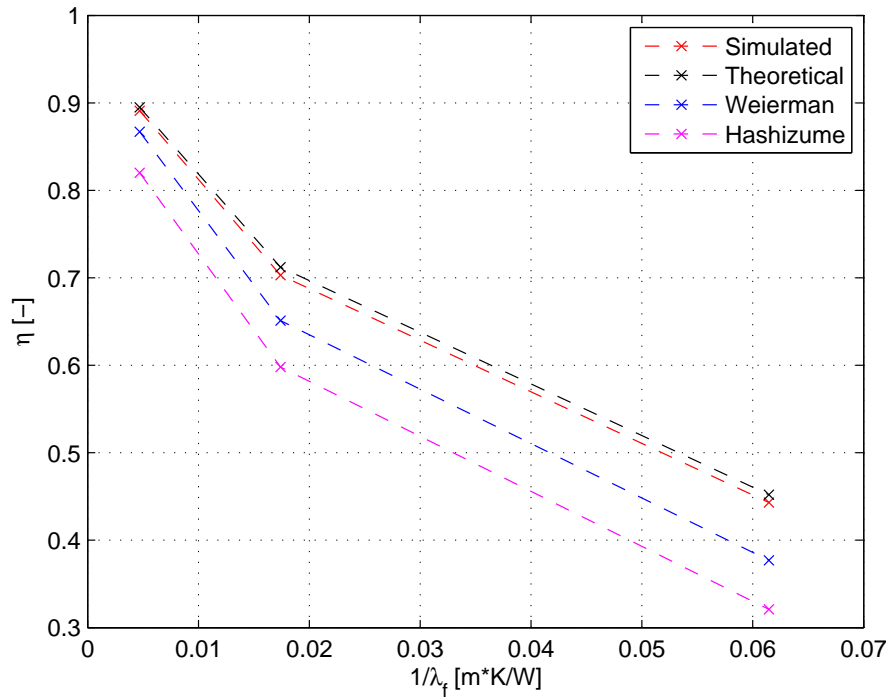
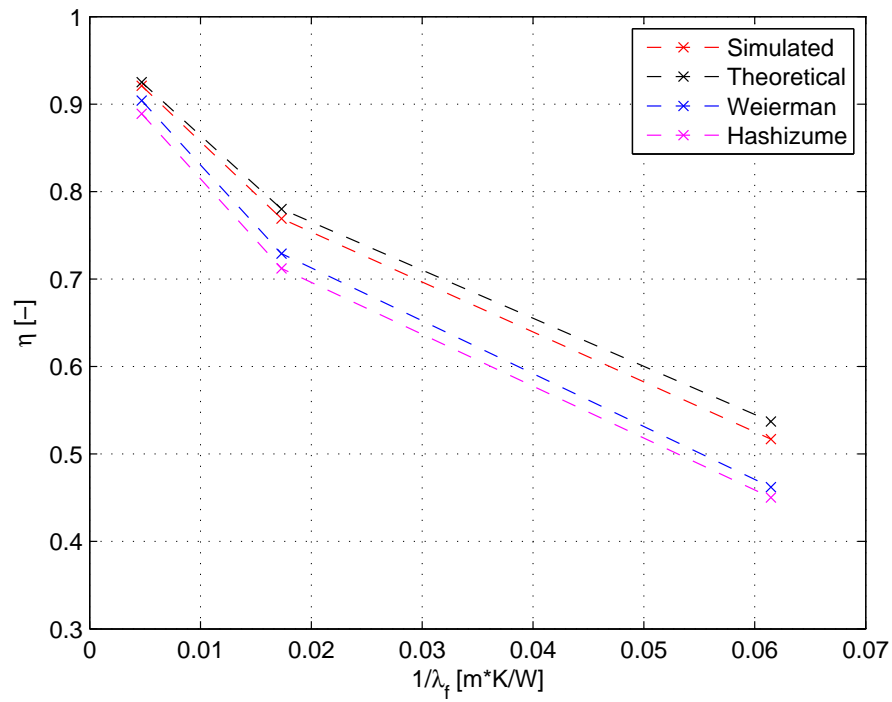
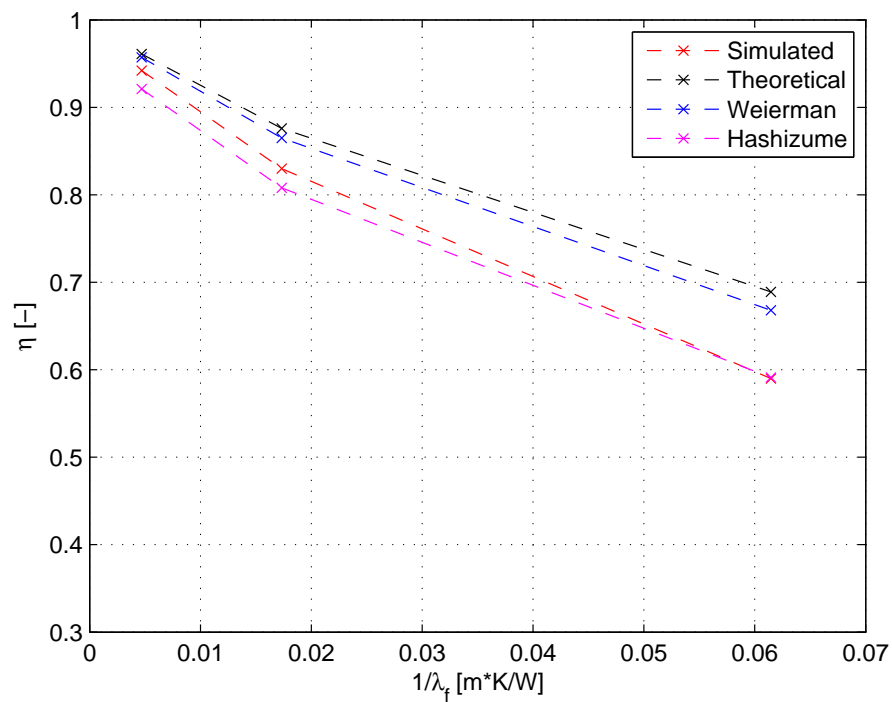


Figure 5.22: $1/\lambda_f$ vs. fin efficiencies η for geometry 1 ($Re = 9430$)

In order to investigate the impact thermal conductivity has on the prediction of fin efficiency, each of the geometries are simulated with three different fin materials for a case with $Re \approx 10000$. The materials considered are Aluminum, Carbon Steel and Steel. For Aluminum and Carbon Steel the thermal conductivities are set with the polynomial function given in appendix A. For Steel a constant thermal conductivity of $k_s = 16.27\text{W}/(\text{m} \cdot \text{K})$ is set. Since the experimental rig only considers one material for each geometry, experimental fin efficiencies are not included.

The results are given in fig. 5.22, 5.23 and 5.24. In the plots Aluminum which has the highest thermal conductivity is to the far left on the x-axis and Steel with the lowest thermal conductivity is to the far right. In the figures it can be seen that as the thermal conductivity decreases, the spread between the simulated and corrected fin efficiencies increases. For geometry 1 and 2 the simulated fin efficiency lies closest to the theoretical fin efficiency. For geometry 3 with serrated fins the corrected fin efficiency from Hashizume et al. [9] is the best fit.

Figure 5.23: $1/\lambda_f$ vs. fin efficiencies η for geometry 2 ($Re = 9818$)Figure 5.24: $1/\lambda_f$ vs. fin efficiencies η for geometry 3 ($Re = 9000$)

5.6 Qualitative analysis of the finned tube bundles

This section focus on qualitatively describing the different local fluid flows and heat transfer phenomenas happening in the finned tube bundles. While the previous sections focused on quantifying the relevant data, visualizations of the finned tube bundles will be presented here. Because of the complex geometry, investigating all the different phenomenas is a rather difficult task. An attempt is made to describe the most important phenomenas affecting the fluid flow and heat transfer.

5.6.1 Fluid flow behavior

Hofmann [10] states that the most important effects occurring in a finned tube bundle is the three-dimensional boundary-layer development and the subsequent flow separation effects. Based on the definition of the Reynolds number the boundary layer thickness must be thinner for higher Reynolds numbers, as this means the viscous effects are smaller than for lower Reynolds numbers. Fig. 5.26 shows the velocity distributions in the stagnation plane upstream of the second tube row between two adjacent solid fins (symmetry condition applies between the two fins). As can be seen from both subfigures, a turbulent boundary layer starts to grow at the fin tip. As the fluid streams down the fin surface, the velocity reduces. As expected, the boundary layer is thinner for the case with the higher Reynolds number. Another important flow phenomena is seen from fig. 5.26. At the junction of the fin and tube, the formation of horseshoe vortexes takes place.

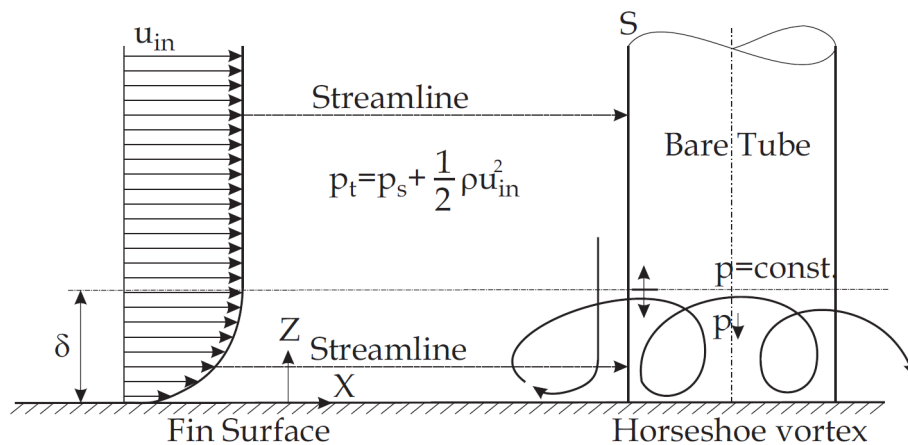


Figure 5.25: Schematic explaining formation of horseshoe vortex at the leading part of the tube (taken from Hofmann [10])

Horseshoe vortexes develop as a result of the negative pressure gradient towards the fin surface. Close to the tube wall, the flow can not stand this pressure gradient. The flow rolls backwards and form a horseshoe vortex. This effect is shown schematically in fig. 5.25. The same effect is seen downstream of the finned tube, although in less magnitude. The horseshoe vortexes causes an increase in the heat transfer rate due to the increased

mixing of the flow. Horseshoe vortices are also observed in the studies performed by Hofmann [10] and Mon [16]. Also for geometry 2 and 3 (see fig. 5.27 and 5.28) horseshoe vortices can be seen. The horseshoe vortex seems to be less prominent in geometry 3.

Fig. 5.29, 5.30 and 5.31 show the velocity profiles in the mid-plane between the fins for a low and high Reynolds number for the three geometries respectively. For all cases except for geometry 1 at a high Reynolds number, dead-zones appear behind row two through eight, where there is little to no circulation of the flow. These dead-zones definitely affect the heat transfer in the finned tube bundle in a negative manner since such a low portion of the hot air flows directly downstream of the finned tubes. For geometry 1 with the high Reynolds number swirls/circulation zones appear behind row two through eight. Since the simulations in the present study is steady and not transient it is hard to tell the amount of mass transfer between the circulation zones and the main flow taking place.

The flow pattern from row one to two seen for all three geometries could explain the enhanced heat transfer happening at the second row, discussed in section 5.2.3. The flow effects, made by the first row causes the air to enter the second rows with a much higher velocity than the inlet velocity of the tube bundle which increases the convective heat transfer.

Fig. 5.32 and 5.33 shows the turbulent activity for a low and high Reynolds number for geometry 1 and 3. The parameter visualized is turbulent kinetic energy, k introduced in section 3.1.1. From the two cases with high Reynolds numbers it can be seen that the flow is highly turbulent between the finned tube rows. No clear differences can be seen between the geometry 1 with solid fins and geometry 3 with serrated fins, although the turbulence seems to be more consistent over the whole finned tube bundle for geometry 3 with serrated fins. The peak of turbulence seems to be higher directly downstream of the tube rows for geometry 1 than for geometry 3.

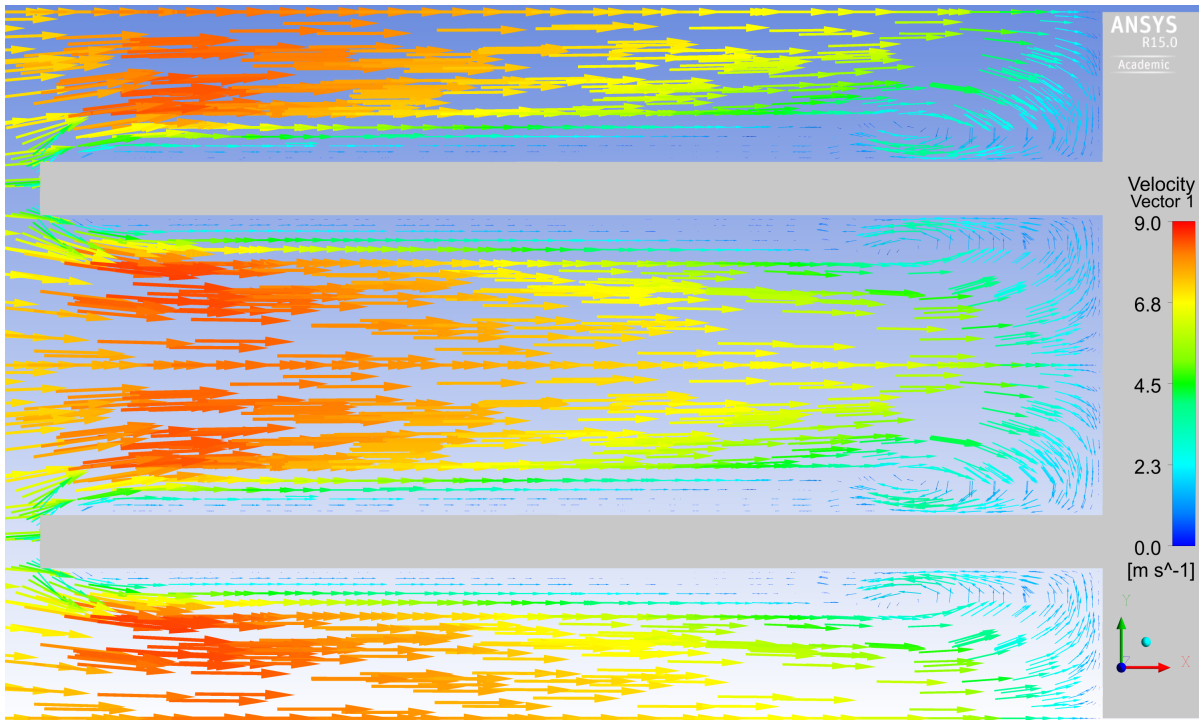
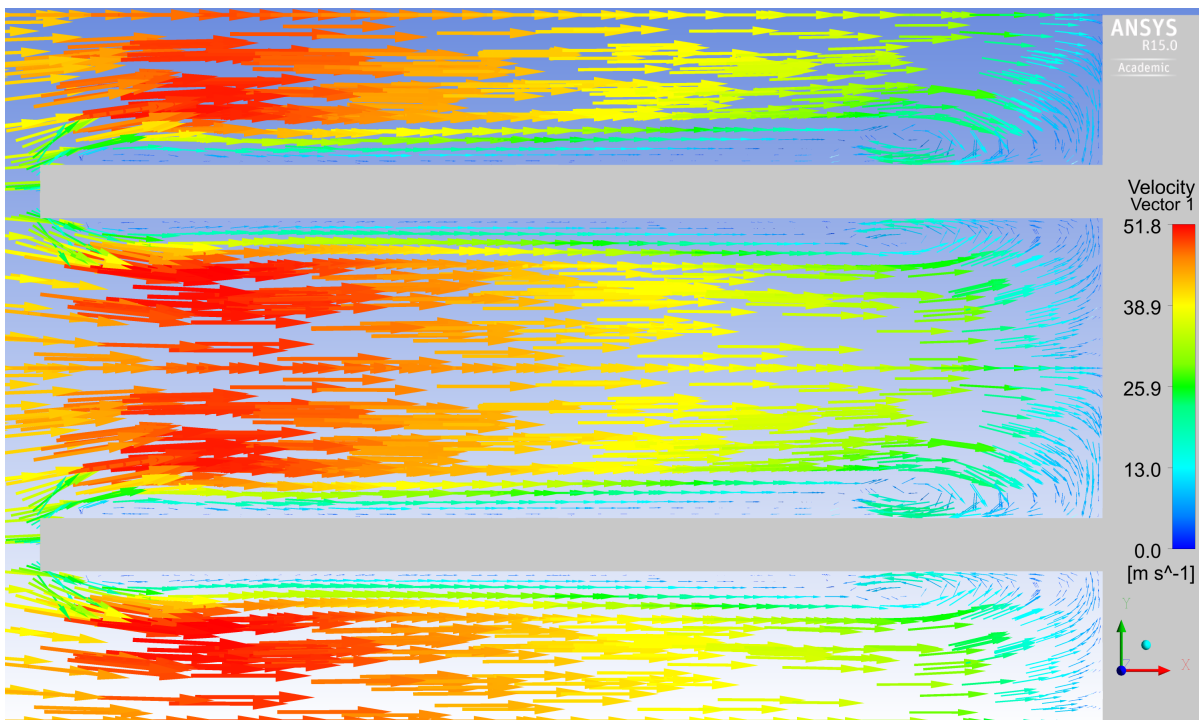
(a) $Re = 4397$ (b) $Re = 26086$

Figure 5.26: Velocity distributions between the fins of second row in symmetry plane at low and high Reynolds number for geometry 1

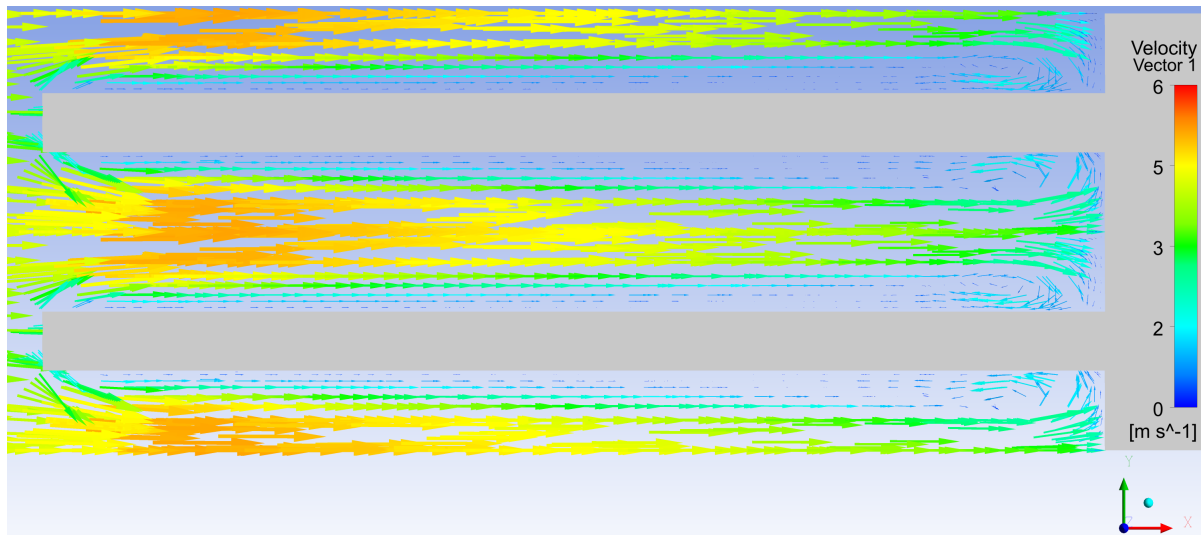
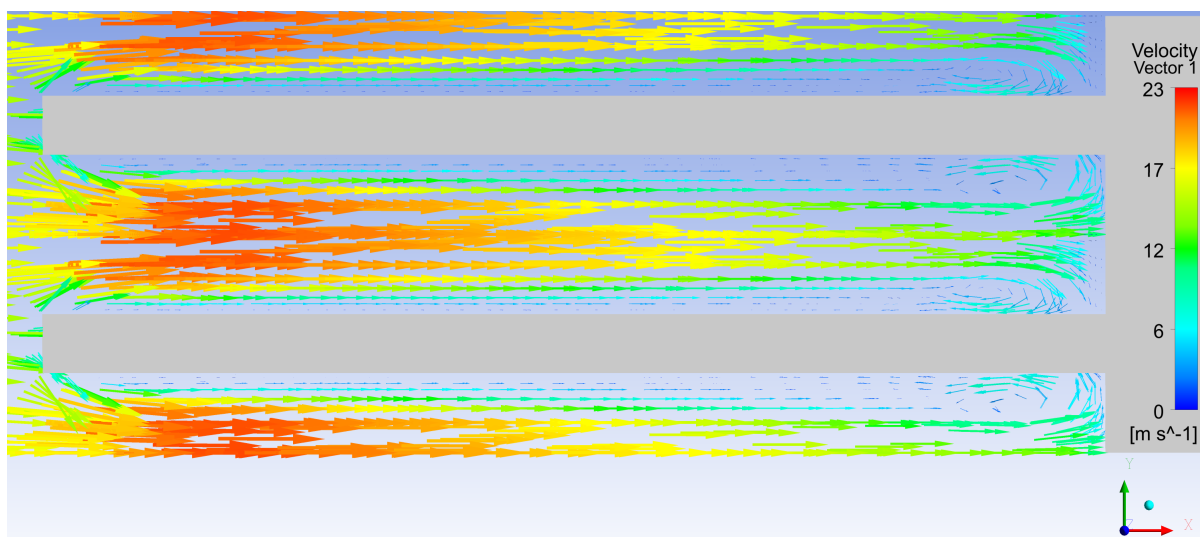
(a) $Re = 5793$ (b) $Re = 26017$

Figure 5.27: Velocity distributions between the fins of second row in symmetry plane at low and high Reynolds number for geometry 2

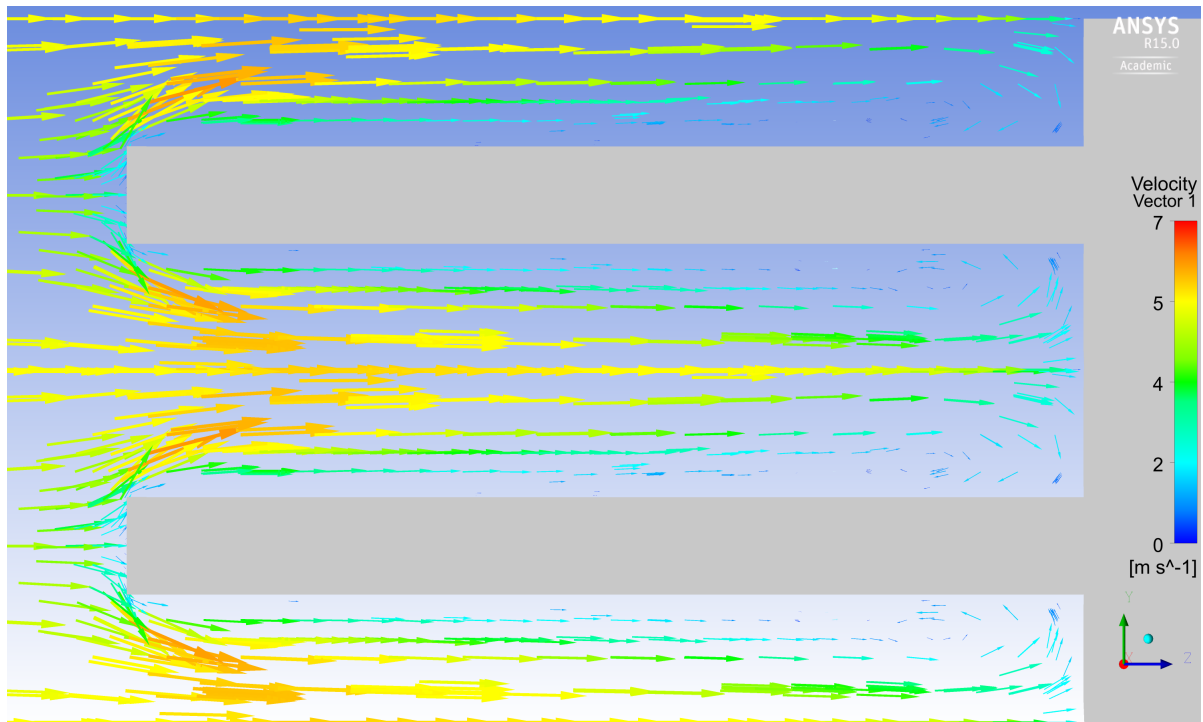
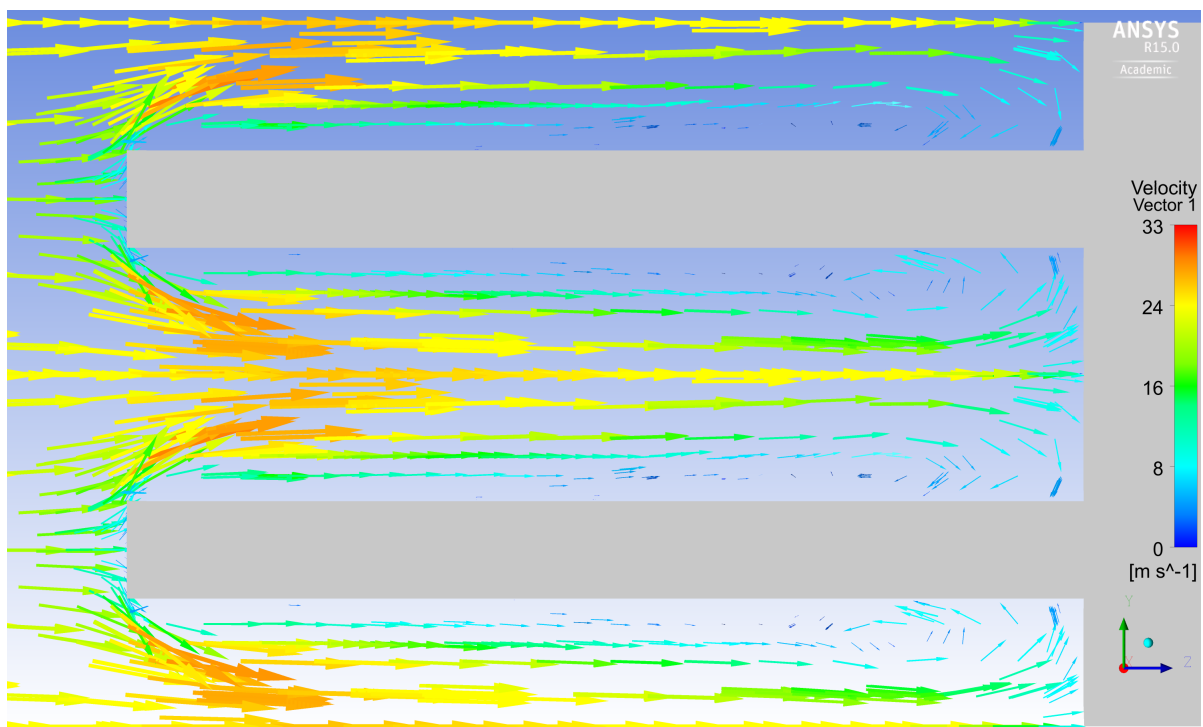
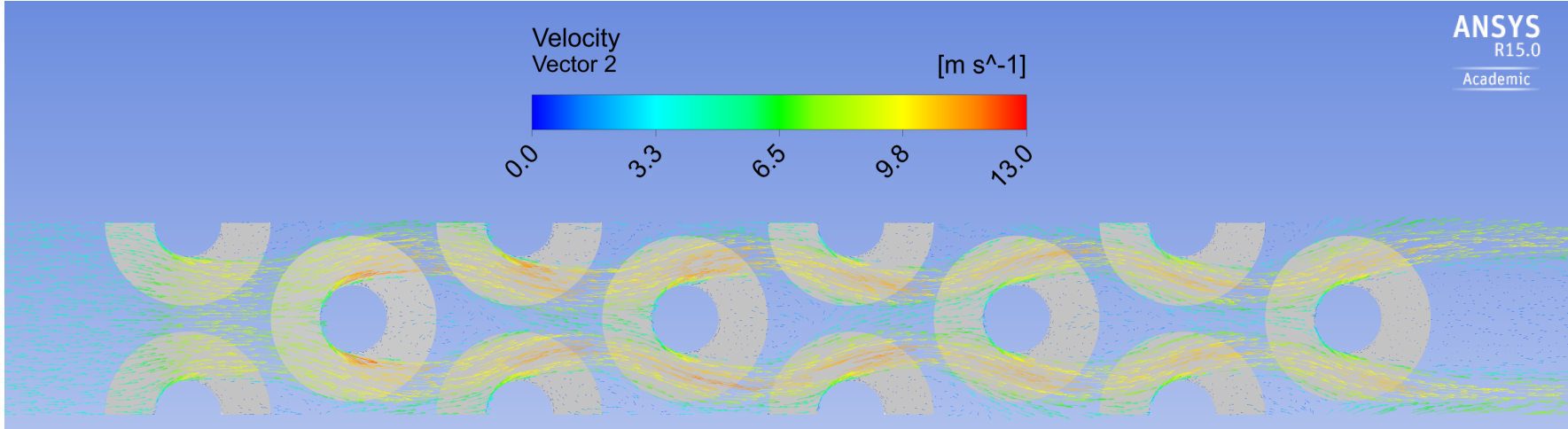
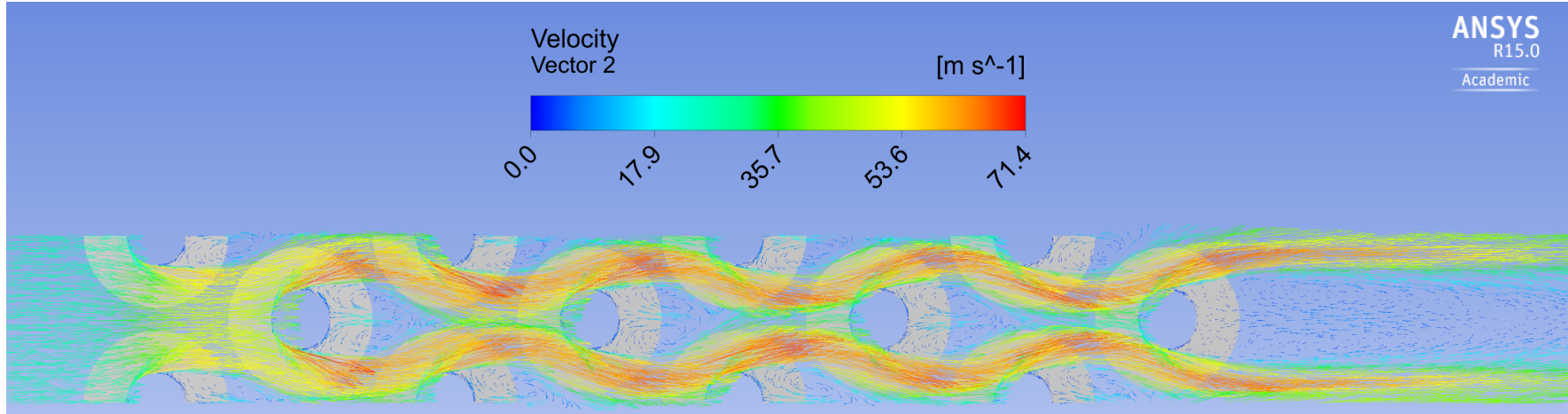
(a) $Re = 4802$ (b) $Re = 25090$

Figure 5.28: Velocity distributions between the fins of second row in symmetry plane at low and high Reynolds number for geometry 3



(a) $Re = 4397$



(b) $Re = 26086$

Figure 5.29: Velocity profile in mid-plane between fins for geometry 1

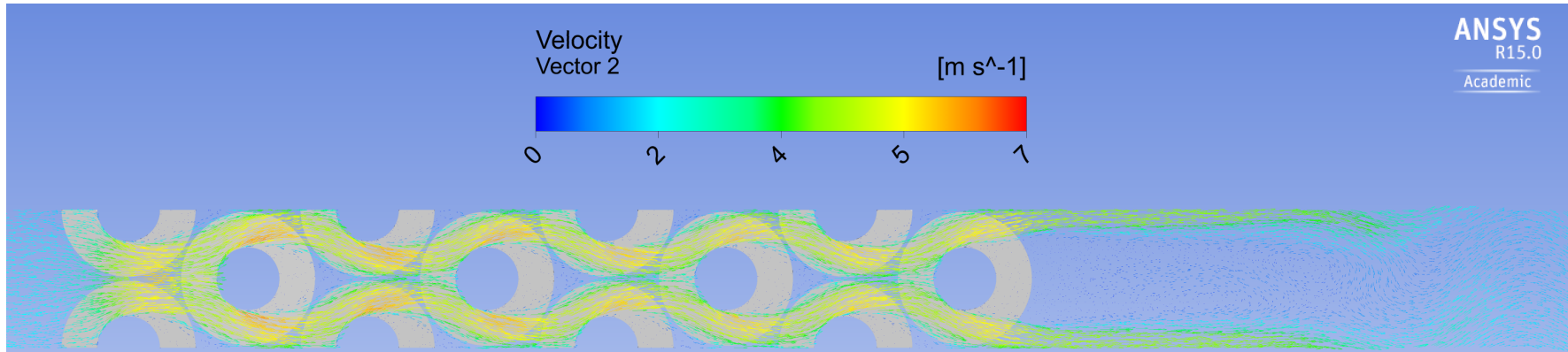
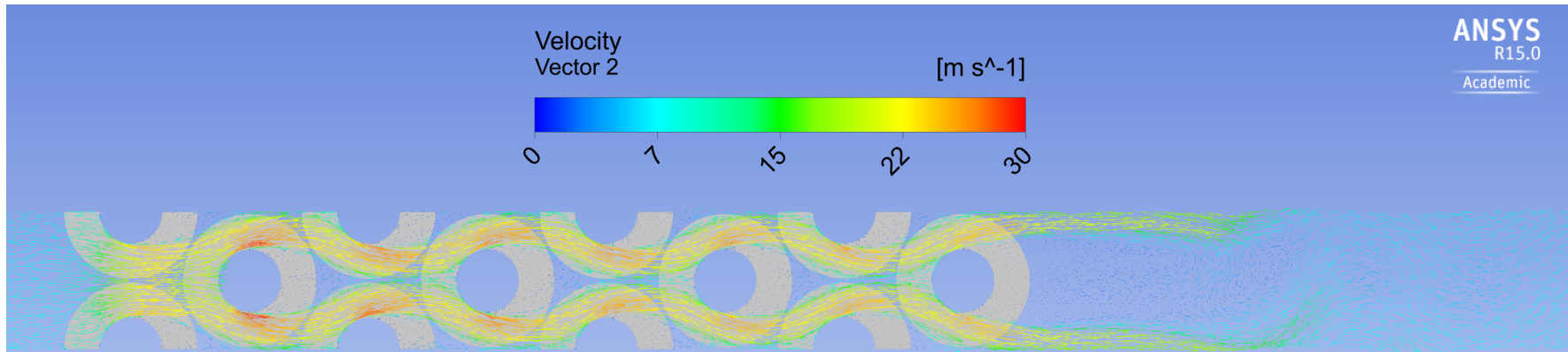
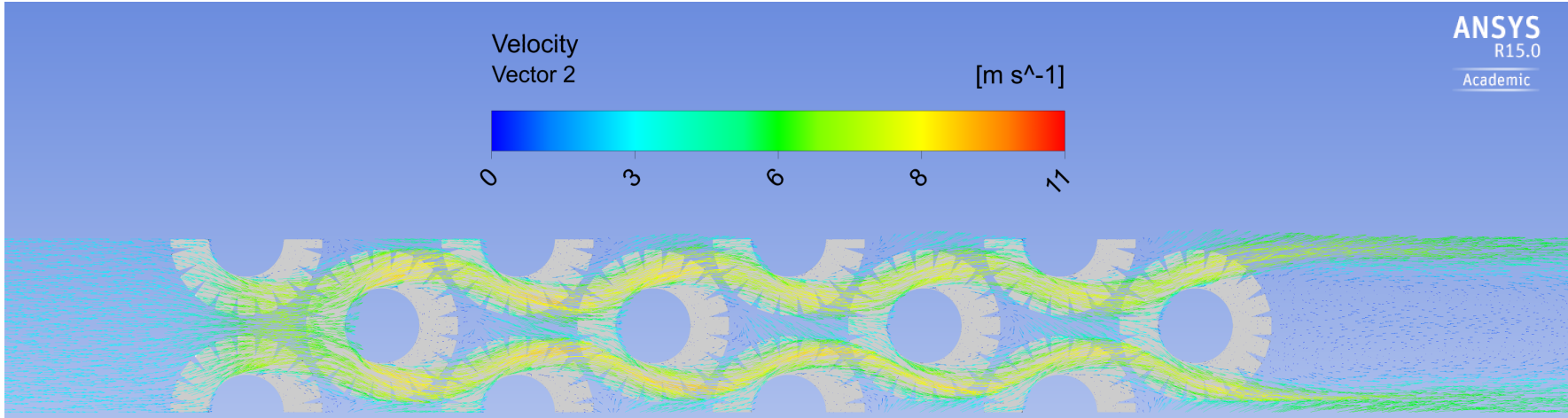
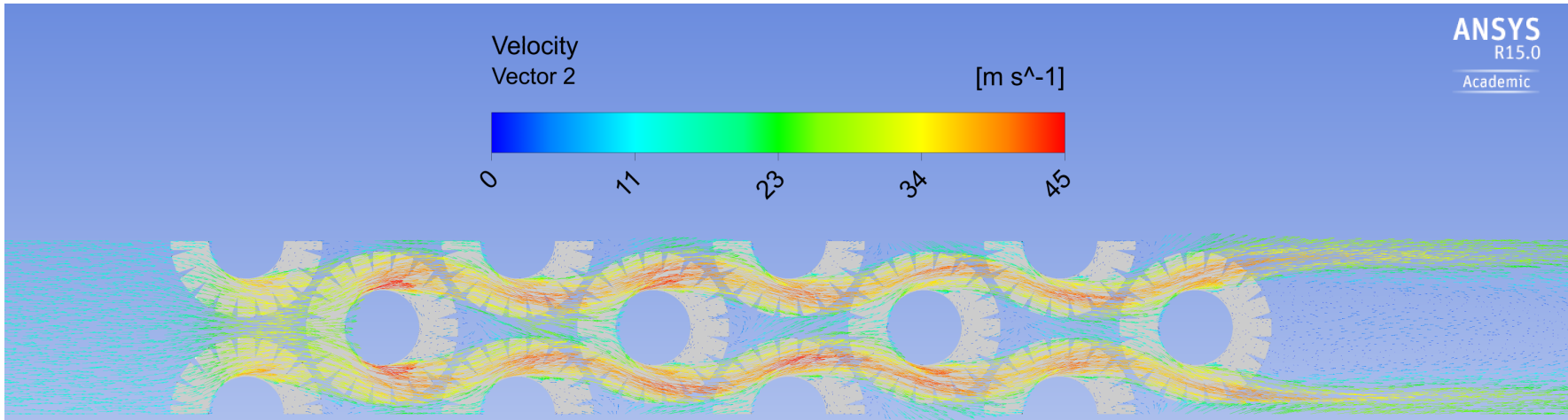
(a) $Re = 5793$ (b) $Re = 26017$

Figure 5.30: Velocity profile in mid-plane between fins for geometry 2

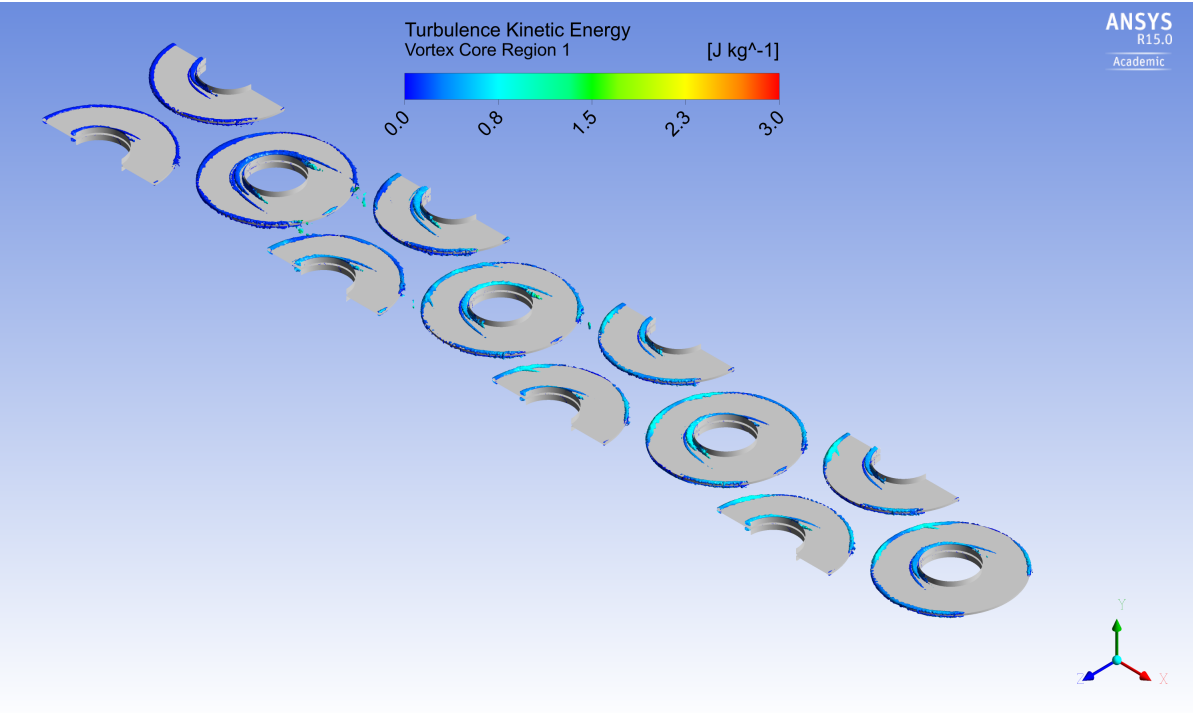


(a) $Re = 4802$

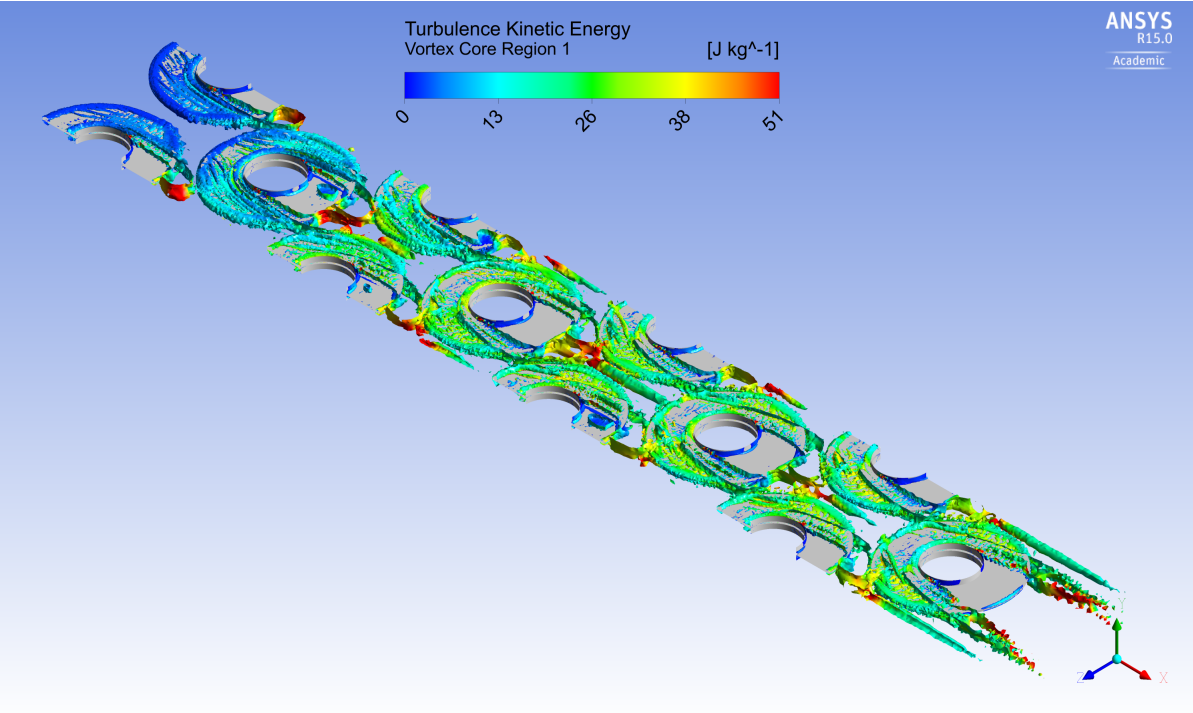


(b) $Re = 25090$

Figure 5.31: Velocity profile in mid-plane between fins for geometry 3



(a) $Re = 4397$



(b) $Re = 26086$

Figure 5.32: Turbulence in the finned tube bundle for geometry 1

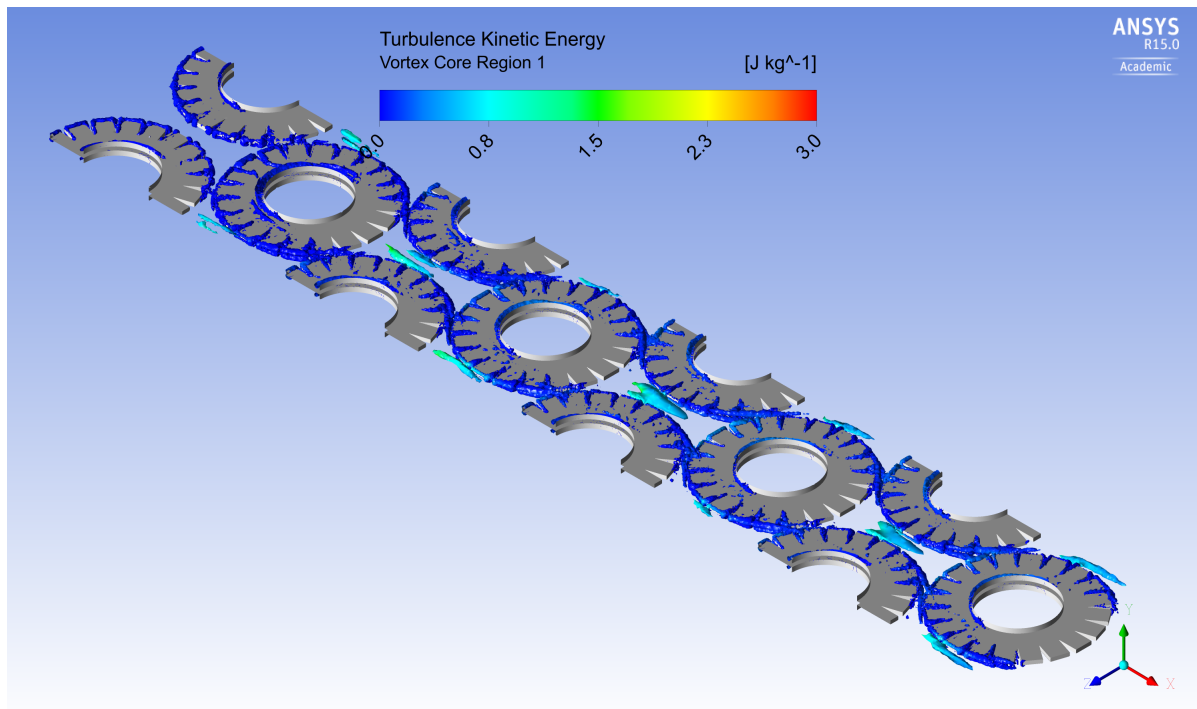
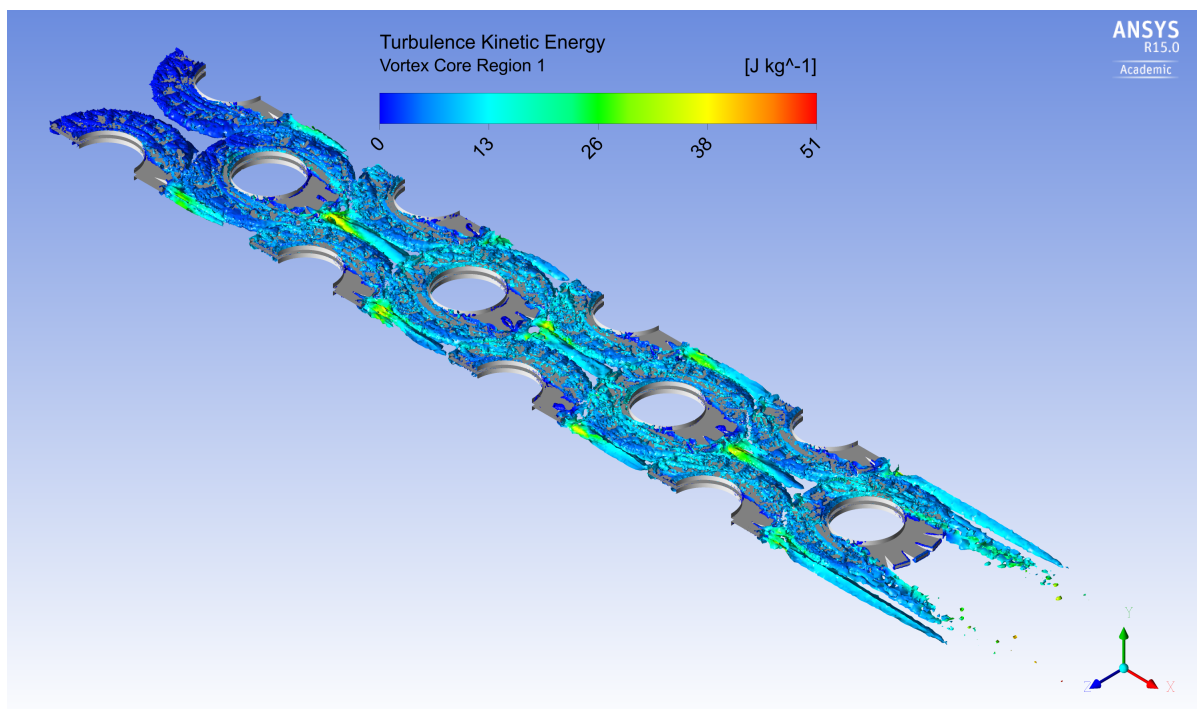
(a) $Re = 4802$ (b) $Re = 25090$

Figure 5.33: Turbulence in the finned tube bundle for geometry 3

5.6.2 Heat transfer behavior

Thermal boundary layer formation, the temperature distribution over the fins and the wall heat flux are important parameters to investigate when looking at heat transfer behavior in a finned tube bundle. Fig 5.34, 5.35 and 5.36 shows the temperature distribution over the fins for the three geometries. A non-uniform temperature profile over the fins can be seen for all cases. The dead-zones/circulation zones behind each tube row (seen in fig. 5.29-5.31), cause the fins to have a much lower temperature in the back of each finned tube than in the front. Remember that one of the assumptions when finding the theoretical fin efficiency is uniform heat transfer coefficients across the fins. Based on the temperature distribution this assumption clearly does not hold even for a fin-material like Aluminum with high conductivity. It is therefore surprising that the simulated fin efficiencies lies close to the theoretical fin efficiencies (see fig. 5.9 for example).

Fig. 5.37 shows the thermal boundary layer development at a low and high Reynolds number for geometry 1 at the stagnation plane upstream of the second finned tube row. As expected the boundary layer is thicker for the low Reynolds number where the viscous effects are more prominent. For both cases the boundary layers clearly break up close to the junction of the fin and tube. This is most likely caused by the horseshoe vortexes shown in 5.26. Clearly the break-up of the boundary-layer is a positive effect since more of the hot air gets in contact with the fin walls. For geometry 1 with a high fin pitch the thermal boundary layers between two fins are never in danger of touching each other. Geometry 2 has a smaller fin pitch relative to the fin thickness than geometry 1. As can be seen from fig. 5.38 this affects the temperature distribution. Although the thermal boundary-layers do not touch each other, the temperature between the fins for geometry 2 is generally lower than for geometry 1. Break-up of the boundary-layer at the junction of the fin and tube can be seen also for geometry 2. Geometry 2 is a compact finned tube bundle with a fin tip clearance of only $2mm$. In fig. 5.38(a) upstream of the fin it can be seen that the entering flow has an uneven temperature distribution caused by the preceding row. This effect is not seen for geometry 1.

Fig. 5.39, showing the temperature distribution between the fins for geometry 3 clearly differs from 5.37 and 5.38. As discussed in the previous chapter, geometry 3 lacks prism layers close to the walls. As can be seen from the figure this results in a worse near-wall modeling. Especially the modeling of the thermal boundary-layer is disrupted. This is most likely a part of the reason to why the numerical model over-predicts the heat transfer when compared to the experimental result (see section 5.4.3). Fig. 5.40, 5.41 and 5.42 displaying the heat flux from the walls to the hot air for the three geometries, shows as expected that the heat flux is lower in the back of each finned tube. The case with the highest Reynolds number for geometry 1 (fig. 5.40(a)) shows a notable heat flux taking place downstream of the fins. This effect is not seen for geometry 2. This heat flux is probably caused by the circulation zones seen in fig. 5.29.

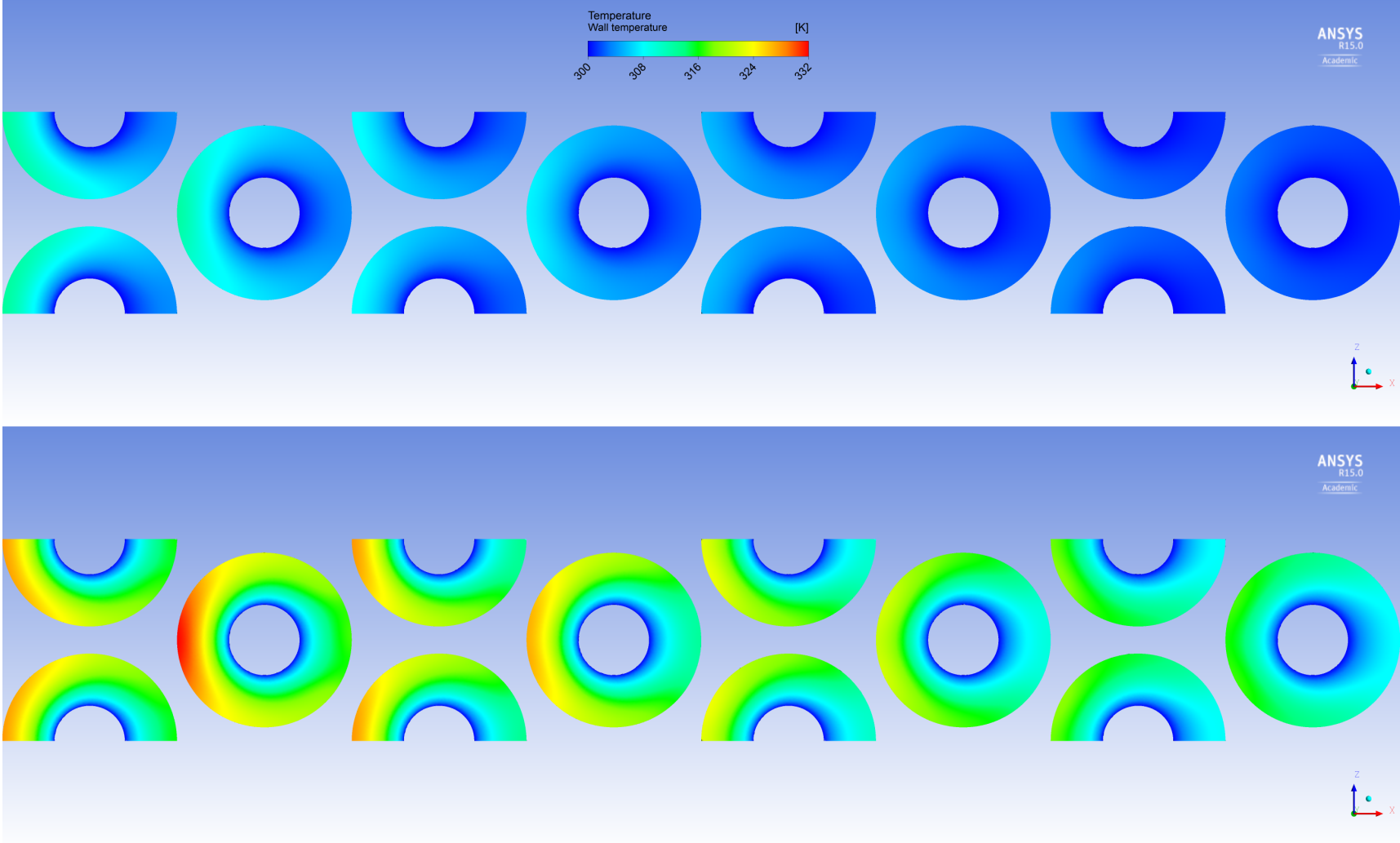


Figure 5.34: Wall temperature for $Re = 4397$ (top) and $Re = 26086$ (bottom) for geometry 1

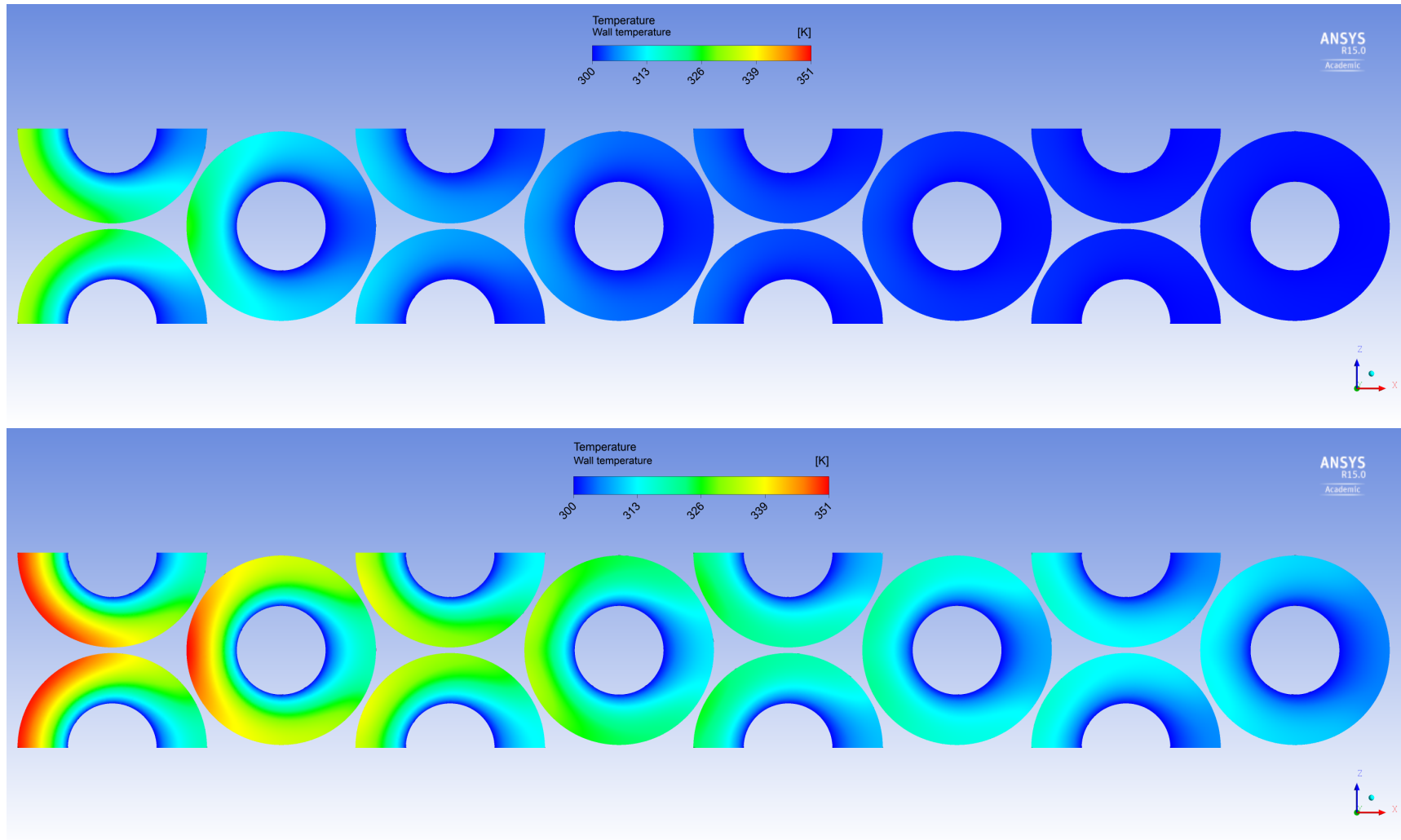


Figure 5.35: Wall temperature for $Re = 5793$ (top) and $Re = 26017$ (bottom) for geometry 2

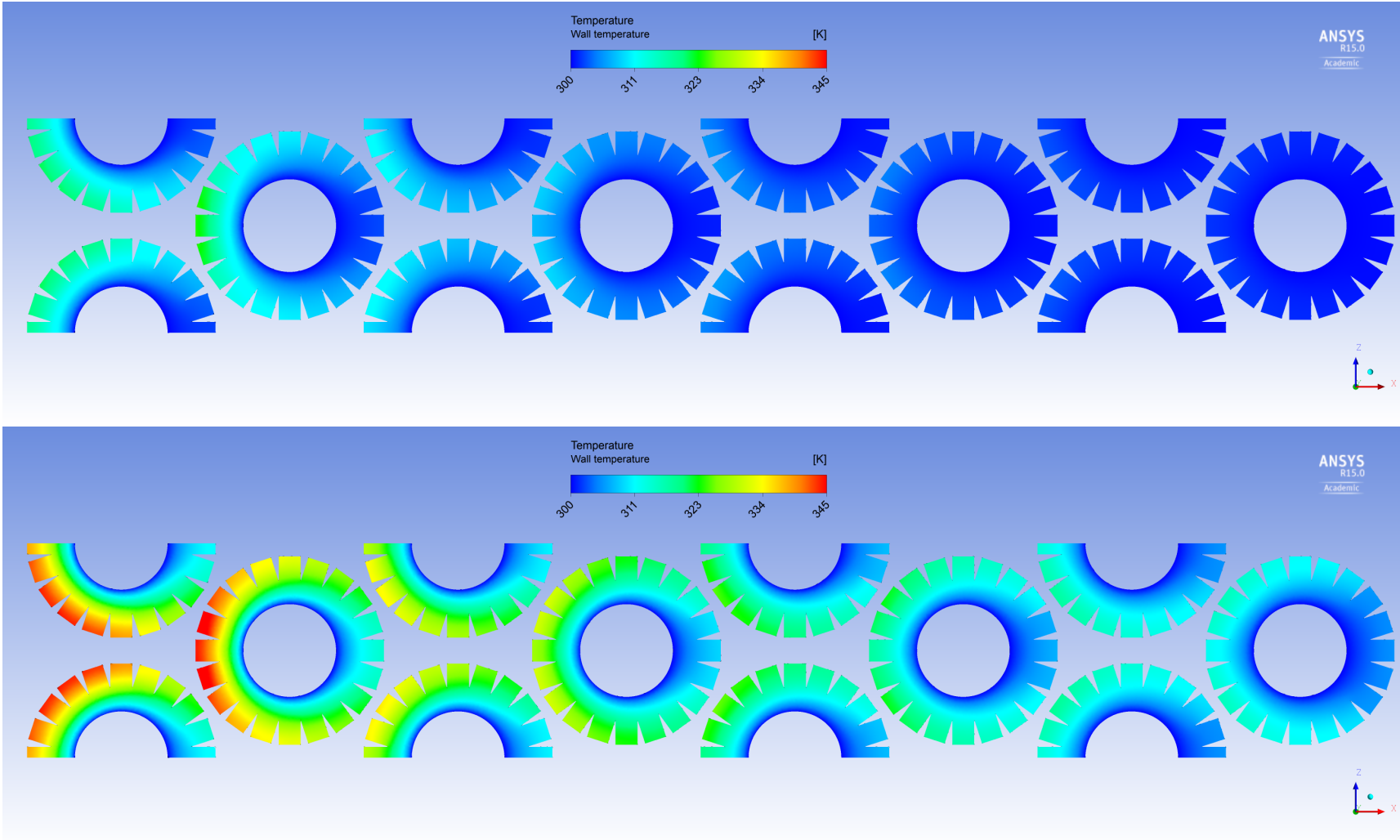


Figure 5.36: Wall temperature for $Re = 4802$ (top) and $Re = 25090$ (bottom) for geometry 3

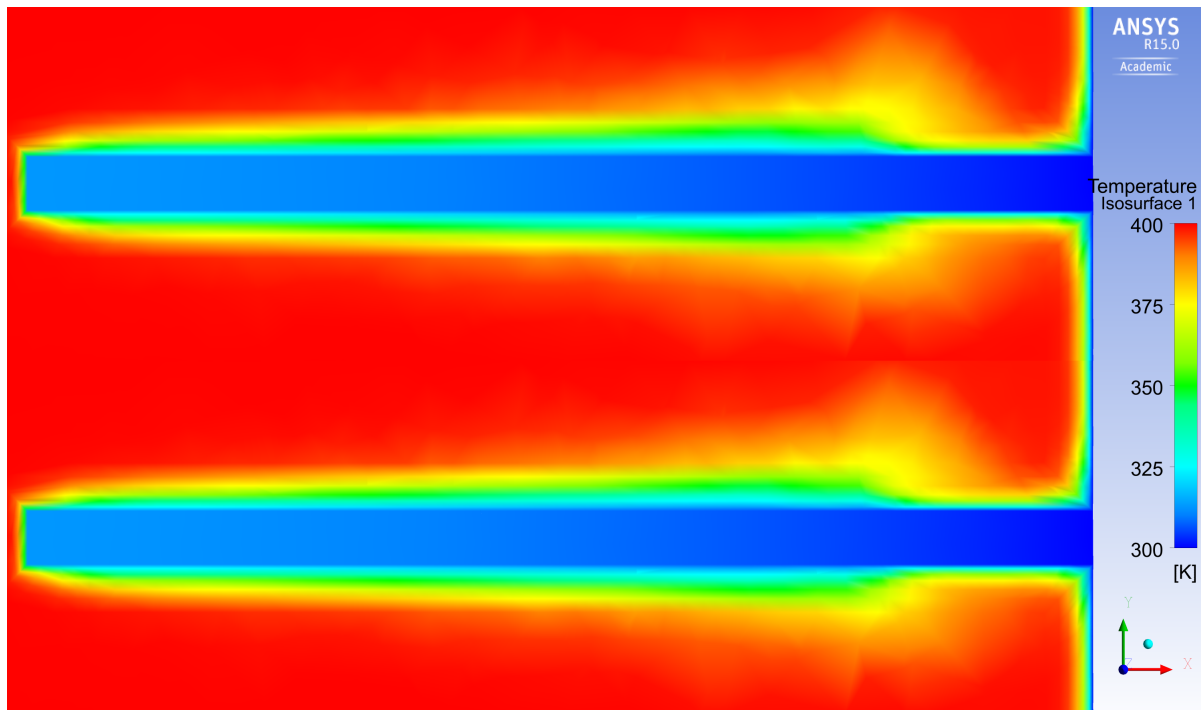
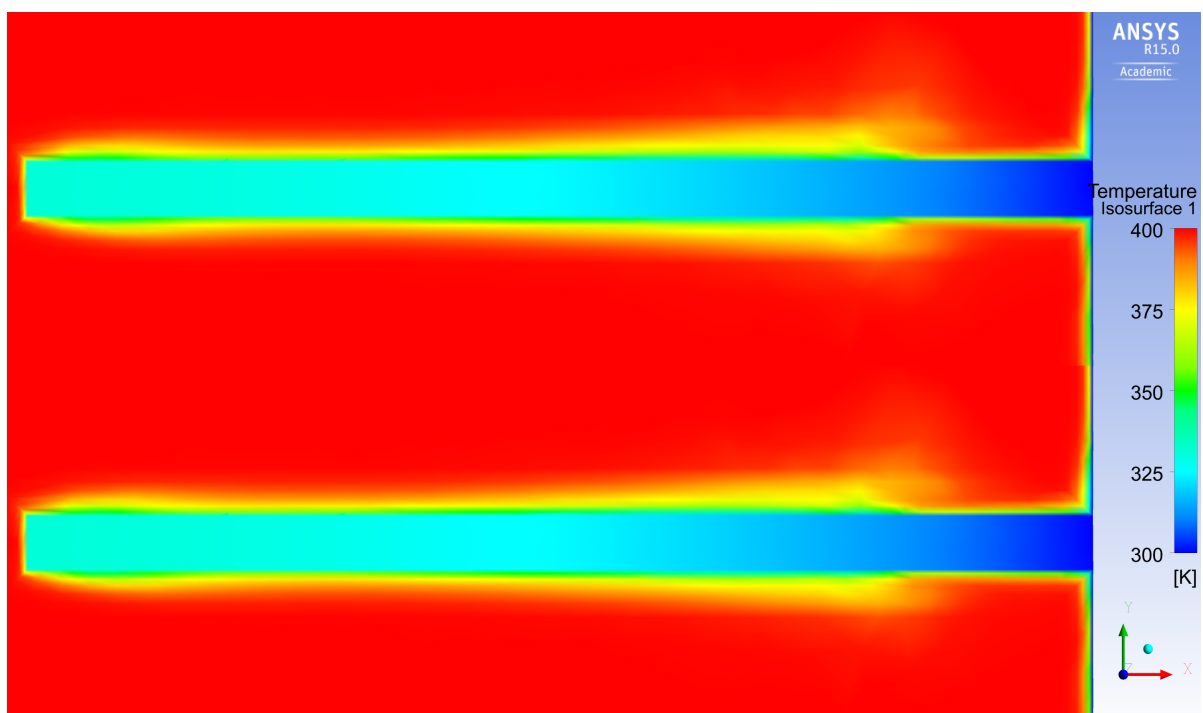
(a) $Re = 4397$ (b) $Re = 26086$

Figure 5.37: Temperature distributions between the fins upstream of second row in symmetry plane at low and high Reynolds number for geometry 1

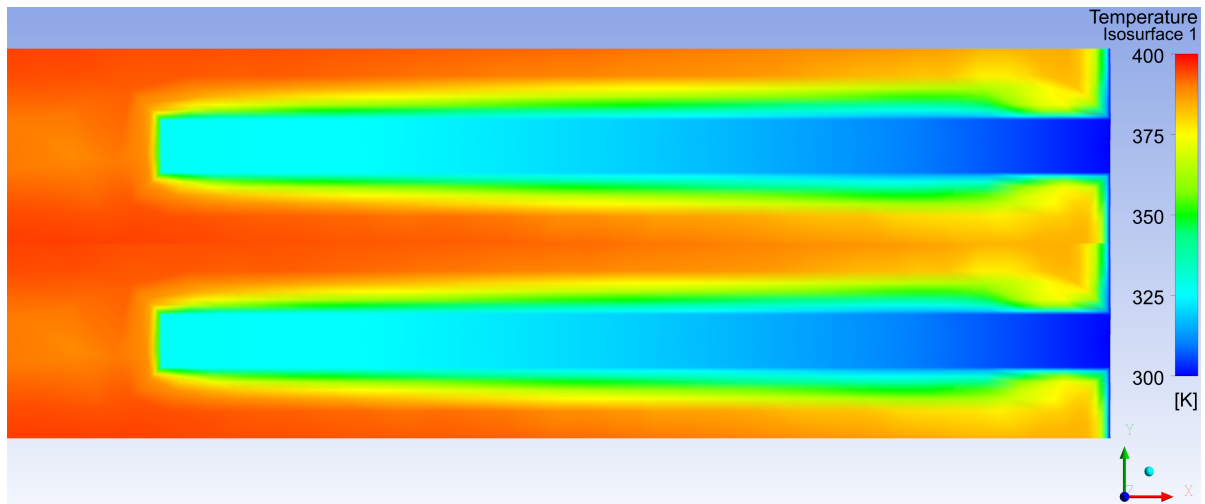
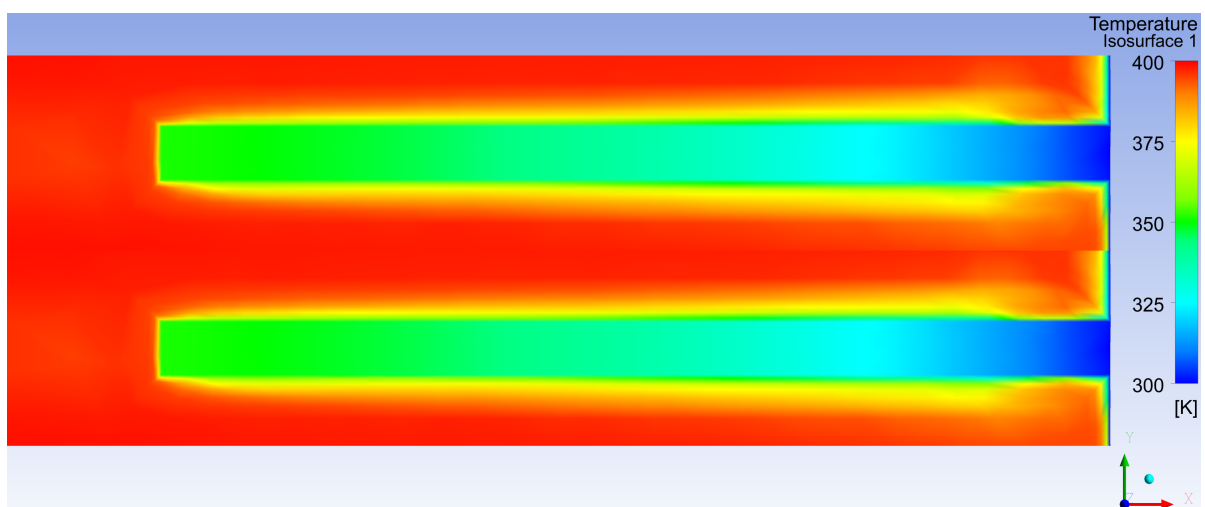
(a) $Re = 5793$ (b) $Re = 26017$

Figure 5.38: Temperature distributions between the fins upstream of second row in symmetry plane at low and high Reynolds number for geometry 2

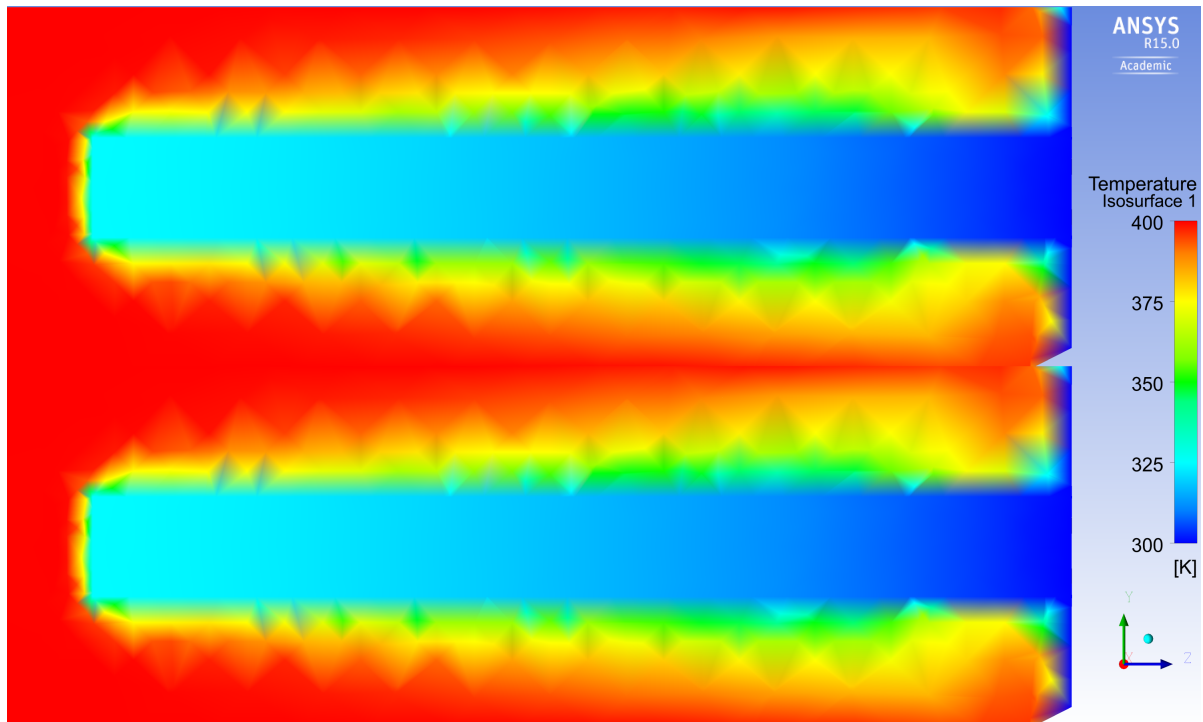
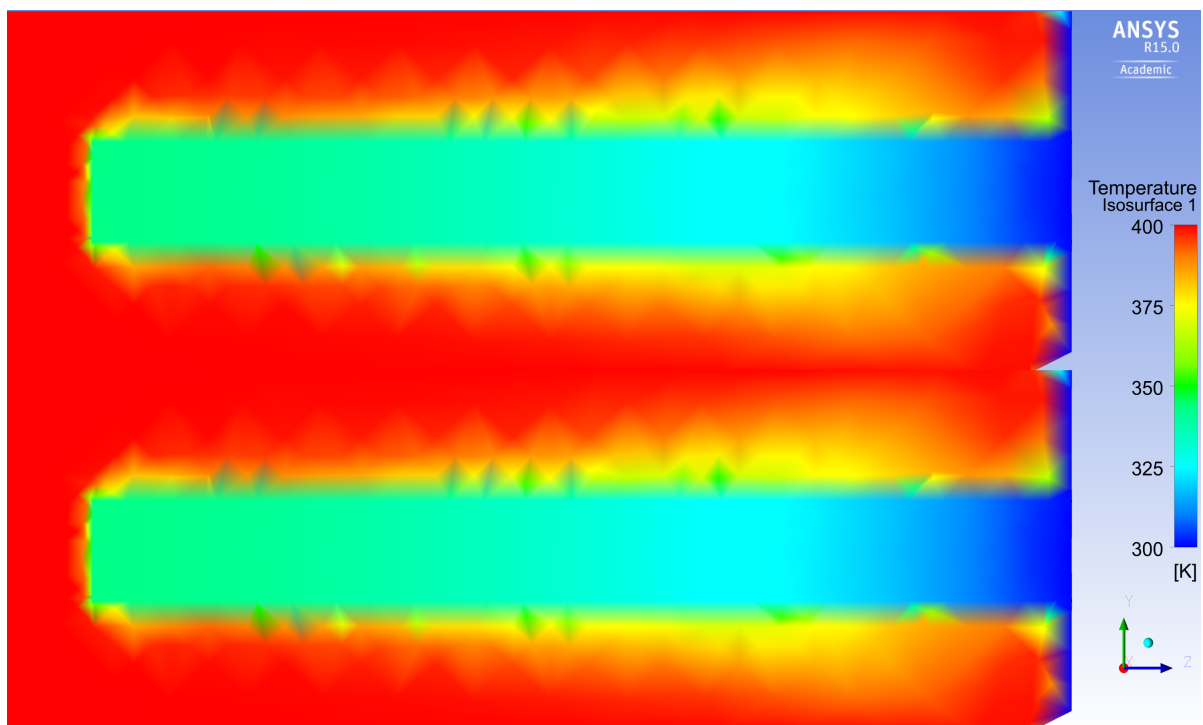
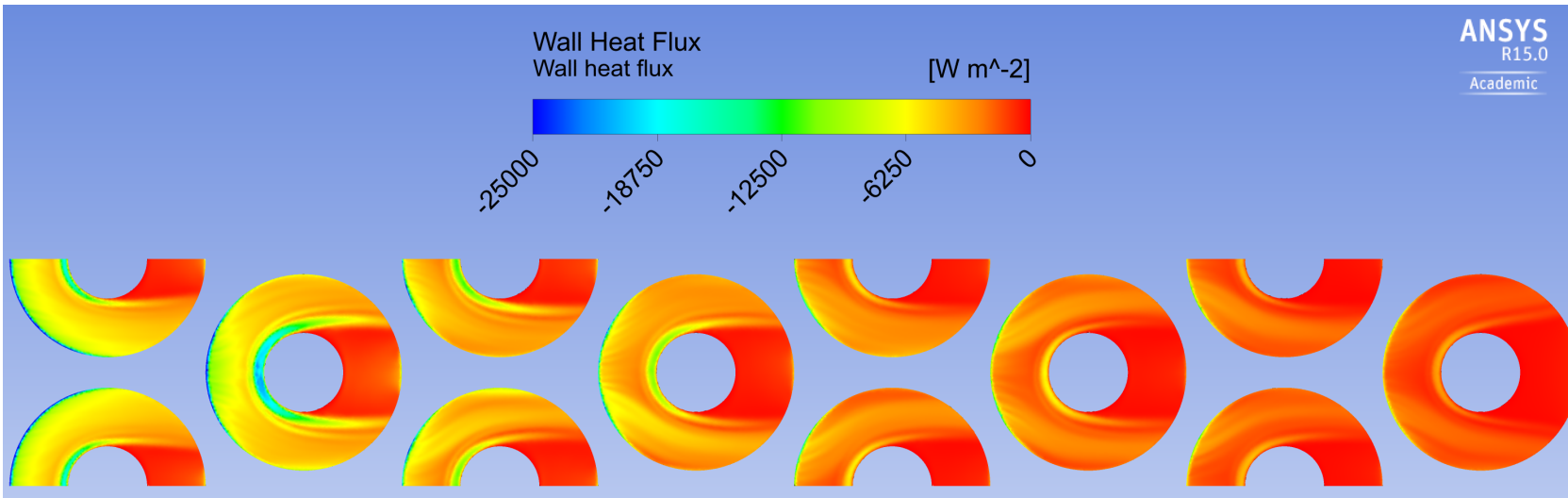
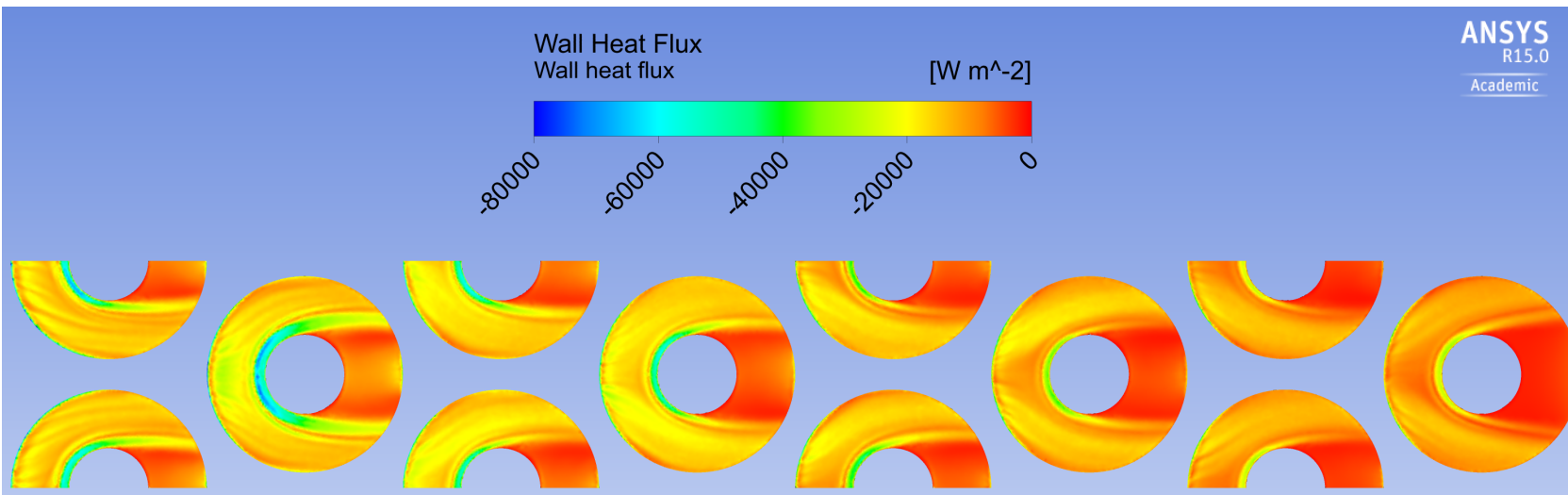
(a) $Re = 4802$ (b) $Re = 25090$

Figure 5.39: Temperature distributions between the fins upstream of second row in symmetry plane at low and high Reynolds number for geometry 3



(a) $Re = 4397$



(b) $Re = 26086$

Figure 5.40: Wall heat flux at the fins for geometry 1

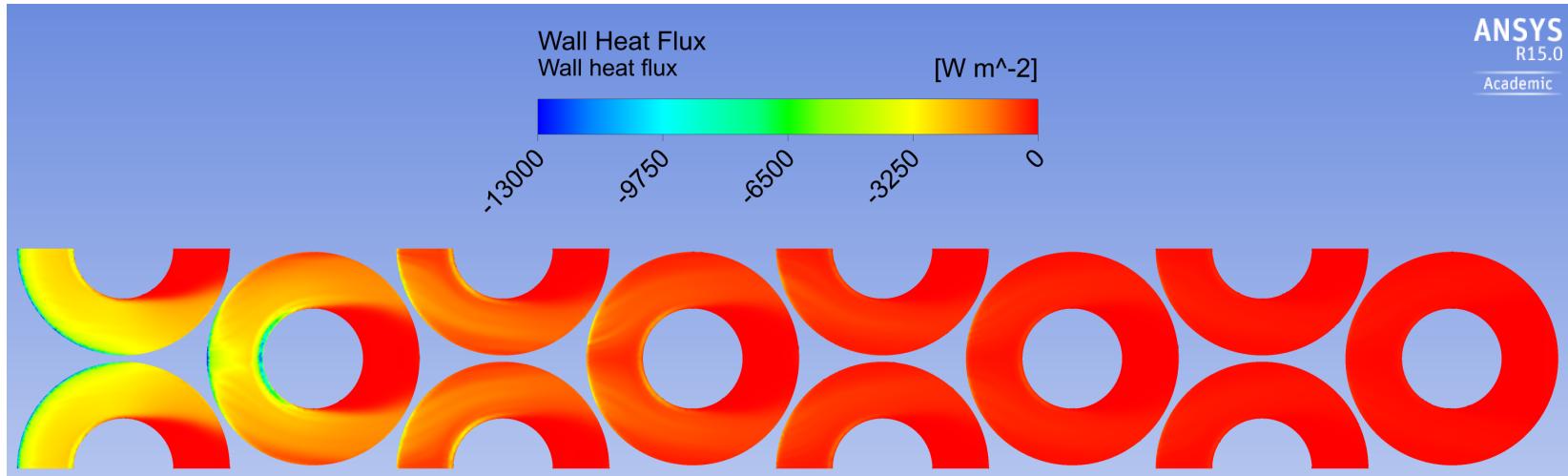
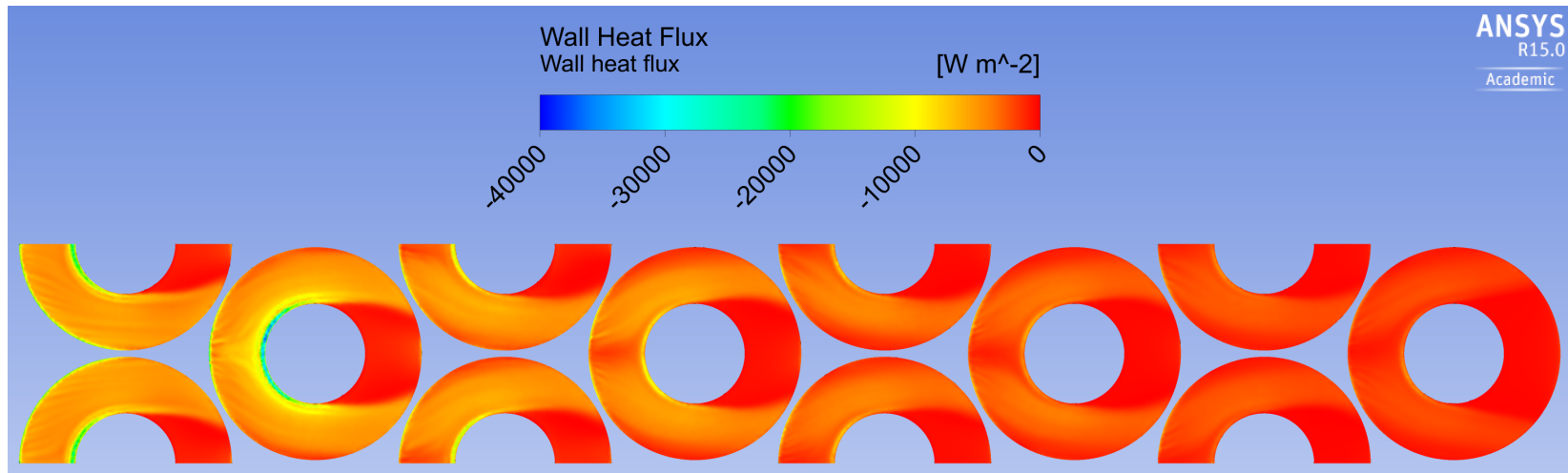
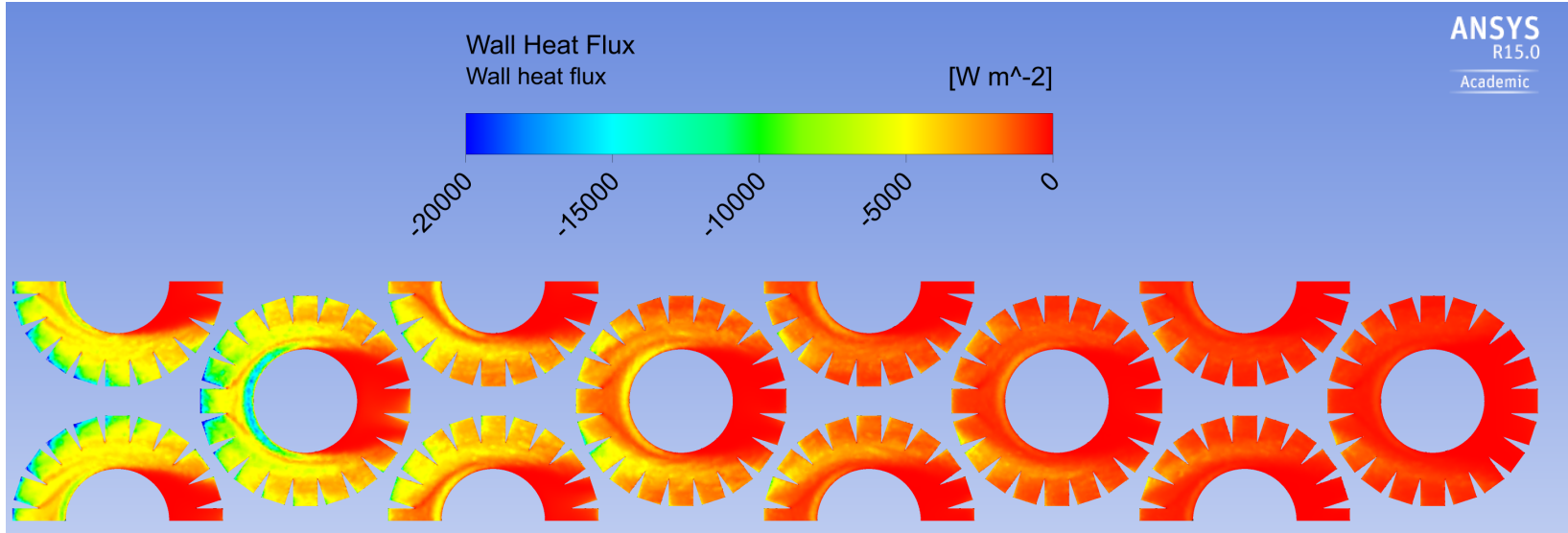
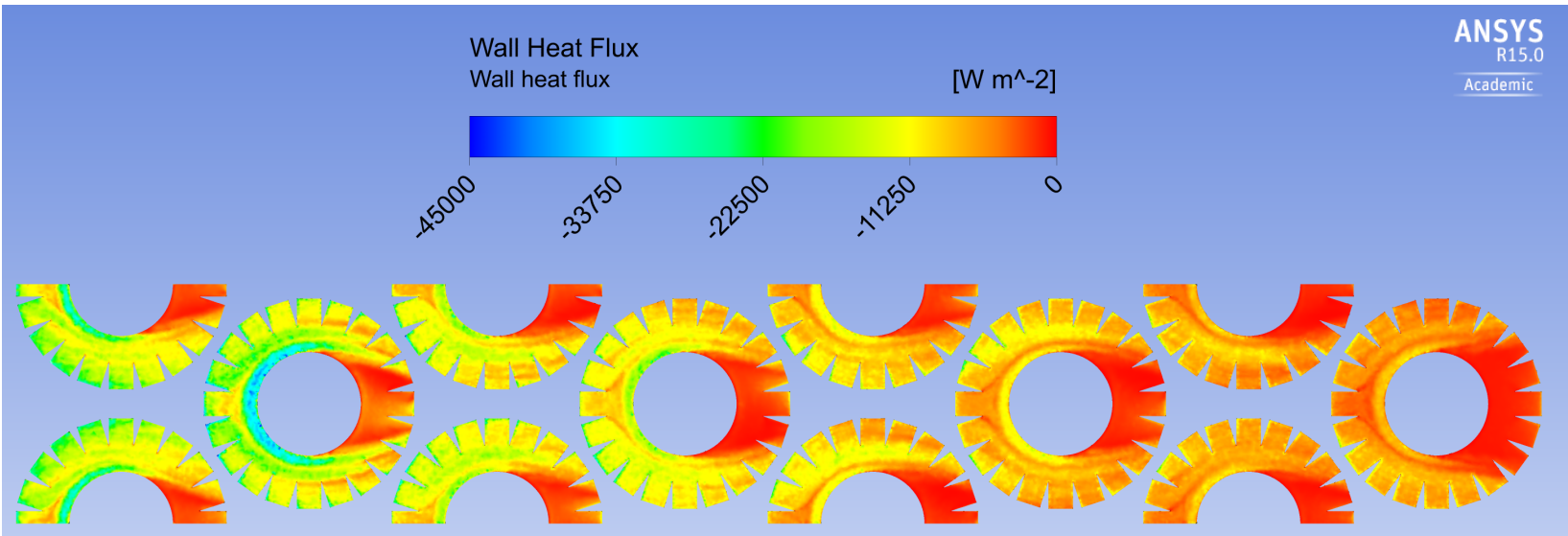
(a) $Re = 5793$ (b) $Re = 26017$

Figure 5.41: Wall heat flux at the fins for geometry 2



(a) $Re = 4802$



(b) $Re = 25090$

Figure 5.42: Wall heat flux at the fins for geometry 3

Chapter 6

Conclusions

The pressure drop performance and heat transfer in three finned tube bundles have been determined with a CFD-analysis and compared to equivalent finned tube bundles used in experimental tests at NTNU performed by Holfeld [11].

The numerical model predicts the experimental data best for geometry 1 which consists of solid fins. The numerical model is able to calculate the overall Nusselt number of the finned tube bundle with a maximum deviation of 6.5% at $Re = 13916$. The maximum deviation for the Euler number between the numerical and experimental result for geometry 1 is 17.5% also at $Re = 13916$. The higher variations within the different correlations for the Euler number suggests that predicting the pressure drop performance is a more difficult task than predicting the heat transfer in a finned tube bundle.

For geometry 1 and 2 with solid fins the experimental and numerical development of the Nusselt number with increasing Reynolds number are in a fairly good agreement with the correlations from published literature. For geometry 3 with serrated fins the numerical Nusselt number differs from the experimental Nusselt number, but seems to be in better agreement with the correlations.

The results from section 5.5 shows that the simulated fin efficiencies lies closer to the theoretical fin efficiencies for solid finned tubes than for serrated finned tubes. This is in contradiction to the corrected fin efficiency developed by Weierman [25]. According to [25], serrated finned tubes are less influenced by non-uniformities in the heat transfer distribution. It can be concluded that the simulated fin efficiencies are in better agreement with the corrected fin efficiencies for materials with high conductivity.

Based on fig. 5.9, 5.15 and 5.21 it can be concluded that the simulated fin efficiency is in best agreement with the corrected fin efficiency from Weierman [25] at low Reynolds numbers. For high Reynolds numbers the simulated fin efficiencies lies closest to the corrected fin efficiency from Hashizume et al. [9].

From the visualizations it is clearly seen that the heat transfer distribution across the fins can be considered to be uneven for all three geometries having different fin materials. Important flow effects like horseshoe vortexes and flow separation can also be observed.

Chapter 7

Suggestions for Further Work

- Based on the prediction of the pressure drop performance for all three geometries (see fig. 5.5, 5.11 and 5.17) the simplification of making the fins annular around the tubes does not hold. In the future the fins should be twisted helically around the tubes in a similar manner like the experimental setup.
- If the fins are to be helically twisted around the tubes, the symmetry condition would not hold at the top/bottom outer boundary. Periodic interfaces should be applied in order for the fluid variables to be conservative across the top and bottom boundary.
- Fig. 5.39 clearly shows that prism layers needs to be grown close to the walls for all geometries.
- Based on fig. 5.3 a further refinement of the mesh should be considered also for geometry 1 and 2. Fig. 5.37 and 5.38 gives a clear indication on how thick the boundary-layer is expected to be. In order to improve the near-wall modeling more prism layers could be put in this region and in the transition region between the boundary-layer and the turbulent core. In order to ensure good aspect ratios the surface mesh at the finned tube walls needs to be made smaller accordingly. All in all this would result in a substantial increase of the mesh size and would require more computational capacity.
- The simulations should be made transient. Most of the earlier studies on finned tube bundle considers the steady-state approach to be adequate. However, if the simulations were to be transient, it would be possible to investigate the development of the circulation zones behind the tube rows for example. It would be interesting to investigate the rate of mass transfer happening between the main flow and the circulation zones. Making the simulations transient would require more computational capacity.
- An uneven temperature distribution can be seen on the fins for all cases in the

numerical model. It is therefore surprising that the simulated fin efficiencies for geometry 1 and 2 lies so close to the theoretical fin efficiencies. Deviations are seen between the existing corrections for the fin efficiencies. A further study should be done on how uneven heat distributions affects the fin efficiency.

Appendix A

Thermo-Physical Properties

A.1 Air

In the simulations the thermo-physical properties of dry air are considered with the help of polynomial functions. For the thermal conductivity and dynamic viscosity the polynomial functions were taken from VDI (2010). This is the same functions as used under the experimental studies performed in the laboratory at NTNU. The thermal conductivity and dynamic viscosity is calculated according to eq. A.1, using the coefficients given in tab. A.1. The specific heat capacity is found in a similar way, but the coefficients are taken from Principles of Engineering Thermodynamics [17].

$$\lambda_{air}/\mu_{air}/C_{P,air} = A + B \cdot T + C \cdot T^2 + D \cdot T^3 + E \cdot T^4 \quad (\text{A.1})$$

	Thermal conductivity	Dynamic viscosity	Specific heat capacity
	$\lambda_{air}[W/m \cdot K]$	$\mu_{air}[Pa \cdot s]$	$C_{P,air}[J/kg \cdot K]$
A	$-0.908 \cdot 10^{-3}$	$-0.01702 \cdot 10^{-5}$	1048.5066
B	$0.112 \cdot 10^{-3}$	$0.79965 \cdot 10^{-7}$	-0.3838
C	$-0.084333 \cdot 10^{-6}$	$-0.72183 \cdot 10^{-10}$	$9.4546 \cdot 10^{-4}$
D	$0.056964 \cdot 10^{-9}$	$0.046960 \cdot 10^{-12}$	$-5.4908 \cdot 10^{-7}$
E	$-0.015631 \cdot 10^{-12}$	$-0.01388 \cdot 10^{-15}$	$7.9305 \cdot 10^{-11}$

Table A.1: Coefficients for eq. A.1

A.2 Aluminum

Thermal conductivity for Aluminum is considered using the function made by Lundberg (1997). This is the same function as used under the experimental studies performed in

the laboratory at NTNU.

$$\lambda_{Al} = A + B \cdot T \quad (\text{A.2})$$

Here, $A = 190$ and $B = 0.074$.

The specific heat capacity is considered to be constant and is set to $C_{P,Al} = 871 [J/kg \cdot K]$. This is the default value set in ANSYS Fluent.

A.3 Carbon Steel

For the thermal conductivity and specific heat capacity for Carbon Steel, polynomial functions from Hofmann [10] are used. See eq. A.3 and A.4 and tab. A.2.

$$C_{P,cs} = A + B \cdot T + C \cdot T^2 + D \cdot T^3 \quad (\text{A.3})$$

$$\lambda_{cs} = A + B \cdot T + C \cdot T^2 \quad (\text{A.4})$$

	Thermal conductivity	Specific heat capacity
	$\lambda_{cs} [W/m \cdot K]$	$C_{P,cs} [J/kg \cdot K]$
A	66.17504949	185.8537793
B	-0.03482879	1.272598818
C	0.0000233	-0.0017157
D		$9.1 \cdot 10^{-7}$

Table A.2: Coefficients for eq. A.3 and A.4

Appendix B

Heat Transfer and Pressure Drop Correlations for Finned Tube Heat Exchangers Taken From Literature

Note: [20] argues that the variable-property correction, $\left(\frac{T_b}{T_w}\right)^{0.25}$ used in the correlations from ESCOA [8] is not necessary. The term is therefore left out. In the correlations from Næss [20], d_e is swapped with d_o since the present study considers I-foot fins, not L-foot fins.

For all correlations and cases the Prandtl number is taken be constant $Pr = 0.7$.

B.1 Heat transfer correlations

B.1.1 Solid fins

ESCOA [8]

$$Nu = 0.091 \cdot Re^{0.75} \cdot Pr^{1/3} \cdot \left[0.35 + 0.65 \cdot e^{-0.25 \cdot \frac{h_f}{p_f}} \right] \cdot \left[0.7 + \left(0.7 + (0.7 - 0.8 \cdot e^{-0.15 \cdot N_i^2}) \cdot e^{-\frac{P_l}{P_t}} \right) \cdot \sqrt{\frac{D_f}{d_o}} \right] \quad (\text{B.1})$$

Stasiulevicius [21]

$$Nu = 0.044 \cdot \left(\frac{P_t}{P_l}\right)^{0.2} \cdot \left(\frac{p_f}{d_o}\right)^{0.18} \cdot \left(\frac{h_f}{d_o}\right)^{-0.14} \cdot Re^{0.8} \quad (\text{B.2})$$

Weierman [25]

$$Nu = 0.25 \cdot Re^{0.65} \cdot Pr^{\frac{1}{3}} \cdot \left(0.35 + 0.65 \cdot e^{-0.25 \frac{h_f}{p_f}} \right) \cdot \left[0.7 + \left(0.7 - 0.8 \cdot e^{-0.15 \cdot N_l^2} \right) \cdot e^{-\frac{P_l}{P_t}} \right] \cdot \left(\frac{D_f}{d_o} \right)^{0.5} \quad (\text{B.3})$$

B.1.2 Serrated fins

ESCOA [8]

$$Nu = 0.091 \cdot Re^{0.75} \cdot Pr^{1/3} \cdot \left[0.35 + 0.65 \cdot e^{-0.17 \cdot \frac{h_f}{p_f}} \right] \cdot \left[0.7 + \left(0.7 + (0.7 - 0.8 \cdot e^{-0.15 \cdot N_l^2}) \cdot e^{-\frac{P_l}{P_t}} \right) \cdot \sqrt{\frac{D_f}{d_o}} \right] \quad (\text{B.4})$$

Næss [20]

$$Nu = 0.197 \cdot Re^{0.65} \cdot Pr^{\frac{1}{3}} \cdot 0.758 \cdot \left(\frac{P_t}{d_o} \right)^{0.35} \cdot \left(\frac{h_f}{p_f} \right)^{-0.14} \cdot \left(\frac{p_f}{d_o} \right)^{-0.2} \quad (\text{B.5})$$

PFR [22]

$$Nu = 0.195 \cdot Re^{0.7} \cdot Pr^{1/3} \cdot Ar^{-0.17} \quad (\text{B.6})$$

$$Ar = \frac{A_{tot}}{A_{bare}}$$

Weierman [25]

$$Nu = 0.25 \cdot Re^{0.65} \cdot Pr^{\frac{1}{3}} \cdot \left(0.55 + 0.45 \cdot e^{-0.35 \frac{h_f}{p_f}} \right) \cdot \left[0.7 + \left(0.7 - 0.8 \cdot e^{-0.15 \cdot N_l^2} \right) \cdot e^{-\frac{P_l}{P_t}} \right] \cdot \left(\frac{D_f}{d_o} \right)^{0.5} \quad (\text{B.7})$$

B.2 Pressure drop correlations

B.2.1 Solid fins

Stasiulevicius [21]

$$Eu = \frac{6.55 \cdot \left(1 - \frac{p_f}{d_o} \right)^{1.8} \cdot Re^{-0.25}}{\left(\frac{P_l}{d_o} \right)^{0.55} \cdot \left(\frac{P_l}{d_o} \right)^{0.5} \left(1 - \frac{h_f}{d_o} \right)^{1.4}} \quad (\text{B.8})$$

Ward and Young [23]

$$Eu = 0.256 \cdot Re^{-0.264} \left(\frac{t}{D_f} \right)^{-0.377} \cdot \left(\frac{p_f}{d_o} \right)^{-0.396} \cdot \left(\frac{P_l}{d_o} \right) \quad (\text{B.9})$$

Weierman [25]

$$Eu = \left(0.28 + \frac{32}{Re^{0.45}}\right) \cdot 0.11 \cdot \left(0.05 \cdot \frac{P_t}{d_o}\right)^{-0.7 \cdot \frac{h_f}{p_f} 0.2} \cdot \left[1.1 + (1.8 - 2.1 \cdot e^{-0.15 \cdot N_l^2}) \cdot e^{-2 \frac{P_l}{P_t}} - (0.7 - 0.8 \cdot e^{-0.15 \cdot N_l^2}) \cdot e^{-0.6 \cdot \frac{P_l}{P_t}}\right] \cdot \left(\frac{D_f}{d_o}\right)^{0.5} \quad (\text{B.10})$$

B.2.2 Serrated fins

Næss [20]

$$Eu = \left(0.2 + \frac{6.75}{Re^{0.5}}\right) \cdot \left(\frac{h_f}{d_o}\right)^{-0.61} \cdot \left(\frac{h_f}{s_f}\right)^{0.33} \cdot \left(\frac{\min(P_t, P_x)}{D_f}\right)^{-0.165} \cdot \min\left(1.0, 0.52 + 964 \cdot e^{-3.2 \cdot \frac{P_t}{P_l}}\right) \quad (\text{B.11})$$

PFR [22]

$$Eu = \left(\frac{19.04}{Re_h^{0.3}}\right) \cdot \left(\frac{P_l}{d_h}\right)^{-0.42} \quad (\text{B.12})$$

$$d_h = 4 \cdot L \cdot \left(\frac{F_t}{A_o}\right)$$

$$L = (N_l - 1) \cdot P_l + (d_o + 2 \cdot h_f)$$

Weierman [25]

$$Eu = \left(0.28 + \frac{32}{Re^{0.45}}\right) \cdot 0.11 \cdot \left(0.05 \cdot \frac{P_t}{d_o}\right)^{-0.7 \cdot \frac{h_f}{p_f} 0.23} \cdot \left[1.1 + (1.8 - 2.1 \cdot e^{-0.15 \cdot N_l^2}) \cdot e^{-2 \frac{P_l}{P_t}} - (0.7 - 0.8 \cdot e^{-0.15 \cdot N_l^2}) \cdot e^{-0.6 \cdot \frac{P_l}{P_t}}\right] \cdot \left(\frac{D_f}{d_o}\right)^{0.5} \quad (\text{B.13})$$

Bibliography

- [1] *ANSYS ICEM CFD Help Manual*.
- [2] *ANSYS Fluent User's Guide*, 2013.
- [3] *ANSYS Fluent Theory Guide*, 2013.
- [4] *CFX Reference Guide*, 2013.
- [5] Bharathan, Panneer Selvam, Bharath Kumar, and S.Bharathwaj. Numerical investigation of air-side heat transfer and pressure drop in serrated finned-tube heat exchangers, 2012.
- [6] Cathal T. O Cleirigh and William J. Smith. Can cfd accurately predict the heat-transfer and pressure-drop performance of finned-tube bundles? *Applied Thermal Engineering*, 73(1):681–690, 2014.
- [7] Eirik Løland Eide. Compact fin-tube heat exchangers for offshore waste heat recovery. NTNU, 2014.
- [8] ESCOA. *Extended Surface Corporation of America, Turb-X HF Rating Instructions*. Pryor, Oklahoma, 1979.
- [9] Kenichi Hashizume, Ryo Morikawa, Tetsuya Koyama, and Takahiro Matsue. Fin efficiency of serrated fins. *Heat Transfer Engineering*, 23:2, 6-14, 2002.
- [10] Rene Hofmann. *Experimental and Numerical Gas-Side Performance Evaluation of Finned-Tube Heat Exchangers*. PhD thesis, Technischen Universitat Wien, 2009.
- [11] Anna Holfeld. *Unpublished work to be published in 2015*. PhD thesis, NTNU, 2015.
- [12] Frank P. Incropera, David P. DeWitt, Theodore L. Bergman, and Adrienne S. Lavine. *Fundamentals of Heat and Mass Transfer*. John Wiley & Sons, Inc., 2007.
- [13] Thea Valsø Klynderud. The influence of free-stream turbulence on heat transfer in finned tube bundles. Master's thesis, NTNU, 2014.
- [14] A. Lemouedda, A. Schmid, E. Franz, M. Breuer, and A. Delgado. Numerical investigations for the optimization of serrated finned-tube heat exchangers. *Applied Thermal Engineering*, 31(8-9):1393–1401, 2010.

- [15] Stuart Russell McIlwain. *Improved Prediction Methods for Finned Tube Bundle Heat Exchangers in Crossflow*. PhD thesis, University of Strathclyde, 2003.
- [16] Mi Sandar Mon. *Numerical Investigation of Air-Side Heat Transfer and Pressure Drop in Circular Finned-Tube Heat Exchangers*. PhD thesis, TU Bergakademie Freiberg, 2003.
- [17] Michael J. Moran, Howard N. Shapiro, Daisie D. Boettner, and Margaret B. Bailey. *Principles of Engineering Thermodynamics*. John Wiley & Sons, Inc., 2012.
- [18] CFD Online. Introduction to turbulence/turbulence kinetic energy. URL http://www.cfd-online.com/Wiki/Introduction_to_turbulence/Turbulence_kinetic_energy.
- [19] E. M: Sparrow and F. Samie. Heat transfer and pressure drop results for one- and two-row arrays of finned tubes. *Pergamon Press Ltd.*, 1985.
- [20] Erling Næss. *An Experimental Study of Heat Transfer and Pressure Drop in Serrated-Fin Tube Bundle and Investigation of Particulate Fouling in Waste Heat Recovery Heat Exchangers*. Doctoral thesis at NTNU, 2007.
- [21] Stasiulevicius, Skrinska, and Zukauskas. *Heat Transfer of Finned Tube Bundle in Crossflow*. Hemisphere Publishing Corporation, 1988.
- [22] PFR Engineering systems. Heat transfer and pressure drop characteristics of dry tower extended surfaces. Technical Report PFR Report BNWL-PFR-7 100, PFR Engineering Systems Inc, 1976.
- [23] D. J. Ward and E. H. Young. Heat transfer and pressure drop of air in forced convection across triangular pitch banks of finned tubes. *Chemical Engineering Progress Symposium Series*, 55(29):37–44, 1959.
- [24] R. L. Webb and N. H. Kim. *Principles of Enhanced Heat Transfer*. Taylor&Francis, New York, 2. edition, 2005.
- [25] C. Weierman. Correlations ease of the selection of finned tubes. *The Oil and Gas Journal*, (36):94–100, 1976.

